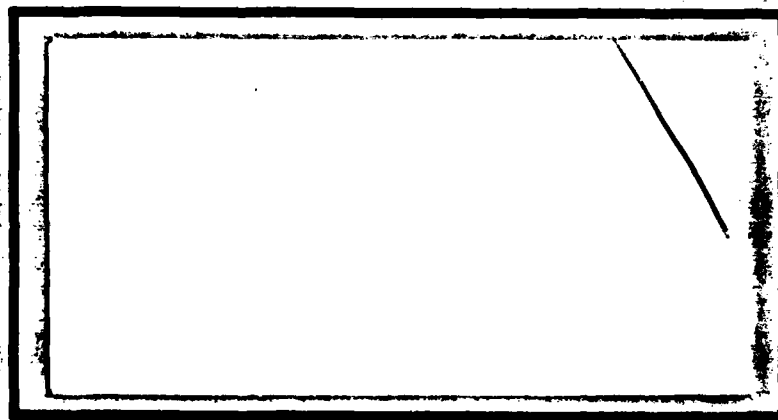DTIC
ELE
S JAN 2 3 1989 D
∞H

DEPARTMENT OF THE AIR FORCE

AIR UNIVERSITY

AIR FORCE INSTITUTE OF TECHNOLOGY

Wright-Patterson Air Force Base, Ohio

89 1 17 117

Optical Information Processing in a
Confocal Fabry-Perot Resonator

THESIS

Jeffery A. Wilson
Captain

AFIT/GEO/ENG/88D-5

DTIC
ELECTE
JAN 2 3 1989
H

Optical Information Processing in a

Confocal Fabry-Perot Resonator

THESIS

Presented to the Faculty of the School of Engineering

of the Air Force Institute of Technology

Air University

In Partial Fulfillment of the

Requirements for the Degree of

Master of Science in Electrical Engineering

Jeffery A. Wilson, B.S.E.E.

Captain

December, 1988

Preface

There are many individuals who deserve thanks for their support. First, I would like to thank Dr. Steve Rogers for his guidance and encouragement during during this research. Dr. Rogers provided many insightful discussions on the concepts within this thesis which led to the optical associative memory architecture design. I am indebted to George Vogel for his support and advice throughout this thesis. He provided the equipment necessary for performance of the thesis from his dissertation equipment and helped analyze both the expected and unexpected results from the crystal and confocal resonator experiments. In addition, I would like to thank Dave Ridenour for his help in providing equipment support and maintenance preventing many down days. Special thanks also go to Capt. Ken Fielding for his suggestions and help in the laboratory and in the preparation of this document.

Most of all. I thank my wife, Marilyn, for her support, understanding and encouragement both in this research effort and throughout my masters' work. Without her support. it all would not have been possible.

Finally, I would like to thank my parents for instilling in me the courage, determination, and self-discipline to see the task through.

Jeffery A. Wilson

DTIC
COPY
INSPECTED
6

Accession For	
NTIS GRA&I	☑
DTIC TAB	☐
Unannounced	☐
Justification	

By
Distribution/
Availability Codes

Dist	Avail and/or Special
A-1	

ii

Table of Contents

List of Figures

AFIT/GEO/ENG/88D-5

Abstract

Many optical information processing algorithms require feedback to perform iterative processing. An algorithm which exemplifies the requirement for feedback is the optical associative memory. This thesis explores the theoretical design of an optical associative memory in a confocal Fabry-Perot resonator.

The components of the optical associative memory — $BaTiO_3$ crystals, confocal resonator, and holographic plates — are characterized individually to determine the feasibility of implementing the associative memory. The $BaTiO_3$ crystals are characterized for processing functions such as image amplification, edge enhancement, linear and nonlinear gain, and linear and nonlinear attenuation. Unique 45°-cut $BaTiO_3$ crystals are investigated in two-wave coupling experiments. The 45°-cut crystals did not perform as expected, and their performance points to a need to improve the mathematical model of two-wave coupling to include the effects of beam-fanning. The sensitivity of the confocal resonator to mechanical vibrations and air currents were learned along with methods to overcome these problems and align/stabilize the resonator. The $BaTiO_3$ crystals were placed within the resonator to perform qualitative analysis on the crystals. Within the resonator, it was verified that the 45° crystal does have more gain potential than the z-cut crystal. Experiments with the holographic plates at the 1–3° angles necessary for the confocal resonator show a diffraction efficiency of 12 %.

The result of these experiments is a qualified yes to the feasibility of the optical associative memory in the confocal resonator. The qualification comes from the need for a better model of two-wave coupling and beam-fanning and follow-on quantitative analysis of the 45°-cut crystal within the confocal resonator.

Optical Information Processing in a
Confocal Fabry-Perot Resonator

I. INTRODUCTION

1.1 Background

A great need exists for automatic target recognizers which are robust under conditions of partially distorted or obscured objects and background clutter. However, the automatic target recognizers that have been realized depend upon a near perfect target image. A method of providing the necessary restoration of distorted or obscured objects and rejection of background clutter is an optical associative memory. An associative memory is one in which a partially distorted or obscured object is input into the memory and an undistorted object is recalled from memory. Optical systems which perform this function have been designed; however, they have been limited in the objects that can be stored and recalled. Most of these systems have been single-pass systems that cannot be operated in a regenerative mode. Regenerative systems allow the stored objects to compete with each other for a more accurate convergence to the correct object. A regenerative associative memory has been developed with planar mirrors for feedback and photorefractive gain to compensate for losses in the feedback path [27]. The stored objects compete with the available gain and the system converges. The optical associative memory presented in this thesis is performed within a confocal resonator with holograms for storage of objects, and two photorefractive crystals, one crystal for linear gain and the other crystal for a nonlinear loss. The confocal resonator allows a compact processing environment, and the two photorefractive crystals provide an energy hump which sets up a gain-loss competition for which of the stored objects will dominate and be recalled.

1

1.2 Problem

An optical associative memory is required that can recall undistorted objects from partial or distorted inputs and from objects within a cluttered background. Optical associative memories have been designed and demonstrated; however, each has had their own limitations. The Air Force Institute of Technology (AFIT) is beginning to investigate optical associative memories and other types of optical architectures and algorithms which require regenerative feedback such as phase retrieval and clutter rejection algorithms. This thesis represents the first steps of AFIT into the use of photorefractive crystals and their operation in resonators. As such, the goal of this thesis is to investigate the properties of a special cut of Barium Titanate, $BaTiO_3$. With this knowledge base, resonator architectures can be designed and research can be performed on optical applications which require optical feedback and gain, such as the associative memory.

1.3 Scope

The scope of this research is to investigate the properties of a special cut of $BaTiO_3$ that will affect the design of an optical associative memory within a confocal Fabry-Perot resonator. There are two reasons the design of an associative memory is investigated. The first is its possible use within automatic target recognition architectures. The second reason is that the associative memory system demonstrates some important design advantages and limitations of the confocal resonator. The tasks that must be performed in undertaking this design are as follows:

1. Characterization of the nonlinear crystals. The photorefractive crystals to be used are $BaTiO_3$. The reason $BaTiO_3$ is being used is because of its large electro-optic coefficients compared to other photorefractive crystals. The optical properties of interest in $BaTiO_3$ are linear amplification and saturated gain/loss within two-wave coupling. Two types of $BaTiO_3$ are to be used in this thesis. The first is a z-cut crystal in which the c-axis of the crystal is

2

parallel to the crystal face, and the other is a special cut crystal in which the c-axis of the crystal is 45° to the crystal face. Three crystals will be used (one z-cut and two 45°-cut crystals) and each needs to be characterized separately. The performance of the 45°-cut crystals will be compared to the z-cut crystal.

2. Characterization of the confocal Fabry-Perot resonator. The confocal resonator to be used is made up of Mangin mirrors which have different radius of curvatures on their front and back surfaces and have the reflective coating on the back surface. The reason for the different curvatures of the two surfaces is to correct for aberrations in the resonator from use of spherical surfaces. The confocal Fabry-Perot resonator requires exact longitudinal spacing to provide optimum feedback without phase error. In order to maintain this alignment the resonator requires active stabilization. Thus, it is necessary first to create an alignment procedure, second to develop a stabilization scheme, and third to characterize the resonator performance.

3. Recording of Phase Holograms. The holographic films to be used are Agfa 8E75-HD holographic plates and Kodak High Resolution 1-A plates. The film needs to be characterized for the particular use in this thesis of low angle (1-3 degrees) multiple exposure holograms. This involves finding the correct exposure times for maximum diffraction efficiency.

4. System Integration. The alignment of the optical elements is critical for exact recombination of the feedback beam with the input beam. After alignment, the system will be characterized for eventual use as an optical associative memory with the properties of restoration of distorted or partial input objects and the rejection of background clutter.

1.4 Organization

This thesis is organized in the order that the research progressed--from theoretical research to experimental demonstration. In Chapter 2, a brief synopsis is

3

presented of the current knowledge within the fields of $BaTiO_3$ research, confocal resonators, photorefractive gain within a ring laser, and optical associative memories. In Chapter 3, the design of an optical associative memory within a confocal resonator is investigated to demonstrate the processing possibilities within a confocal resonator with photorefractive gain and photorefractive nonlinear processing. A theoretical development of the process of two-wave coupling within photorefractive crystals is presented in Chapter 4, followed by the specifics of two-wave coupling within $BaTiO_3$. Experimental results of two-wave coupling experiments, experiments with the confocal resonator and phase holography are presented in Chapters 5-7. In the last chapter, recommendations for optical processing experiments as a result of research performed in this thesis will be presented.

II. SUMMARY OF CURRENT KNOWLEDGE

2.1 Introduction

In order to build an optical associative memory, several areas of current optical research have to be integrated. These areas are $BaTiO_3$ crystals, resonator theory, photorefractive gain within a ring laser, and associative memory systems. The current knowledge in these areas as it pertains to this thesis will be discussed in separate sections.

2.2 Barium Titanate Crystals

Barium Titanate crystals are considered to be good candidates for optical processing applications because of their large electro-optic coefficients relative to other nonlinear crystals [21:4901]. The larger the electro-optic coefficients in a nonlinear crystal, the greater the amplification. $BaTiO_3$ crystals have a tetragonal symmetry (point group 4mm), and its clamped, nonzero, linear electro-optic coefficients are $r_{13} = 8$, $r_{33} = 24$, and $r_{42} = 820$ in units of pm/V. $BaTiO_3$'s unclamped, nonzero, linear electro-optic coefficients are $r_{13} = 24$, $r_{33} = 80$, and $r_{42} = 1640$ in units of pm/V. Unclamped means the crystal can deform according to the law of piezoelectricity, and the deformation follows the modulating frequency of the electric field. Clamped means that the modulation frequency is too high for the crystal to deform by the laws of piezoelectricity. There has not been wide agreement of which coefficients (clamped or unclamped) should be used for two-wave coupling in $BaTiO_3$.

Two-wave coupling is the process of amplification in nonlinear crystals. The physical process of two-wave coupling is where a probe beam and a pump beam are input into a nonlinear crystal and the nonlinear crystal directs energy from the pump beam into the probe beam by the photorefractive effect. (see Figure 1). Lee from the University of California performed theoretical analysis of $BaTiO_3$ crystals to maximize the amplification by varying the input parameters of the crystal,

5
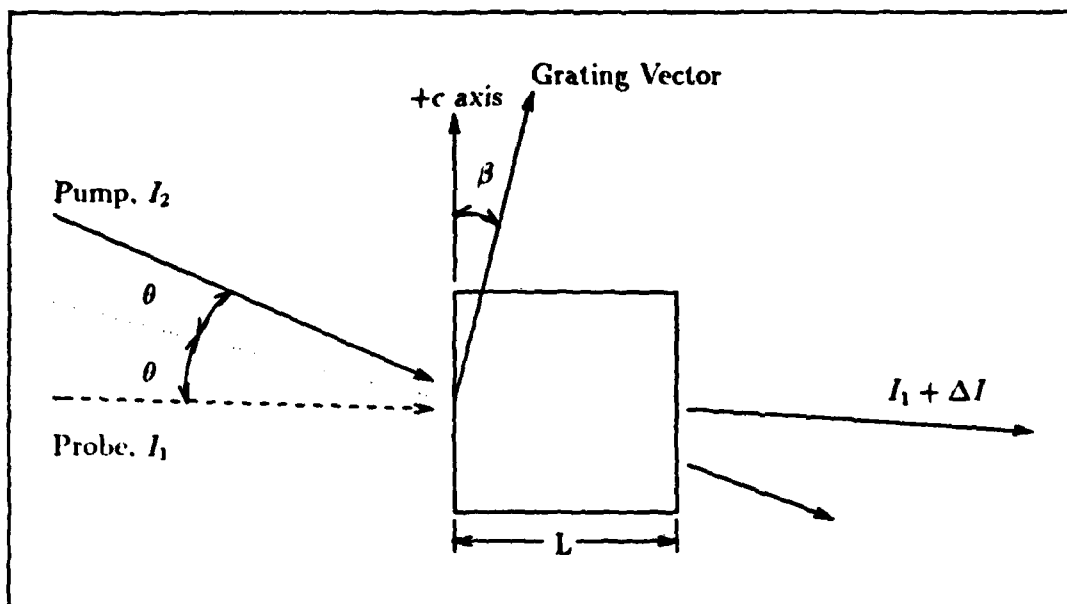
Figure 1. Geometrical Configuration of Two-Wave Coupling. Two coherent beams are directed on the crystal separated by an angle 2θ (internal). The normal to the bisector of the two beams is the grating vector. The angle β is the angle between the grating vector and the +c-axis.

and he recommended a special cut crystal for maximum amplification [11:228]. The input parameters varied were the angle, 2θ, between the pump and probe beam, and the angle, β, between the grating vector and the crystal's optic axis (see Figure 1). The parameters for maximum amplification were found to be $\theta = 2°$ and $\beta = 45°$. However, in this configuration a large percentage of the output power is reflected off the face of the crystal, and the spatial extent of the input face available for use is reduced. Therefore, Lee recommended a 45°-cut crystal (cut along the (100), (011), and (01$\bar{1}$) crystallographic planes) to maximize the amplification (see Figure 2) [11:228-234]. Two 45°-cut crystals will be used in this thesis. In this configuration, Lee reported the $BaTiO_3$ crystal could provide an image amplification of 4000 with a space-bandwidth product of 1,000,000. "The space-bandwidth product is the product of the spatial frequency extent with the spatial extent of the input" [20:1433]. In simple terms, the higher the space-bandwidth product, the higher the
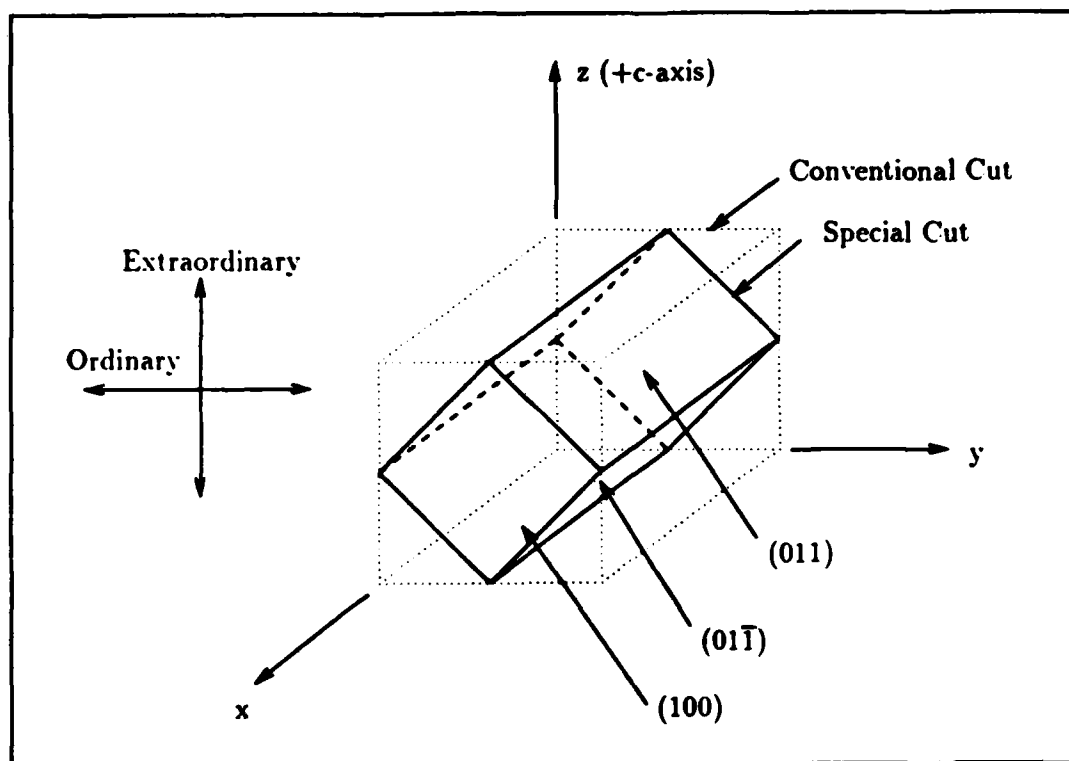
Figure 2.   45°-Cut $BaTiO_3$ Crystal.   The crystal represented by the dashed lines is the
z-cut crystal conventionally used. The crystal represented by the solid lines is
the special 45°-cut recommended by Lee [11:234].

quality of image amplification.

The gain of the crystal is also dependent on the inclination of the polarization
of the incoming laser beam. There are two orthogonal orientations within nonlinear
crystals: ordinary and extraordinary (see Figure 2). With ordinary polarization
(perpendicular to the c-axis), only the smaller r_{13} coefficient can be used; hence, there
is little gain with ordinary polarization. With extraordinary polarization (parallel
to the c-axis), all of the electro-optic coefficients can be used; therefore, more gain
can be achieved with extraordinary polarization.

There are, however, two current problems with the use of $BaTiO_3$: (1) the

manufacture of the crystals is more of an art than a science, leaving each crystal with slightly different operating characteristics; and (2) the exact physics of the operation of the crystal are unknown [21:4901-4905]. There have not been any published results of experiments with a 45°-cut $BaTiO_3$ crystal; therefore, experiments will be required to validate the improved gain behavior of the crystal.

2.3 Resonator Theory

A resonator is required to provide feedback control in an optical associative memory similar to the feedback used in electrical operational amplifiers. The confocal resonator is ideal for coherent optical feedback systems like the optical associative memory because its compact design and two image and Fourier planes. The path of light rays in a confocal resonator is shown in Figure 3 [24:55-57]. The resonator is called confocal because the focal points of the mirrors are at the same point. An advantage of confocal resonators over other types of resonators is that the angular alignment of a confocal resonator is not as critical as other types of resonators;
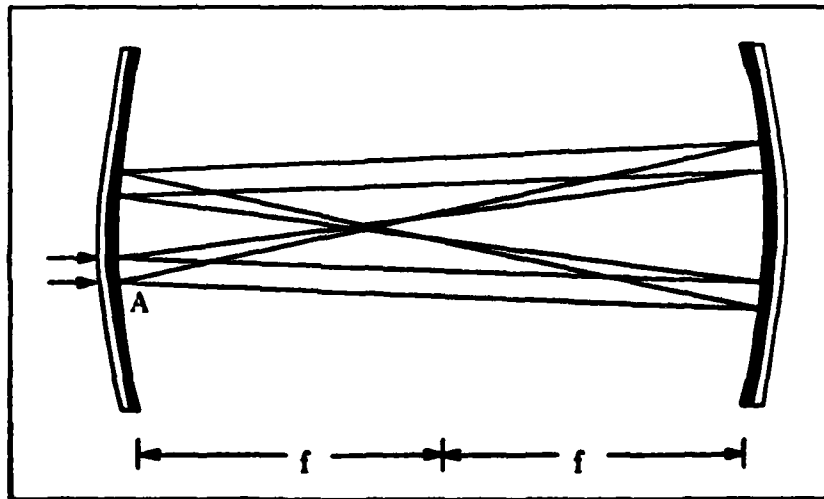
Figure 3. Confocal Resonator. The input beam is brought into the resonator with a non-zero inclination so that the Fourier transform planes will separate.

8
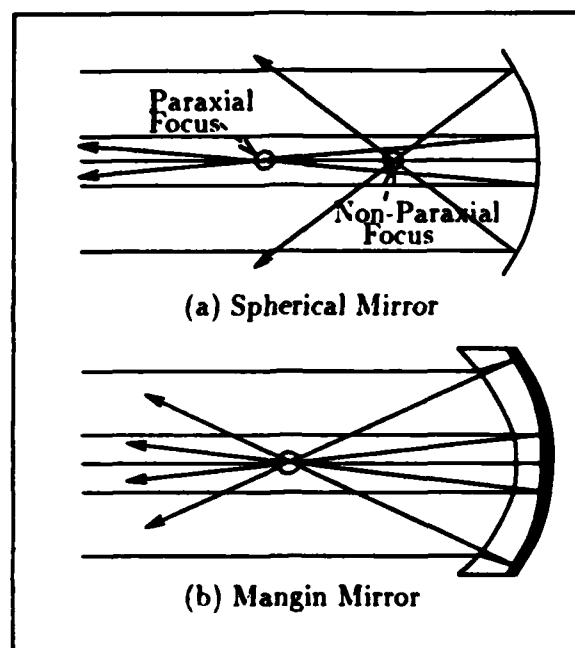
Figure 4. Spherical Aberrations in a Convex Mirror and Aberration Correction with
Mangin Mirrors. With a spherical mirror, the non-paraxial rays focus before
the paraxial focus. A Mangin mirror uses a negative lens to compensate for
the non-paraxial rays.

however, the longitudinal spacing of the confocal resonator is critical.   Lee has
improved the basic design of confocal resonators by replacing the simple spherical
mirrors with Mangin mirrors. Mangin mirrors are unique in that the reflective surface
is the back surface of the mirror and not the front surface. In addition, the radius of
curvature of the two surfaces are different resulting in a convex mirror surface and
a negative lens combination. The improved performance of the resonator is due to
reduction of spherical aberrations present in spherical lenses and mirrors. Spherical
aberrations are present in spherical optics because of the paraxial assumption made
in their design. The result is that rays farther away from the optical axis of the
lens will be focused before the paraxial focus (see Figure 4a). Therefore, the theory
behind the Mangin mirror is that a negative lens compensates for the spherical

9

aberrations introduced by the convex mirror (see Figure 4b). This configuration is quite similar to a doublet lens made of a positive and negative lens to correct for spherical aberrations. Lee has developed the equations for the Mangin mirror parameters (r, R, t and f shown in Figure 5) [20:1431- 1437] [10:535-540].

The resonator to be used in this thesis is similar to the resonator used by Lee. but it has been designed for operation at a wavelength of 575 nm instead of the 514.5 nm used by Lee. The Mangin mirror specifications are:

$$r = 34.25 cm$$

$$R = 53.29 cm$$

$$t = 1.5 cm$$

$$f = 35 cm$$

The physical dimensions of the confocal resonator are 70 cm in length and 72 mm in width. This is a very large for an optical cavity and will require active stabilization
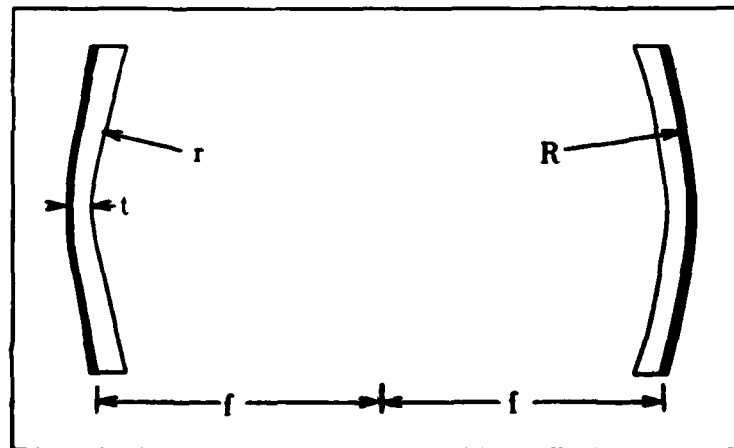
Figure 5. Mangin Mirror Confocal Resonator. The focal lenght, f, is the focal length of the negative lens-convex mirror combination. R is the radius of the outside surface, r is the radius of the inside surface, and t is the thickness of the negative lens at the center.

circuitry to maintain the exact longitudinal spacing between the mirrors. This cavity size should not deter using the confocal resonator within optical systems that must be compact because the confocal resonator can be miniaturized once a design is demonstrated on a "breadboard" resonator.

2.4 Photorefractive Gain within a Ring Laser

Anderson from the University of Colorado has modeled the results of photorefractive gain within a ring laser, and he has performed ring laser experiments [4] [5]. A ring laser is formed when a $BaTiO_3$ crystal is placed within a resonator as shown in Figure 6 and a pump beam is directed onto the crystal. A process called asymmetric defocusing or more commonly called "beam-fanning" scatters the pump beam and provides the initial energy for the lasing path. This energy is fed back to the crystal and a grating is formed in the crystal which deflects additional energy into the laser
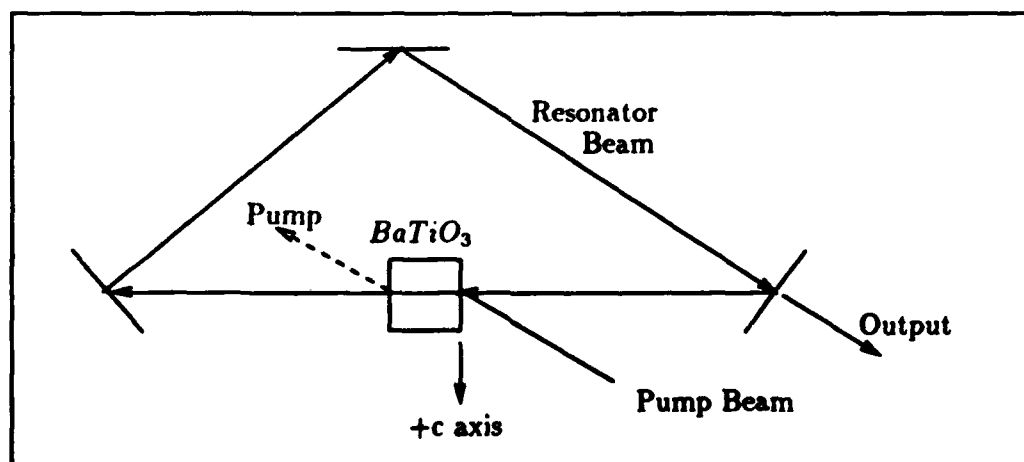
Figure 6.   Photorefractive Gain in a Ring Laser.   A laser is built with $BaTiO_3$ crystal as the laser medium. The lasing process with a $BaTiO_3$ is different from conventional lasers in that the resonator beam is formed and maintained by the deflection of the pump beam into the cavity and not from stimulated emission.

cavity by two-wave coupling. Two important results have come from his research that relate to this thesis.

First, Anderson proved that the ring laser formed with a photorefractive crystal will have its cavity frequency pulled towards the frequency of the pump beam within a few hertz. Thus, unlike a gas laser, a laser formed with photorefractive gain lases consistent with the cavity and the frequency of the pump beam, whereas a gas laser lases at a frequency consistent with the mirror spacing. The reason for this effect is because of the method of energy transfer in the photorefractive case is diffraction off of gratings internal to the crystal, while the gas laser lases due to the stimulated emission of photons from transitions within the media.

The other important result occurs when a hologram is placed within the laser cavity. These stored objects are eigenmodes of the resonator and control the areas of gain. Anderson demonstrated that after the objects have been stored in the resonator and a pump beam is directed onto the crystal, the ring laser will operate with all the eigenmodes present. At times, one mode may be brighter than the others and the laser may oscillate between the eigenmodes. However, if an eigenmode or partial eigenmode is input into the ring laser, the ring laser will operate in that eigenmode only. In other words, the ring laser will resonate on the presented input, enhance it (recall the full object), and will win the competition for the available gain in the resonator.

2.5 Associative Memory Systems

An associative memory is one in which a partially distorted object is input into the memory and an undistorted object is recalled from the memory. In a block diagram, an associative memory would be as shown in Figure 7. First, a distorted input is compared with a number of stored objects. Each comparison is scored on how close the input matches the stored object. The scores are then subjected to criteria to determine which, if any, of the stored objects is most similar to the distorted

12
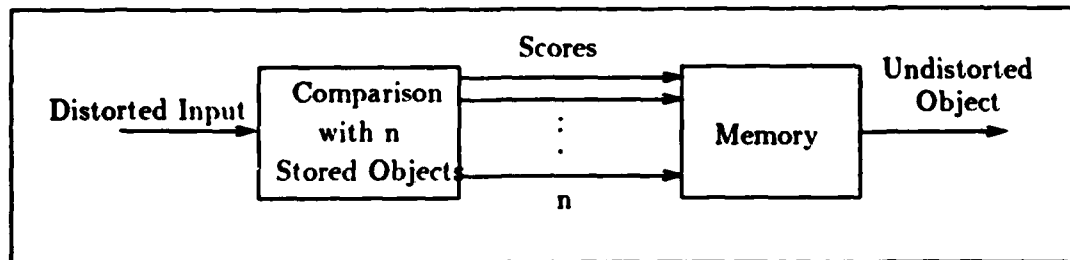
Figure 7. Block Diagram of an Associative Memory.
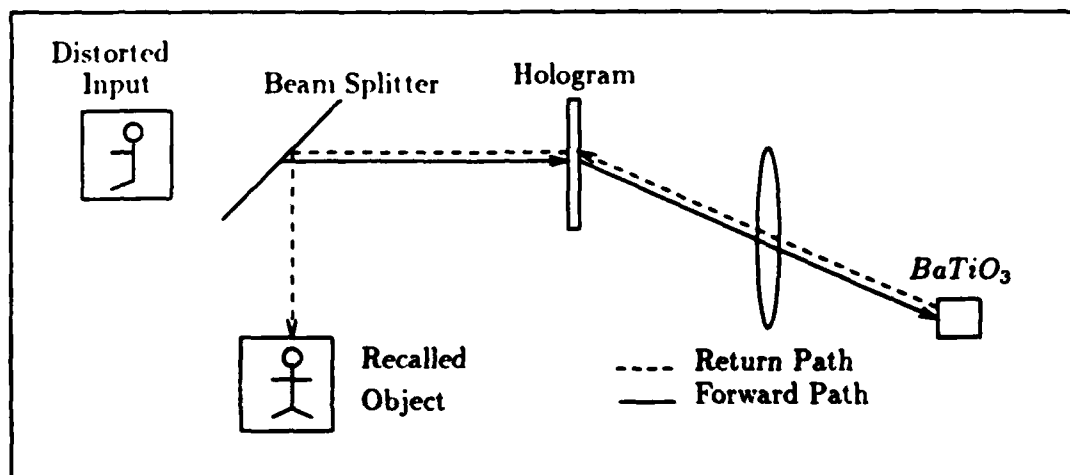
Figure 8. Hughes Laboratories' Associative Memory.

object. The highest score acts as a memory address to recall the undistorted object from memory.

There have been several optical systems that perform as an optical associative memory, with one being similar to Anderson's memory in a resonator. Notable among these systems not within a resonator is the design of Hughes Research Laboratories (see Figure 8). This system was investigated in another thesis at AFIT [16]. The system is based upon the re-illumination of a Vander Lugt filter with an input and a phase conjugate mirror in the correlation domain of the Vander Lugt filter. The phase conjugate mirror, a $BaTiO_3$ crystal, thresholds the correlation peaks and re-illuminates the hologram from the backside with a reconstructed reference beam.
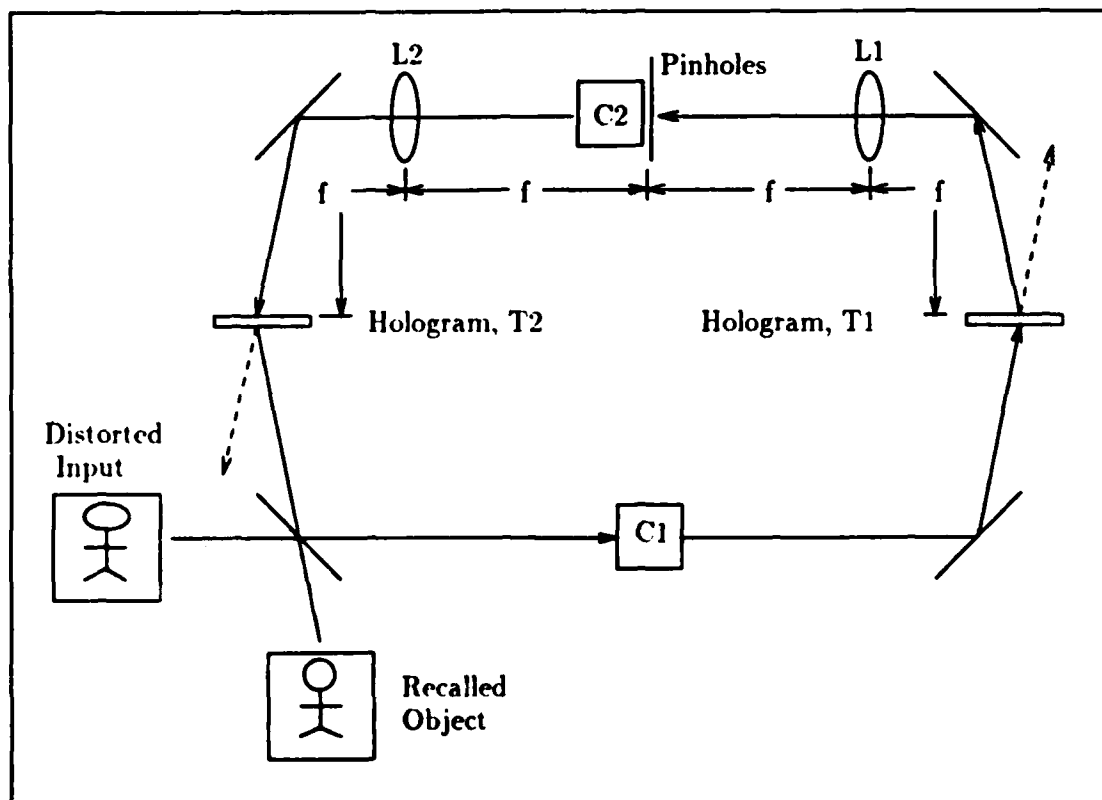
Figure 9.   Northrop's Associative Memory.   The pump beams for the two-wave cou-
pling within the $BaTiO_3$ crystals are not pictured.

The re-illumination recalls the undistorted object on-axis.

A resonator design similar in concept to Anderson's is a design by Northrop
[27]. This design is very similar to the design of the resonator used in this thesis.
It involves the use of two $BaTiO_3$ crystals (z-cut), planar mirrors for feedback, 2
holograms, and a set of pinholes (see Figure 9). The input is sent through crystal C1
and is projected onto hologram T1 which acts as a Vander Lugt filter. The correlation
term is Fourier transformed by lens L1. The correlations are spatially filtered by the
pinholes and amplified by crystal C2 to become reference beams for hologram T2.
The recalled object from hologram T2 is fed back to crystal C1 where the fed back
object is added to the original input object. The system then resonates until a
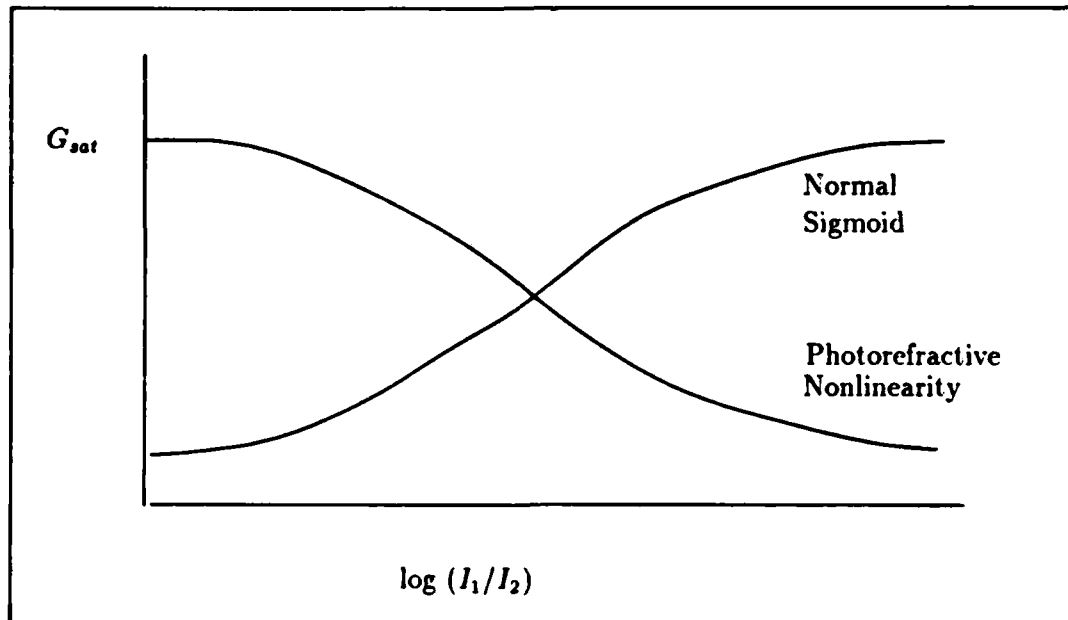
Figure 10. Photorefractive Nonlinearity. The photorefractive nonlinearity used by Northrop is plotted with a sigmoid function. Note that normally a sigmoid function within a neural network passes the larger values while suppressing the smaller ones. The equation which governs these curves is presented in Chapter 4 (Equation 25).

steady state solution is found. The operation of the crystals within this associative memory is critical. Crystal C2 operates as a linear amplifier to compensate for losses within the resonator. However, crystal C1 is operating as a nonlinear gain mechanism in which the gain is dependent on the intensity of the input beam (probe beam) compared to the pump beam–the larger the input, the lower the gain; and similarly, the lower the input, the larger the gain. The gain dependence on intensity ratio of probe beam to pump beam is discussed in Section 4.3.3. Within neural network terminology, crystal C1 operates as a node in which nonlinear summation occurs. This nonlinear summation can be modeled as a sigmoid function; however, the sigmoid function is reversed from the normal neural network use (see Figure 10). There is then competition between the modes (one mode being one stored object) for

the available gain within the resonator with the mode that is most closely associated with the input winning the competition.

The differences between Northrop's system and this thesis is the feedback system used and the operation of the two crystals. The feedback system used in this thesis is the confocal resonator which allows for compactness of design with two image and Fourier planes. The greatest difference is in the crystal operations. Both of Northrop's crystals (z-cuts) are used for amplification: one crystal for linear amplification and the other crystal for nonlinear amplification (linear and nonlinear amplification is discussed in section 4.3.3). Therefore, there is only a competition for the gain within the resonator between stored objects. However, in this thesis, a 45°-cut crystal is used for linear amplification and a z-cut crystal is used as a nonlinear attenuator (section 4.3.3). This combination allows for competition for the available gain while suppressing the weaker objects competing for the gain with the nonlinear attenuator.

2.6 Summary

This summary of current knowledge is the foundation upon which this thesis is built. Much work has been performed with $BaTiO_3$ crystals; however, much is still not known about the material. Experimental results of two-wave coupling within 45°-cut crystals have never been published —only six 45°-cut crystals of $BaTiO_3$ have been manufactured as of this thesis. Therefore, the theoretical performance of the 45°-cut crystal has not been verified. In addition, research has not been performed on the interaction between two crystals where one is a gain mechanism and the other is a loss mechanism. The confocal resonator mirrors were procured with different reflectances on the back surface than those used by Lee for operation at 575 nm instead of 514 nm used by Lee. Thus, the mirrors must be characterized at 575 nm.

Within the next chapter, a detailed development of the theory of the optical

associative memory is presented. First, the principles of holography will be discussed because of their integral part within optical associative memories. From the principles of holography along with Vander Lugt filter theory, the optical associative memory in the confocal resonator will be designed.

III. OPTICAL ASSOCIATIVE MEMORY

3.1 Introduction

Holograms have been used as storage media for objects that can be recalled with their associated reference beams. Gabor the inventor of the first holographic process first discussed the potential of using holograms as an associative memory. An associative memory is one in which a partially distorted object is input into the memory and an undistorted object is recalled from the memory. Holograms are an integral part of the associative memory designed in this chapter. Two holograms are to be used. The first hologram will operate as a Vander Lugt filter [18], while the second hologram will be the memory core of the associative memory. In this chapter, the conceptual design of an associative memory in a confocal Fabry-Perot resonator is performed. However, before preceding onto the system design, a basic understanding of holography must be developed.

3.1.1 Holograms
The basic component of the associative memory is the hologram. The operation described in this section is based upon the Vander Lugt matched spatial filter [18]. When an object is stored on a holographic plate, the transmittance function recorded is:

$$T = |\mathbf{A}|^2 + |h|^2 + \mathbf{A}^*h + \mathbf{A}h^*$$ (1)

where $\mathbf{A} = A\ exp[-j2\pi\alpha x]$ is the reference beam, $\alpha = sin(\theta)/\lambda$ is the spatial frequency, and h is the stored object (see Figure 11). The selection of the spatial frequency, α, will be discussed later in this section. When the hologram is re-illuminated with the object, g, the result is a multiplication of g with the input transparency (see Figure 12).

$$gT = g|\mathbf{A}|^2 + g|h|^2 + g\mathbf{A}^*h + g\mathbf{A}h^*$$ (2)

18
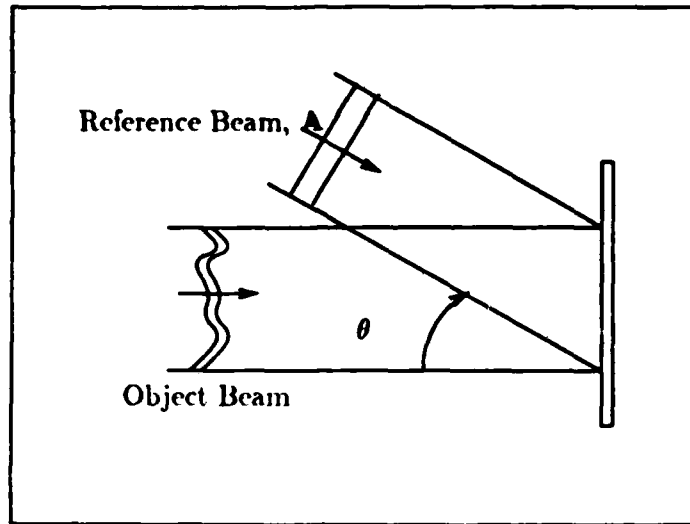
Figure 11. Recording a Hologram on a Photographic Plate.

The first two terms in this multiplication are unimportant because they both are positioned on-axis with no means of separating the terms due to the loss of the phase. However, the third and fourth terms are important because the amplitude and phase of the objects are stored in these terms, and the terms become spatially separate after propagation (see Figure 12). If the third and fourth terms are now Fourier transformed by use of a lens as in Figure 12, the result is:

$$\mathcal{F}[\text{Third term}] = \frac{1}{\lambda f} \, [G \star a^*] \ast H \qquad (3)$$

$$\mathcal{F}[\text{Fourth term}] = \frac{1}{\lambda f} \, [G \star H^*] \ast a \qquad (4)$$

After examination of the Fourier transforms, it is seen that the fourth term is of interest because it is the correlation of the input with the stored object. The third term is a convolution and is not of immediate interest for the associative memory. The peak of the correlation is a measure of how close the input matches the stored image (assuming energy normalization of input and stored objects).

19
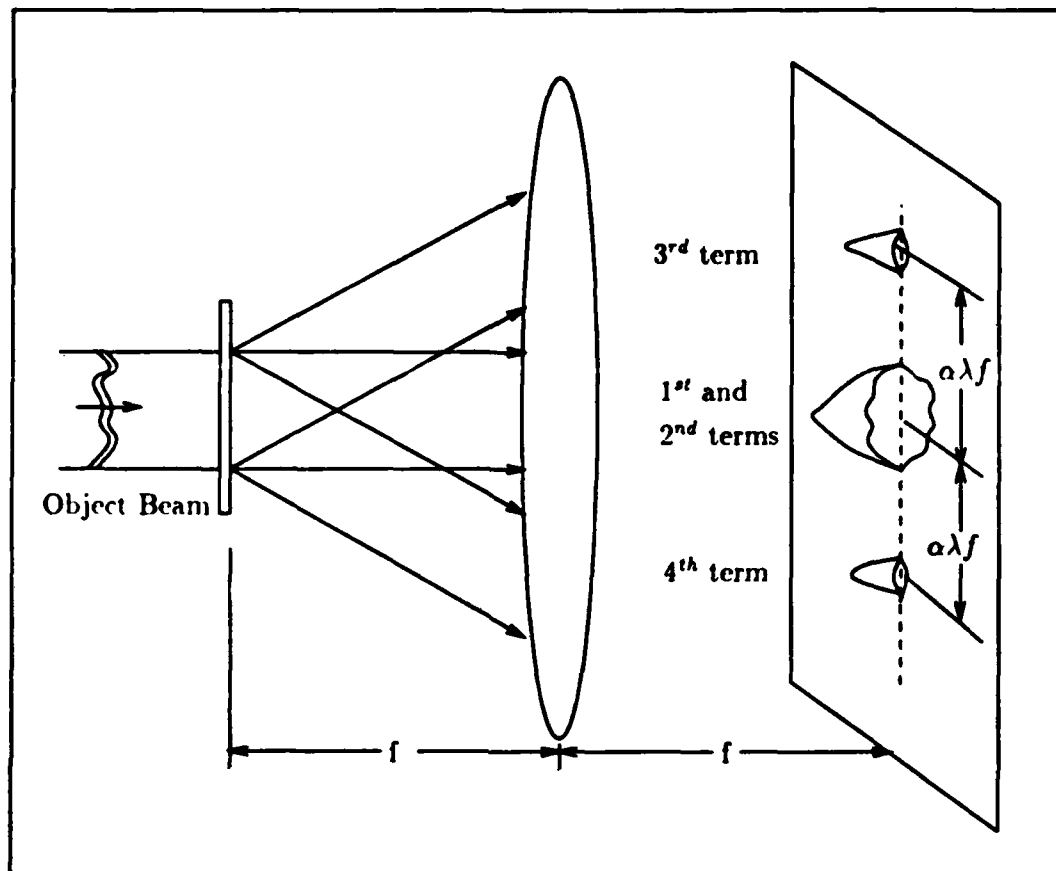
Figure 12. Re-illumination of Hologram with object.

The reason the third and fourth terms are spatially separated from the first and second terms is due to the spatial frequency, α, the hologram is recorded at. But in order for the terms to completely separate, a minimum spatial frequency (angle) must be used. The minimum α is based upon the spatial frequency content of the input object, W'_g, and the stored object, W_h. The width of the terms in Figure 12 are given by [18]:

$$\text{First term}: \quad W'_g$$

$$\text{Second term}: \quad 2W_h + W_g$$

$$\text{Third term}: \quad W_h + W_g$$

$$\text{Fourth term}: \quad W'_h + W'_g \tag{5}$$

From these widths and an examination of Figure 12, the minimum α for complete separation is:

$$\alpha > \frac{1}{\lambda f}\left(\frac{3W'_h}{2} + W'_g\right) \tag{6}$$

Once the minimum α is met, the third and fourth terms resulting from the re-illumination of the hologram will separate and be centered at $\pm\alpha\lambda f$.

Holograms can be used as a matched spatial filter where the input object is correlated with the stored object. The largest correlation peak will occur when the input exactly matches the stored image (assuming energy normalization of objects), and all peaks for either a distorted image or a different object will be smaller.

3.1.2 Multiple Object Holography In order for an associative memory to be useful, more than one object should be stored in the memory. For use in a clutter rejection algorithm or an image correction algorithm, only one object need be stored; however, to increase its usefulness, more than one object should be stored. With a hologram, there are many ways to store k objects. The method used in this thesis is angle multiplexing. In angle multiplexing, each object, h^k, is recorded with its own reference beam at angle θ_k so the first diffracted orders are separate in the correlation domain. The transmittance function of an angle multiplexed hologram is:

$$T = \sum_{k=1}^{n} [|A^k|^2 + |h^k|^2 + A^{k*}h^k + A^k h^{k*}] \tag{7}$$

where $\mathbf{A}^k = A^k exp(-j2\pi\alpha_k x)$. The angles selected for angle multiplexing are selected such that the correlations do not overlap in the correlation domain. In order for this to be accomplished, an analysis similar to the previous section must be performed. The on-axis terms shown in Figure 12 will remain the same width as before if it is assumed the stored objects have similar spatial frequency content. Therefore, as long as the minimum α of Equation 6 is met, the third and fourth terms in the re-illumination will separate from the first and second terms. In multiple

21
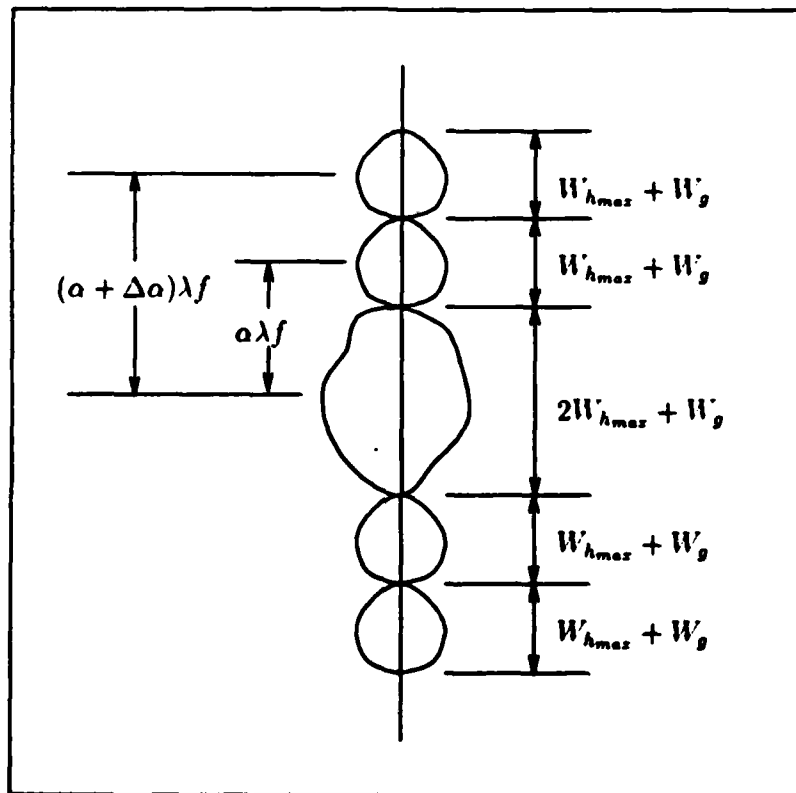
Figure 13. Output of a Multiple Object Hologram in the Fourier Domain. $W'_{h_{max}}$ is the width of the Fourier transform with the highest spatial frequency. $\Delta\alpha$ within $(\alpha+\Delta\alpha)\lambda f$ is the minimum $\Delta\alpha$ such that no overlap of the correlations occur.

object holography, however, an added concern is the separation of the third and fourth terms of the different objects. If it is assumed that the first object is stored at the spatial frequency of α, then the second object must be stored at $\alpha + \Delta\alpha$. The minimum $\Delta\alpha$ is met when (see Figure 13):

$$\Delta\alpha = W'_{h_{max}} + W'_g \qquad (8)$$

Once the angles are selected, the hologram made and re-illuminated with the object, g, the Fourier transform of the fourth term is:

$$\mathcal{F}[\text{Fourth term}] = \sum_{k=1}^{n} [(G \star H^{k\bullet}) \star a^k] \qquad (9)$$

This equation represents the correlation of the input object with all of the stored objects.

3.2   Single-Pass Associative Memory

An associative memory schematic based on the properties of angle multiplex holograms is shown in Figure 14. The memory consists of two angle multiplexed
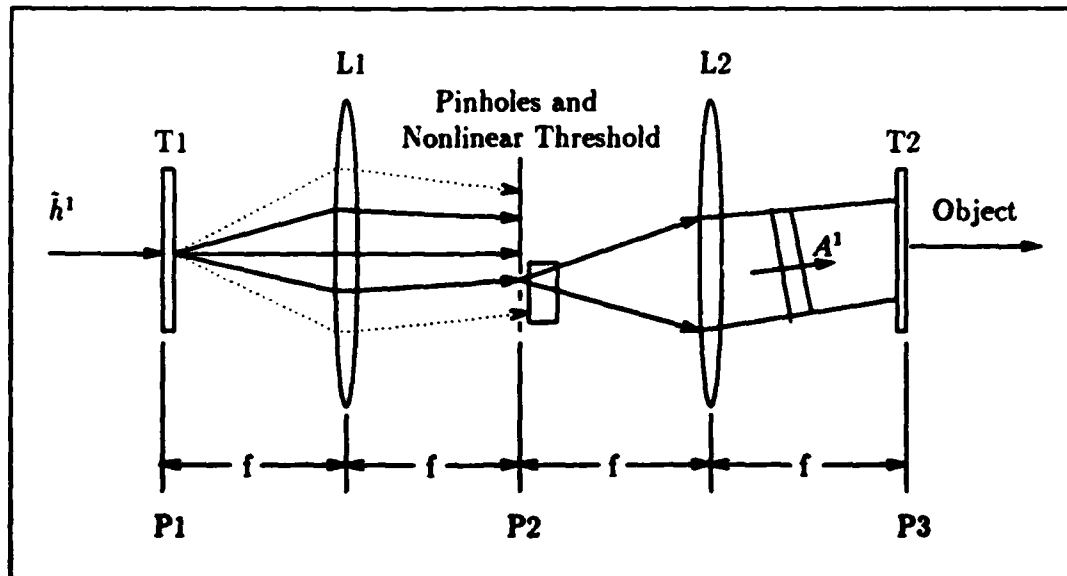
Figure 14. Single-Pass Optical Associative Memory.

23
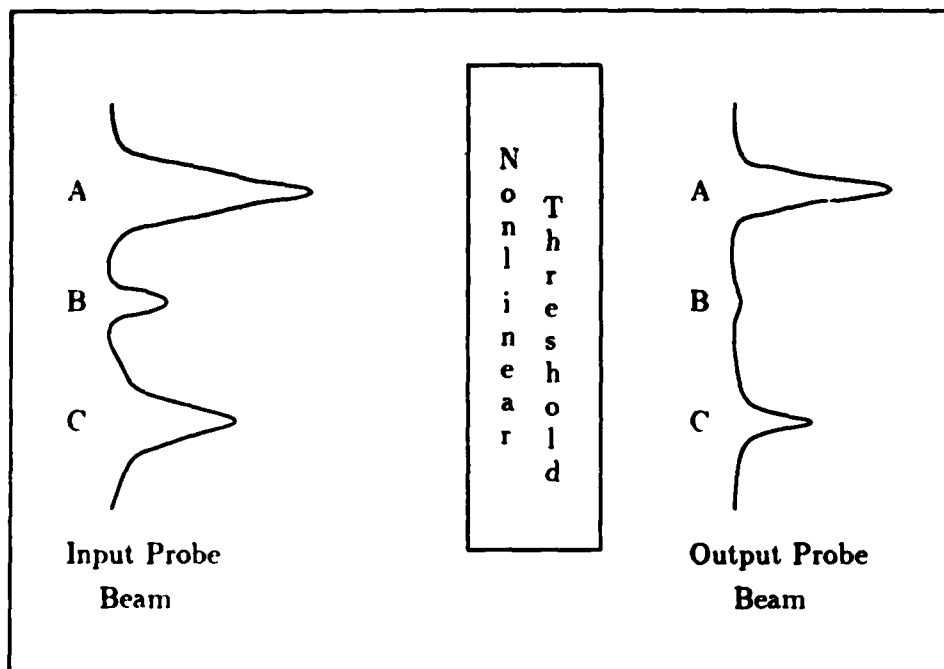
Figure 15. Nonlinear Thresholding of Correlation Peaks. The nonlinear threshold passes large intensity peaks with a small amount of attenuation. However, small intensity peaks are attenuated a larger amount.

holograms, T1 and T2; two lenses, L1 and L2; a nonlinear threshold device; and a set of pinholes. First, the theory of operation of the associative memory will be presented followed by the mathematical development.

The first hologram along with the first lens performs the correlation of the distorted object with the stored objects on the hologram. The correlation peaks are pinholed to pass only the peak values. The peak values are then sent through a nonlinear threshold device. All peaks will be attenuated by the nonlinear threshold with the strongest peak being attenuated less than the weaker peaks (see Figure 15). The peak values passed by the pinholes will be modeled as delta functions. The delta functions are Fourier transformed by the second lens and projected onto the second hologram as a reference beam. The reference beam projected on the second

hologram is associated with the stored object that is most closely related to the distorted input object. Therefore, the on-axis term from the second hologram is the object associated with the input.

Mathematically, the system works as follows. The information stored on the two holograms is:

$$T1 = \sum_{k=1}^{n} [|\mathbf{A}^k|^2 + |h^k|^2 + \mathbf{A}^{k*} h^k + \mathbf{A}^k h^{k*}] \qquad (10)$$

where $\mathbf{A}^k = A exp(-j2\pi\alpha_k x)$; and:

$$T2 = \sum_{k=1}^{n} [|\mathbf{B}^k|^2 + |h^k|^2 + \mathbf{B}^{k*} h^k + \mathbf{B}^k h^{k*}] \qquad (11)$$

where $\mathbf{B}^k = B exp(+j2\pi\alpha_k x)$. The reason the reference beam, B^k, is the conjugate about the z-axis of the reference beam, A^k, is due to the inversion by the two lenses.

A distorted input object, $\hat{h}^1$, is illuminated onto T1 at plane P1. The fourth term of the multiplication between $\hat{h}^1$ and T1 is Fourier transformed by lens L1 and projected onto plane P2:

$$\mathcal{F}[\text{Fourth term}] = \underbrace{(\hat{H}^1 \star H^{1*}) * a^1}_{\text{autocorrelation}} + \underbrace{\sum_{k=2}^{n} [(\hat{H}^1 \star H^{k*}) * a^k]}_{\text{cross-correlation}} \qquad (12)$$

Each of these correlation peaks are spatially separate due to the angle multiplexing of the reference beams. If the correlation peaks are now pinholed to pass only the peak value, the result is delta functions of unequal intensities—the greatest being the correlation of $\hat{h}^1$ with the stored object h^1:

$$U_{P2-} = \sum_{k=1}^{n} \hat{H}^1 H^{k*} a^k \delta(f_x + \alpha_k) \qquad (13)$$

(Note: $\hat{H}^1 H^{k*} a^k$ is the zero shift correlation magnitude.) The correlation peaks are subject to a nonlinear threshold with a crystal of $BaTiO_3$ (discussed in Chapter 3) oriented such that there is a nonlinear loss for the input (see Figure 15). The

nonlinear loss, L, is adjusted such that the small peaks are attenuated more than the greatest peak for h^1:

$$U_{P2+} = (K - L)\, \delta(f_x + \alpha_1) \tag{14}$$

where K is a constant $= \tilde{H}^1\, H^1\, a^1$. This delta function which is passed through the crystal is now Fourier transformed by lens L2 to form a plane reference beam for the second hologram at plane P3:

$$U_{P3-} = \mathcal{F}[U_{P2+}] = (K - L)\, exp(+j2\pi\alpha_1 x) \tag{15}$$

At P3, U_{P3-} and T2 multiply together. The third term is of interest after multiplication because the phase terms in the reference beam cancel with the stored object associated with the distorted input object; therefore, the recalled object travels on a spatial carrier of zero (on-axis):

$$
\begin{aligned}
U_{P3}[\text{Third term}] \ &= \ (K - L)\, exp(+j2\pi\alpha_1 x) \sum_{k=1}^{n}[\mathbf{B}^{k*} h^k] \\
&= \ (K - L)[B^1 exp(-j2\pi\alpha_1 x)\, exp(+j2\pi\alpha_1 x)]h^1 \\
&\quad + \sum_{k=2}^{n} [(K - L)\, exp(+j2\pi\alpha_k x)\mathbf{B}^{k*} h^k] \\
&= \ (K - L)B^1 h^1 + \sum_{k=2}^{n} [(K - L)\, exp(+j2\pi\alpha_k x)\mathbf{B}^{k*} h^k] \tag{16}
\end{aligned}
$$

All the other stored objects will also be output from hologram T2, but they will travel off-axis.

Therefore, the system works as an associative memory where the stored object that is closest to the distorted input image is recalled and displayed without distortion.

3.3 Iterative Optical Associative Memory

The single-pass optical associative memory presented in the previous section is not without its problems. A major problem is the recalled object is not fed back to
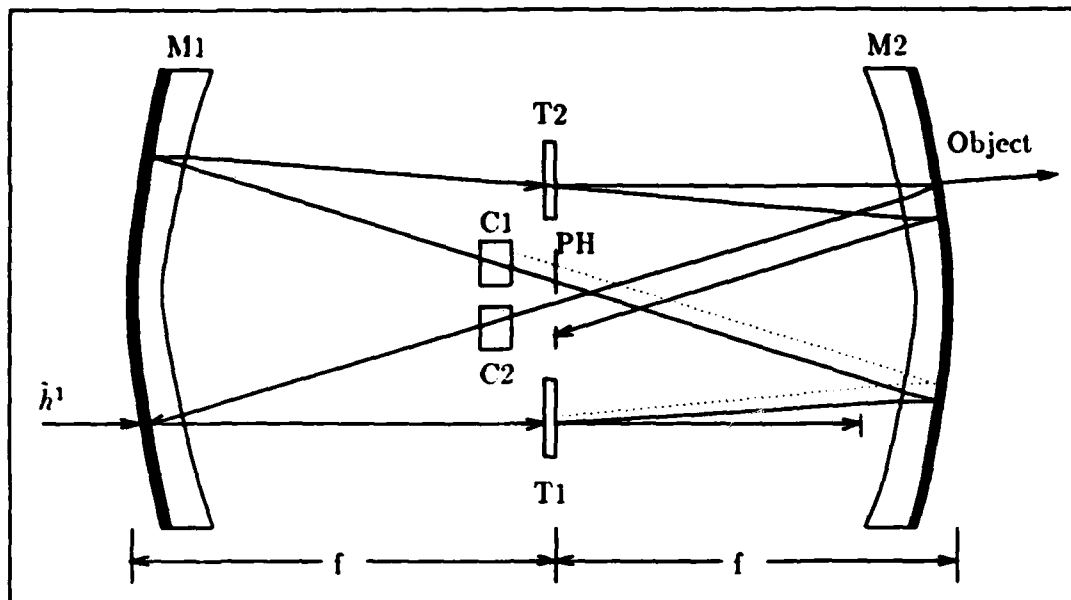
Figure 16. Optical Associative Memory in Confocal Resonator.

the input to ensure the recalled object is consistent with the distorted input object. The feedback necessary to ensure this consistency can be provided with the confocal resonator configuration shown in Figure 16. The resonator memory is composed of two concave Mangin mirrors, M1 and M2; two $BaTiO_3$ crystals, C1 and C2; two holograms, T1 and T2; a set of pinholes, PH; and a restricting aperture. The iterative associative memory will be presented like the single-pass memory– theory of operation first, followed by a mathematical development.

The distorted input object is transmitted through mirror M1 onto the hologram T1. Mirror M2 acts as a Fourier transform lens to transform the output of T1; therefore, correlations appear at the pinholes PH. The pinholes pass only the correlation peaks to the crystal C1, which performs a nonlinear threshold operation on the peaks passing only the greatest ones as described in the last section. The delta function is then Fourier transformed by M1 and projected onto the second hologram T2 as a reference beam. This reference beam is the one associated with the stored object the distorted input is most like. The recalled object is linearly amplified by

27

crystal C2 to make up for the cavity losses in the resonator. An aperture is placed before C2 to block the off-axis beams of the other objects stored on hologram T2. The output of C2 then recombines with the distorted input beam. The feedback required for operation as an associative memory is positive. Positive feedback is assured when an input is presented by maintaining the proper mirror spacing. This allows the addition of the distorted input, $\tilde{h}^1$, with the recalled object, h^k. The system then resonates until a steady state solution is found.

This design incorporates features which take advantage of the confocal resonator's advantages and disadvantages. First, both the two image and two Fourier transform planes are used for optical processing elements. A confocal resonator disadvantage this design takes advantage of is the fact that the confocal resonator is an on-axis resonator, meaning it does not allow for any deflection of beams within the resonator. If a beam is deflected, the fed back beam will not recombine with the input beam. However, by virtue of having two holograms in the resonator, the deflection of one hologram is compensated by the other hologram to restore the beam alignment. In addition, the Fourier transform planes were able to be separated in this design with the input beam at $0°$ inclination because of the deflection off of the holograms. Thus, the disadvantage works to the advantage of the design.

Mathematically, the iterative system is similar to the single-pass system; however, there are some unique requirements in the resonator which are shown in this development. The information stored on the two holograms is:

$$T1 = \sum_{k=1}^{n} [|A^k|^2 + |h^k(x,y)|^2 + A^{k*} h^k(x,y) + A^k h^{k*}(x,y)] \qquad (17)$$

where $A^k = A exp(-j2\pi\alpha_k x)$; and:

$$T2 = \sum_{k=1}^{n} [|B^k|^2 + |h^k(-x,-y)|^2 + B^{k*} h^k(-x,-y) + B^k h^{k*}(-x,-y)] \qquad (18)$$

where $B^k = B exp(+j2\pi\alpha_k x)$. The reason the reference beam is the inverse linear phase about the z-axis and the object is inverted is due to the inversion by the two

28

lenses. In the single iteration associative memory, the holograms did not need to be recorded while in the system and the recalled object was not fed back to the input, so there was no concern over beam recombination. However, in the iterative system the fed back object must combine with the distorted input.

A distorted input object, $\tilde{h}^1$, is transmitted through M1 and illuminated onto T1. The fourth term of the multiplication between $\tilde{h}^1$ and T1 is Fourier transformed by mirror M2 and projected onto the pinholes:

$$\mathcal{F}[\text{Fourth term}] = \underbrace{(\tilde{H}^1 \star H^{1*}) * a^1}_{autocorrelation} + \underbrace{\sum_{k=2}^{n} [(\tilde{H}^1 \star H^{k*}) * a^k]}_{cross-correlation} \tag{19}$$

Each of these correlation peaks are spatially separate due to the angle multiplexing of the reference beams. The correlation peaks are pinholed to pass only the peak value, the result is delta functions of unequal intensities.

$$U_{PH-} = \sum_{k=1}^{n} \tilde{H}^1 H^{k*} a^k \delta(f_x + \alpha_k) \tag{20}$$

The correlation peaks are subject to a nonlinear threshold with a crystal of $BaTiO_3$ (discussed in Chapter 3) oriented such that there is a nonlinear loss, L, for the input (see previous section).

$$U_{PH+} = (K - L) \delta(f_x + \alpha_1) \tag{21}$$

where K is a constant $= \tilde{H}^1 H^1 a^1$. This delta function which is passed through the crystal is now Fourier transformed by mirror M1 to form a plane reference beam for the second hologram T2:

$$\mathcal{F}[U_{PH+}] = (K - L) exp(+j2\pi\alpha_1 x) \tag{22}$$

The third term is of interest after the multiplication of T2 with the reference beam because the phase terms in the reference beam cancel with the stored object associated with the distorted input object, and the recalled object travels on a spatial carrier of zero (on-axis):

$$U_{P3}[\text{Third term}] = (K - L) exp(+j2\pi\alpha_1 x) \sum_{k=1}^{n} [\mathbf{B}^{k*} h^k]$$

$$= (K - L)B^1 h^1 + \sum_{k=2}^{n} [(K - L) \, exp(+j2\pi\alpha_k x)\mathbf{B}^{k} h^k] \quad (23)$$

All the other stored objects will be output from hologram T2, but they will travel off-axis. Since these off-axis terms will be collected by mirror M1 and combine with the distorted input just like the on-axis recalled term, an aperture is required in the Fourier plane to block the off-axis terms.

Crystal C2 is setup as a linear amplifier as described later in Chapter 3. The amplification provided by C2 is required to make up for the losses in the mirrors, crystal C1, and the holograms. The amplified output of C2 is then recombined with the input object with positive feedback:

$$U_{T1} = \tilde{h}^1 + \mathcal{O}[\tilde{h}^1] \quad (24)$$

where $\mathcal{O}$ stands for the mathematical operation provided in the feedback. Therefore, when a distorted object is input, there is a gain-loss competition between crystals C1, C2, and the permitted connections provided by the holograms for convergence to the correct output object for the distorted input.

In the terminology of Anderson [4:56], the resonator has n equally likely modes which compete for the available gain. With no input, the internal fields will be a sum of the resonator modes where at times one mode may be dominate over another. With an input injected into the resonator, the mode that the input is most like has the advantage and is more likely to win the mode competition. As long as the input is presented, the setup mode will remain steady state; however, once the input is removed the resonator will return to its internal competition.

3.4 Summary

Two designs of optical associative memories have been presented in this chapter. One design is the single-pass associative memory which utilizes angle-multiplexed holograms to first associate the input with a stored object and then display the object the input is most like. The other design is similar on the first pass through the

resonator to the single pass system, but the resonator system compares the feedback with the input and sets up a gain competition between allowable modes in the resonator until one mode of the resonator wins over the others.

In the next chapter, the process of two-wave coupling within $BaTiO_3$ will be investigated. During this investigation, the theory behind two-wave coupling will be discussed, along with applications of $BaTiO_3$.

IV. TWO-WAVE COUPLING

4.1 Introduction

The gain required for optical information processing within the confocal resonator is provided by two-wave coupling in barium titanate crystals. Two-wave coupling was operationally defined to be where a probe beam and a pump beam are directed onto a nonlinear crystal and the nonlinear crystal directs energy from one beam into the other beam depending on the direction of the positive c-axis of the crystal. Within this chapter, this definition is expanded upon with the theory of the physical process, the mathematical model, and some practical applications of two-wave coupling.

4.2 Physical Process

Two-wave coupling is a product of the photorefractive effect in nonlinear electro-optic crystals. Two-wave coupling is another term for volume holography in electro-optic crystals. The photorefractive effect refers to light induced refractive index changes in electro-optic materials and it arises from non-uniform illumination of the crystal [12:1297][19:206]. Within this section, the physical process of the photorefractive effect and how it relates to two-wave coupling is investigated.

In two-wave coupling, the non-uniform illumination originates from the interference of the mutually coherent pump and probe beams within the crystal. It is important the pump and probe beams are coherent or there will be no interference between the two beams. A simple example is two plane waves interfering and fringing in a Michelson Interferometer. This interference will lead to an intensity variation as seen in Figure 17a. The light in the fringes, both bright and dark, interact with the crystal molecules to create free charges with a given probability per photon. Thus, the crystal molecules within the bright fringes have a much higher amount of free

32
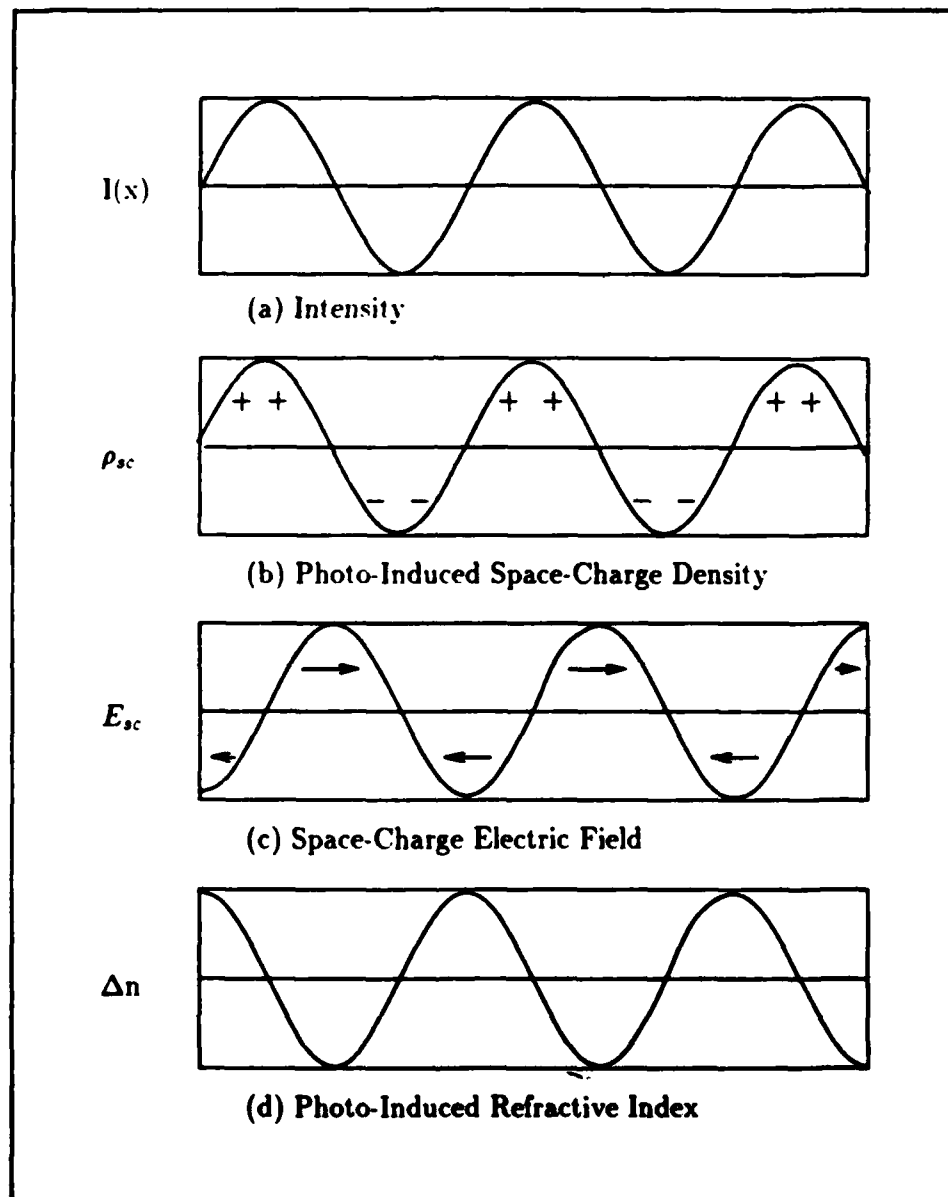
Figure 17. Photoelectric Effect. It is assumed in this diagram that electrons are the dominate photocarrier [19].

charges [12:1298]. For the purpose of this demonstration, I will assume that the electrons are the dominant charge carriers over holes. The crystal carriers which are referred to as holes and electrons are analogous to those in semiconductor theory. In the bright fringes, electrons are freed by the light and migrate leaving holes behind until they are retrapped in an area of the crystal that is not illuminated as brightly (see Figure 17b). The spatial variation in charge density forms an internal space-charge electric field (see Figure 17c). These internal electric fields produce refractive index changes by the (Pockel's) linear electro-optic effect [12:1297]. The depth of the changes in index of refraction is determined by the magnitude of the electro-optic coefficients which are a measure of how susceptible a material is to an applied electric field. The refractive index changes are periodic and result in a diffraction grating which deflects energy in the direction of the shift of the space-charge electric field with respect to the space-charge density. This results in an amplification of the probe beam by deflecting energy into its direction. An important point to remember about the amplification is that it is coherent. In other words, the probe and pump beams retain their original phase functions, only their amplitudes change. This point is discussed further along with possible applications in Appendix C.

The exact acceptors and donors of free charges in barium titanate are unknown. There are two models that are used to describe the photoelectric effect in $BaTiO_3$ [40:3363]. The first says that there is one photoactive species or recombination centers existing in two valence states and the other says there are two independent photoactive species or recombination centers. In Model 1, electrons are photoionized from donors N and recombine at traps N^+, and holes are photoionized from acceptors N^+ and recombine at N (see Figure 18a). In Model 2, one of the independent species has a dominate electron carrier and the other a dominate hole carrier (see Figure 18b). It is important to know how these two models differ in observed effects should the effects be seen. According to Valley, the following effects should be seen [40]:

Conduction Band

N^+

N

Valence Band

h

(a) Model 1

e

N_D^+

$N_D - N_D^+$

$N_A - N_A^-$

N_A^-

h

(b) Model 2
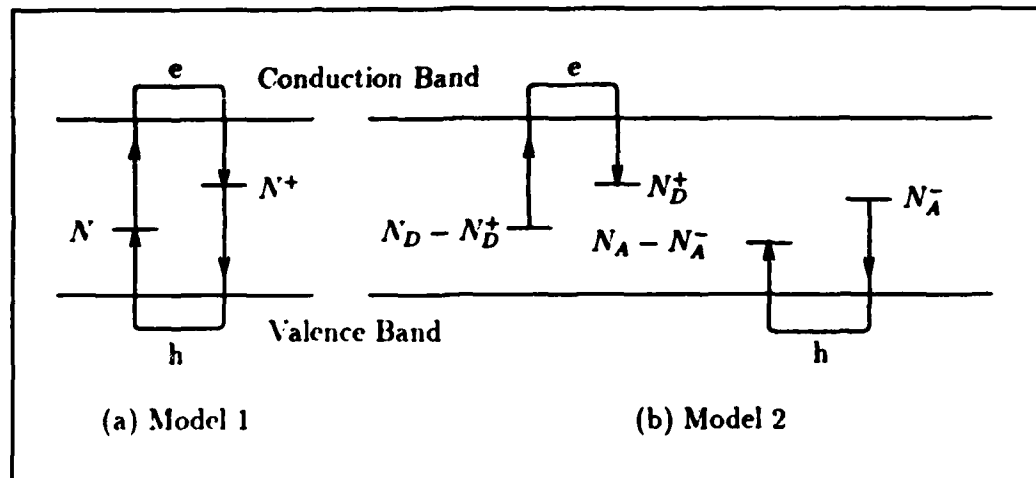
Figure 18. Charge Transport Models [40].

The results obtained here show that if a single set of recombination centers is responsible for both electrons and holes, then the carrier with the largest conductivity dominates for large grating periods, while the carrier with the largest absorption coefficient dominates for small grating periods. On the other hand, if there are two sets of recombination centers, the sign of the space-charge field is given by the sign of the carrier with the largest empty trap density.

This means the direction of energy transport depends on the concentrations of carriers in Model 2 as opposed to the differences in the conductivities or the absorption coefficients in Model 1.

As noted above, not everything is known about the material $BaTiO_3$; however, enough is known to mathematically model some of the external effects.

4.3 Mathematical Model

The geometrical configuration for two-wave coupling is shown in Figure 19. All of the angles in the figure are those internal to the crystal and not external angles. The angle between the two intersecting beams is 2θ. The grating vector is
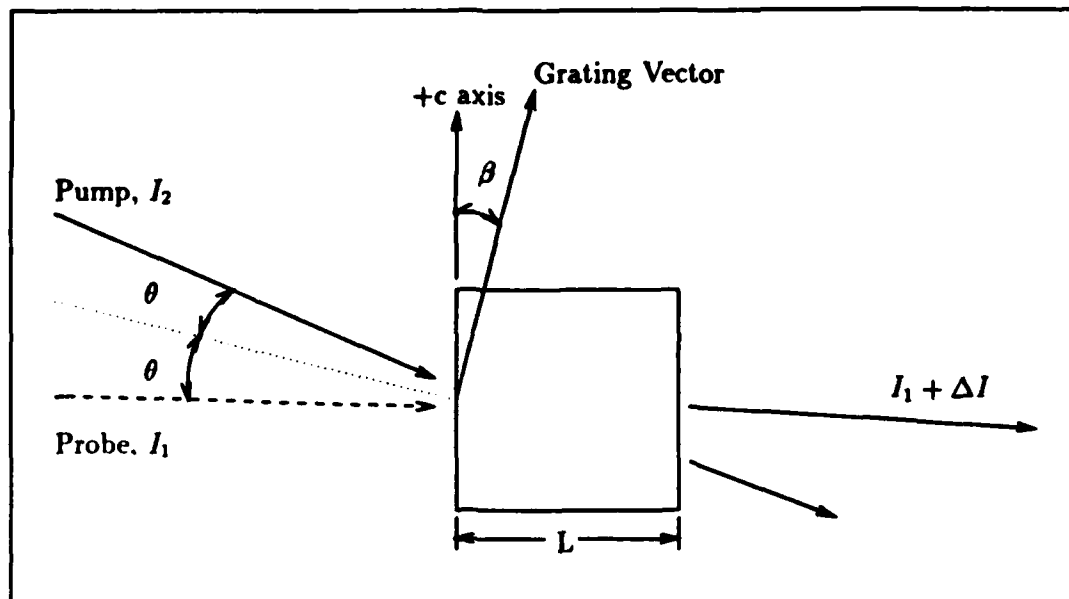
Figure 19. (= Figure 1) Geometrical Configuration for Two-Wave Coupling.

perpendicular to the bisector of the two beams. The angle between the +c-axis and the grating vector is β.

Two-wave coupling gain is defined as the effective amplification of the probe beam once the pump beam is turned on. This method of measuring the gain already takes into account the energy lost due to absorption in the material and reflection off the faces of the crystal. The equation for the gain through the crystal is:

$$G = \frac{I_1(L_{eff})withI_2}{I_1(L_{eff})withoutI_2} = \frac{[I_1(0) + I_2(0)]\,exp[\Gamma L_{eff}]}{I_2(0) + I_1(0)\,exp[\Gamma L_{eff}]} \qquad (25)$$

where Γ is the gain coefficient and L_{eff} is the interaction length in the crystal given by $L_{eff} = L/cos(\beta)$. For $BaTiO_3$ with no electric field applied, the space-charge induced grating is shifted in phase relative to the beams' interference peaks by 90°, and the exponential gain coefficient is:

$$\Gamma = \frac{2\pi}{\lambda n cos(\theta)} r_{eff} F\, Im(E_{sc}) \qquad (26)$$
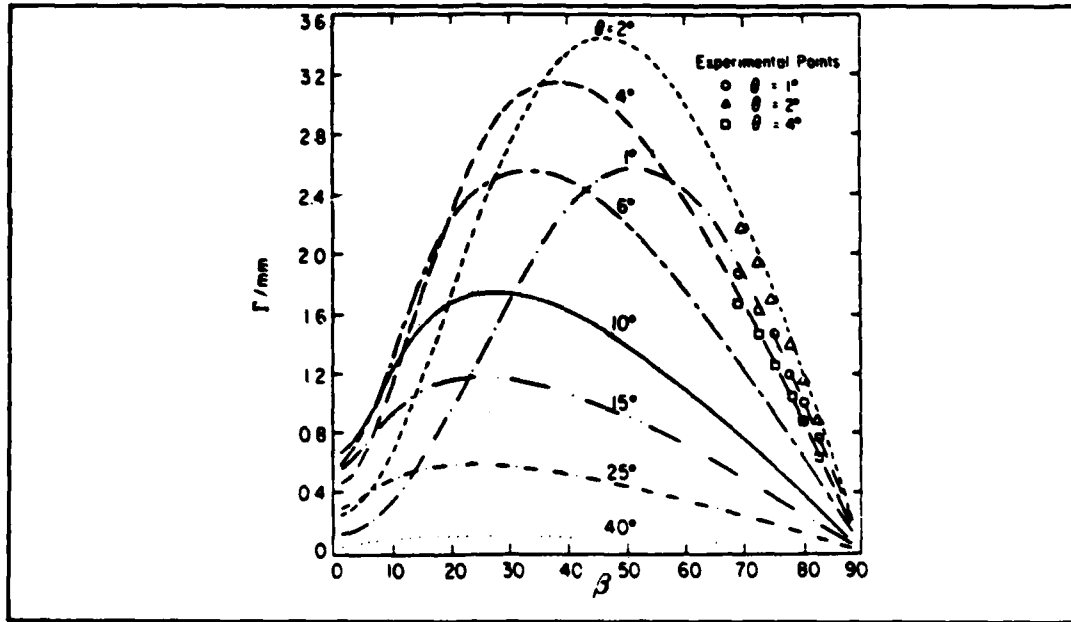
Figure 20. Two-Wave Coupling Gain Coefficient versus θ and β. Note that the peak gain is at $\beta = 45°$ and $\theta = 2°$ [11].

where

$$r_{eff} = r_{ordinary} = n_o^4 r_{13} cos(\beta) \tag{27}$$

$$= r_{extraordinary} = \frac{1}{2}cos\beta \, [n_o^4 r_{13}(cos2\theta - cos2\beta)$$

$$+ 4n_e^2 n_o^2 r_{42}sin^2\beta$$

$$+ n_e^4 r_{33}(cos2\theta + cos2\beta)] \tag{28}$$

and F is a fractional poling factor which provides for the fact that the crystals are not fully poled in the manufacturing [21:4902]. Poling will be explained in the next paragraph.

Lee has plotted the Γ curve for different geometrical configurations of θ and β (see Figure 20) [11:230]. This graph shows how dramatic the differences in gain can be for the different geometries.

37

Poling refers to a two-step manufacturing process which removes 90° and 180° domains from the crystal [34]. 90° domains are evidenced by the presence of highly reflecting planes running along the (100) planes. They are removed by putting mechanical pressure on the faces of the crystal. It is easy to see when the crystal is free of the 90° domains. The second step is the removal of the 180° domains by placing an electric field of 1000 to 1600 V/cm for six to eight hours across the heated crystal (131°C). It is very difficult to determine if all of the 180° domains are removed during this procedure. It is the remaining 180° domains which reduce the electro-optic coefficients to less than their perfectly poled values [21:4902]. Therefore, the crystals do not achieve the optimum electro-optic coefficients reported for $BaTiO_3$.

The components of Equation 26 will now be looked at in more depth. The reason to disect this equation more is because a simple relation between the fractional poling factor. σF, and the charge carrier concentrations of the crystal. With the knowledge of the fractional poling factor and carrier concentrations of a crystal, the performance of a particular crystal can be more accurately predicted.

The assumptions which Klein [21:4902] made to arrive at the expression for the static electric field (see Figure 17c) are that the dark conductivity is negligible above an irradiance of 10 $\mu W/cm^2$, there is no applied external electric field, and the bulk photovoltaic effect is negligible. Under these conditions, the equation for the static electric field is:

$$E_{sc} = \left[\frac{\mu_h p - \mu_e n}{\mu_h p + \mu_e n}\right] \frac{E_d E_q}{E_d + E_q} = \sigma \frac{E_d E_q}{E_d + E_q} \tag{29}$$

where μ_h and μ_e are the hole and electron mobilities, p and n are the hole and electron concentrations, σ is the normalized conductivity, E_d is the diffusion electric field, and E_q is the limiting space-charge electric field.

$$E_d = \frac{k_b T 2\pi}{e \Lambda_g} \tag{30}$$

$$E_q = \frac{2e\Lambda_g}{\epsilon_0 \epsilon_r} \frac{N_+ N}{N + N_+} \tag{31}$$

38
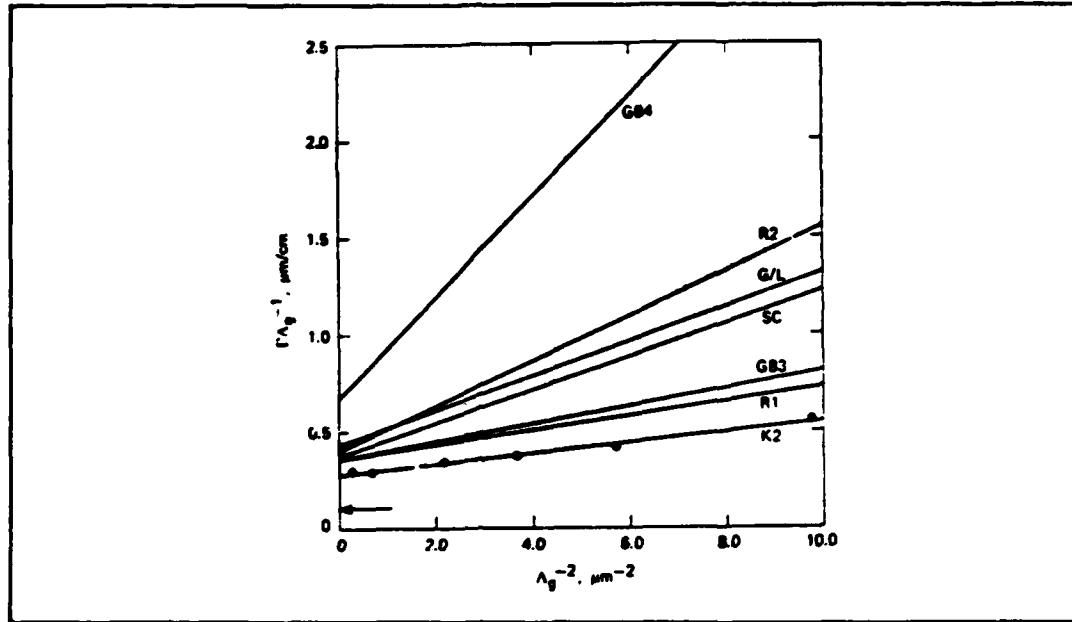
Figure 21. Fractional Poling Factor and Carrier Concentrations.   Plot of $1/\Gamma\Lambda_g$ versus $1/\Lambda_g^2$ can be used to determine the fractional poling factor and carrier concentration by use of the slope and intercept [21].

Λ_g is the grating period ($\Lambda_g = \lambda/2\sin\theta$), e is an electric charge, ϵ_o is the permittivity constant, ϵ_r is the relative dielectric constant, and $N_+N/(N + N_+)$ is the effective carrier concentration. The relative dielectric constant used in this thesis is $\epsilon_r = 168$ ($E \parallel c$) [34].

4.3.1 Fractional Poling Factor and Carrier Concentrations Klein and Valley

[21] have found a simple relation based on a straight line plot that can be used to find the fractional poling factor and carrier concentrations. The factor, σF, and $N_+N/(N + N_+)$ can be determined by the slope and intercept of the straight line produced by a plot of $1/\Gamma\Lambda_g$ versus $1/\Lambda_g^2$. The effects of tne factors σ and F cannot be separated; thus, it is not known whether the fractional effects seen are due to the 180° domains or the normalized conductivity. The intercept of the straight line is:

$$\text{Intercept} = \frac{\lambda\,n}{2\pi r_{eff}\sigma\,F\,E_d\,\Lambda_g} \qquad (32)$$

39

The only unknown in this equation is σF. Once σF has been solved for, the ratio $N_+ N/(N + N_+)$ can be found by equating the slope of the straight line to:

$$\text{Slope} = \frac{\Lambda_g \lambda\, n}{2\pi r_{eff}\sigma F\, E_q} \tag{33}$$

Klein and Valley plotted the results of experiments on seven crystals (see Figure 21). As can be seen from this figure, each of the $BaTiO_3$ crystals had their own unique line indicating different fractional poling factors and the ratio $N_+ N/(N + N_+)$. Klein and Valley have taken the ratio $N_+ N/(N + N_+)$ and equated this to N, the concentration of donor states in the crystal.

Therefore, with a straight line plot, the fractional poling factor and the concentration of donor states can be determined. With this information, the two-wave coupling performance of a particular $BaTiO_3$ crystal can be more accurately predicted.

4.3.2 Sign of Dominant Photocarrier From the theoretical models, Model 1 and Model 2, it was mentioned that the exact carriers are not known for $BaTiO_3$. To complicate matters more, the sign of the dominant photocarrier (electron or hole) is not known and is in fact different for each $BaTiO_3$ crystal. In Klein and Valley's research [21] and research by Schunemann *et al.* [34], eleven crystals had holes as the dominant photocarrier and four crystals had electrons as the dominant photocarrier. The external effect of which photocarrier dominates is the direction of the energy flow in two-wave coupling (see Equation 26). If holes dominate ($\mu_h p > \mu_e n$), the space-charge electric field will be positive and the gain coefficient, Γ, will be positive, indicating an energy flow in the direction of I_1 toward the +c-axis. If, on the other hand, the electrons dominate ($\mu_e n > \mu_h p$), the space-charge electric field and hence Γ will be negative, indicating an energy flow in the direction of I_2 away from the +c-axis. The method of determining the sign of the dominant photocarrier in this thesis and in the above mentioned research is by noting the direction of the energy coupling with respect to the +c-axis, which is determined in the manufacturing process. For
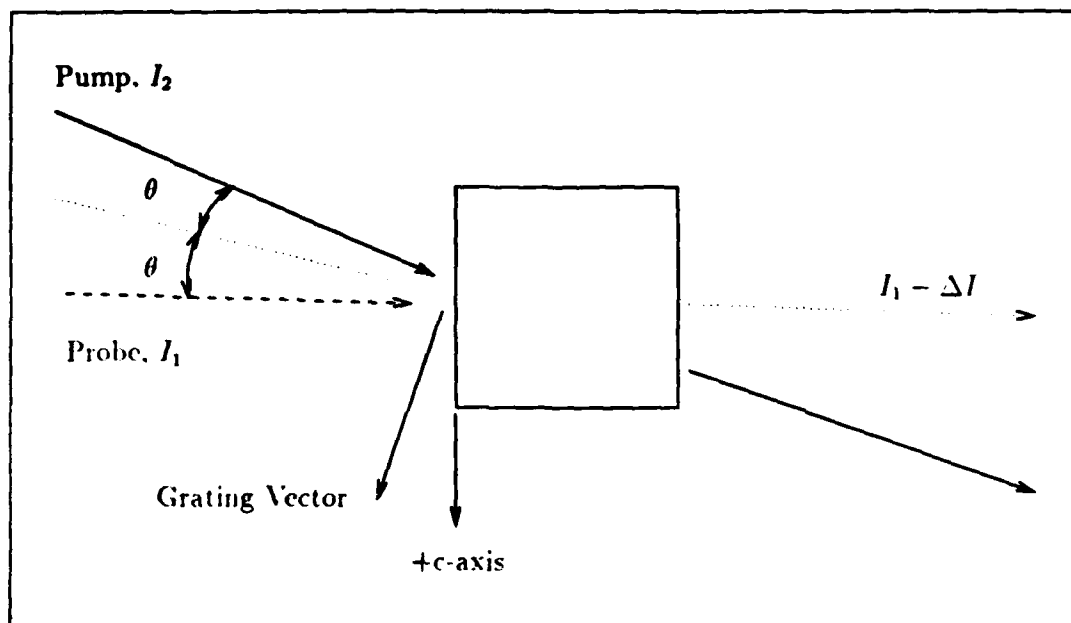
Figure 22. Attenuation With Two-Wave Coupling. Note that the crystal is turned a 180° from the orientation for gain.

the figures presented in this thesis. the dominant photocarrier is assumed to be holes unless otherwise noted.

By noting the direction of the energy gain, the energy loss is obviously in the other beam. Therefore , if gain is desired (assuming a crystal with a positive photocarrier) , the crystal and beams are oriented as shown in Figure 19. Likewise. if attenuation is desired, the crystal and beams are oriented as shown in Figure 22.

Theoretically, the gain coefficient magnitude, $|\Gamma|$, should be the same for the two configurations; however, experiments have shown there is an asymmetry of the gain coefficient [25]. This asymmetry has been attributed to an intensity dependent absorption coefficient. This asymmetry will not cause any problems in the use of the crystals in the resonator, but it will require the thresholding crystal, C1, to be characterized in the configuration of Figure 22.
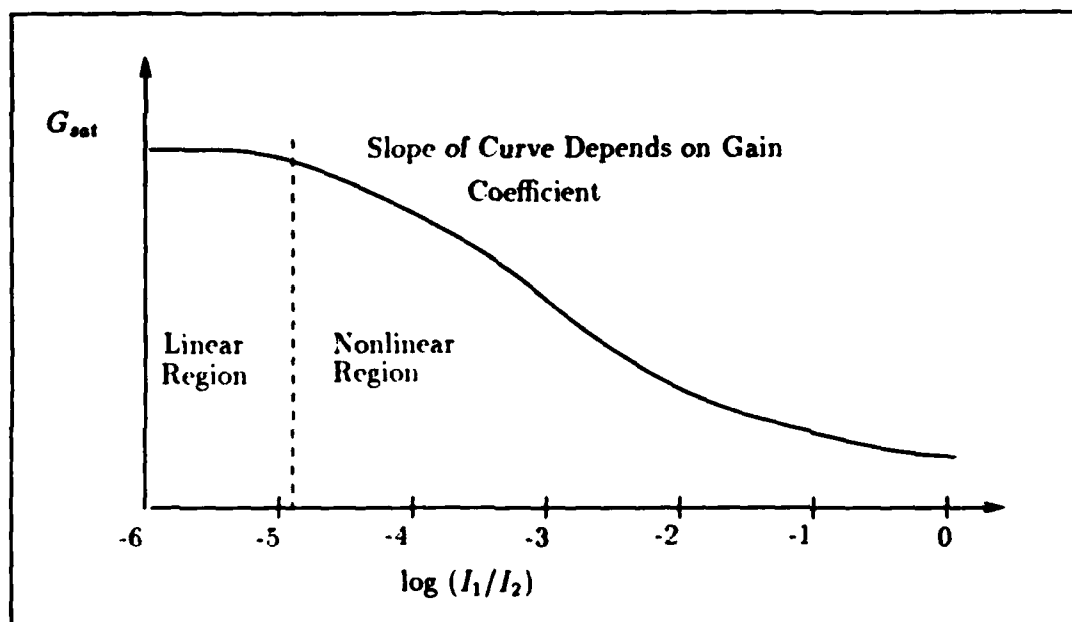
Figure 23. Two-Wave Coupling Gain versus I_1/I_2. This plot is made from Equation 25 with a gain coefficient greater than 1.

4.3.3 Saturation of Gain and Loss One point that must be remembered in the design of optical amplifiers and attenuators is that like any real world electronic amplifiers, $BaTiO_3$ gain in two-wave coupling is subject to saturation. Considering Equation 25, when the ratio of I_1/I_2 is small ($I_2/I_1 \gg exp(\Gamma L_{eff}) > 1$), the equation reduces to [11]:

$$G_{sat} = exp(\Gamma L_{eff}) \tag{34}$$

Note that the equation is independent of the ratio of the beam intensities in the approximation that I_1/I_2 is small. Therefore, the gain becomes constant over an input range which meets the approximation. This constant gain allows $BaTiO_3$ to operate as a linear amplifier.

The other end of the spectrum is when $I_1 \geq I_2$. In this case, a gain greater than two cannot occur because the energy is not physically there in the pump to allow for anything greater. The pump energy is depleted in these cases. By depletion, it

42
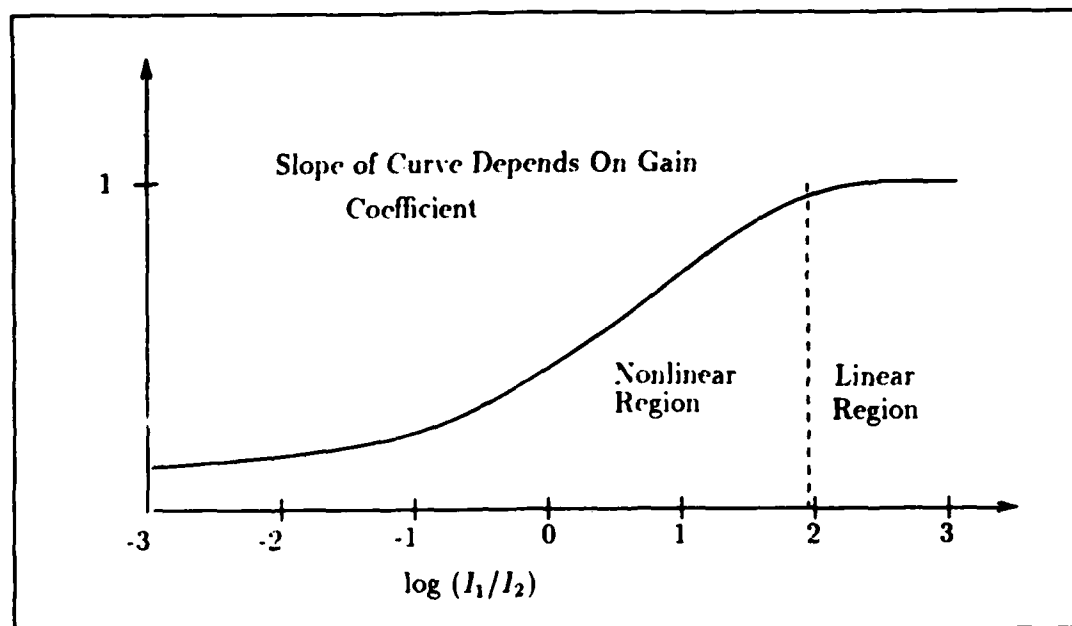
Figure 24. Two-Wave Coupling Attenuation versus I_1/I_2. This plot is made from Equation 25 with a gain coefficient less than 1.

is meant that the pump beam is no longer its original intensity.

The two-wave coupling gain as a function of I_1/I_2 is plotted in Figure 23 [11:229]. Depending on the application desired, the nonlinear regions in the gain can be a help or a hindrance. Where a nonlinear gain is desired, operation within the nonlinear region in Figure 23 is a must. For crystal C2 (Chapter 2), a linear response is required; therefore, the crystal operating region needs to be limited to the region where I_1/I_2 is small as discussed above. This "biasing" of the crystal to operate in a particular region of the gain curve is analogous to the biasing of a transistor to operate in a particular region of its gain curve. Biasing for linear operation is straight forward. Given a known variation in the probe beam intensity, $I_1 + \Delta I_1$, I_2 is selected based on the small I_1/I_2 approximation. The biasing for crystal C1 is based upon the nonlinear behavior desired. In the case of the thresholding operation required in the associative memory, a large signal is required to be passed through

43

the crystal with little or no attenuation, but a small signal is to be attenuated a greater amount. The attenuation curve for crystal C1 is as shown in Figure 24 in the nonlinear operating region.

4.4 Summary

Photorefractive crystals can be used to provide amplification or attenuation through two-wave coupling. Although the exact photocarriers within $BaTiO_3$ are not known, enough is known to model two-wave coupling. Attenuation can be provided with $BaTiO_3$ by rotating the crystal 180° from the orientation providing amplification. Both the amplification and attenuation in $BaTiO_3$ can be linear or nonlinear.

In the next chapter, the experiments conducted on the crystals, resonator and holographic plates are presented along with the experimental results. These experiments are very important to the understanding of how the components will act as a whole in a system performing an optical algorithm. The discussions within the following chapter are detailed so that the experiments can be reproduced by fellow researchers.

V. $BaTiO_3$ CRYSTAL TESTING

5.1 Introduction

Within the next three chapters, the testing of the components used in this thesis is described. The purpose of this testing is to understand the operation of each component, to investigate their unique properties for possible applications, and to predict each component's behavior in the optical associative memory. The component whose operation is the least known about is the $BaTiO_3$ crystals because of how little is known about the precise nature of the atomic interactions within the material and because of the new 45°-cut crystal to be used. Therefore, the testing of the $BaTiO_3$ crystals will be described first in this chapter, followed by the confocal resonator, and photographic film holography in later chapters. In the process of testing these components, three different laser sources were used: a Spectra-Physics Model 2020 Argon laser operating at 488 nm, a Coherent Innova 100 Argon laser operating at 514.5 nm, and a Coherent CR-699 Ring Dye laser operating at 575 nm. The reason three lasers were used is because the experiments were moved from AFIT to the Air Force Wright Aeronautical Laboratories (AFWAL) after the AFWAL facilities were set up.

5.2 Testing of $BaTiO_3$ Crystals

$BaTiO_3$ crystals are known to vary greatly in their behavior from crystal to crystal as discussed in the Summary of Current Knowledge. Therefore, the crystals used in this thesis must be understood not only within the class of $BaTiO_3$, but as individual crystals. In order to keep the performance of each crystal separate, the crystals will be referred to by its cut and by its manufacturing lot number. Three crystals are used in this testing and are labeled as follows:

1. Crystal No.115, 45°-cut

45
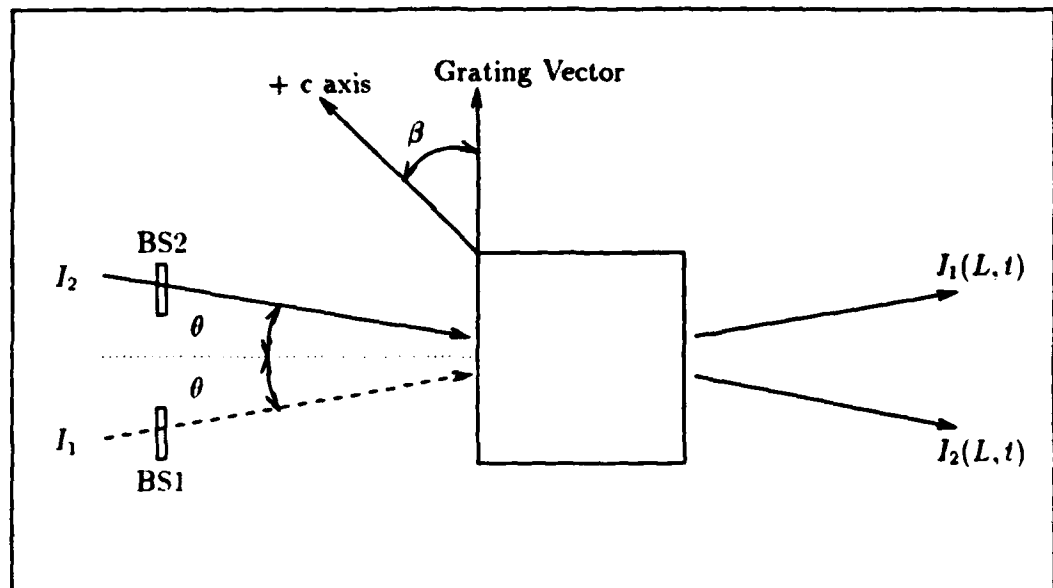
Figure 25. Setup for Two-Wave Coupling Experiments. Note that the beam splitters are used to check for self-pumped phase conjugation. Pictured is the 45°-cut crystal.

2. Crystal No.119, z-cut

3. Crystal No.133, 45°-cut

The information provided within this chapter is detailed. The reason for providing this level of detail is because this thesis is a springboard for future research at AFIT. It is therefore important that follow-on efforts know exactly what was performed in each experiment.

5.2.1 Testing Procedures The two-wave coupling experimental setup used to test the crystals is shown in Figure 25. The detailed test plan used for two-wave coupling is contained in Appendix A. It is important to note that the gains demonstrated during the testing of the crystals have exhibited highly variable behavior (i.e. the gain may be 25 one time and 35 the next). This variability is a consequence of the physical process involved of charge transfer and diffraction gratings. The charge

transfer process is also sensitive to such external factors as beam stability, uniformity, degree of polarization, and angle of polarization. All beams used in the testing process were collimated beams with spot sizes greater than three times the crystal dimensions to assure beam uniformity. Measurements at 488 nm were performed with an uncovered table; where as, the measurements at 514.5 nm and 575 nm were performed with a covered table to minimize any effects of beam instability due to air currents. All of the lasers used had a degree of polarization > 99% by measuring the maximum transmitted beam through a polarizer compared to the minimum beam transmitted. The inclination of the linear polarization was set to within $\pm 1°$ by use of a linear polarizer and a polarization rotator.

A special note on the care of the $BaTiO_3$ crystals. $BaTiO_3$ is a very temperature sensitive material which was learned first-hand during this research. If the material goes above 133° C or below 6° C, the material will change structure [32]. The lower temperature of 6° C was exceeded during the process of immersion of the crystal into index matching fluid and the subsequent cleaning of the crystal with acetone. It was found that this was a common procedure, but that extreme caution needs to be used in the cleaning process due to the lower temperature limit. The day of the mishap, the lab was 16° C, and the almost continuous cleaning of the crystal with acetone resulted in a lowering of the crystal's temperature by the fast evaporation rate of acetone. The result was, when the crystal rose above 6° C, a 90° domain shift was evident in the crystal. This domain shift was able to be removed from the crystal by the manufacturer, but valuable research time was lost while the crystal was at Sanders. Therefore, if it does become necessary to clean the $BaTiO_3$ crystal, care must be taken to clean the crystal slowly so as not to lower the temperature of the crystal below 6° C.

5.2.2 *Testing Results* Overall, the results of the two-wave coupling experiments were not as expected. The first crystal to be tested was No.115, 45°-cut. With no experience in two-wave coupling before testing this crystal, the 45°-cut crystal

47

$$2\theta_{ext} = 6.3°$$

$$\beta = 45°$$
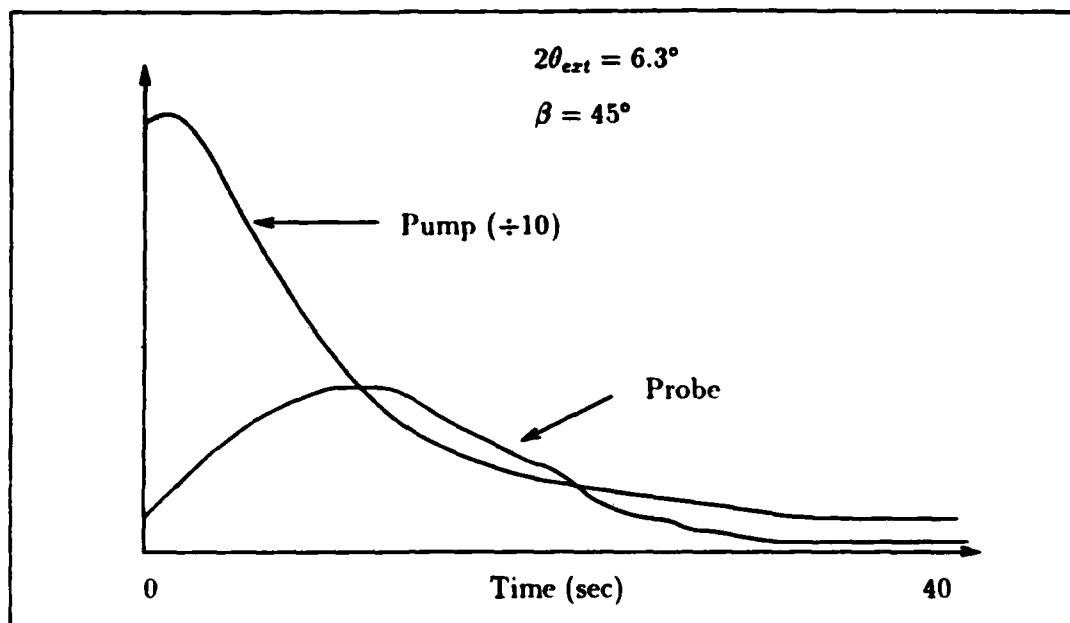
Figure 26. Two-Wave Coupling Time Response for 45°-cut $BaTiO_3$.

was very difficult to understand because its behavior was not as predicted by Lee [11]. Lee had predicted a steady-state gain on the order of 4000 which was not achieved. Instead, a time-dependent decline of the two-wave coupling was observed (see Figure 26). At the time the experiments for No.115 were being conducted, there was not another $BaTiO_3$ crystal at AFIT to compare with the behavior of No.115. Since the behavior of No.115 was so at odds with the published literature on two-wave coupling in $BaTiO_3$, it was thought that there was something wrong with the experimental setup. Since it had been published that mechanical vibrations would erase the grating being formed, vibrations were thought to be the culprit [12]. The Spectra-Physics laser was isolated from the table with foam cushions along with lowering all of the steering mirrors and lenses as close to the table as possible to minimize any vibrational coupling to the laser beam. These changes had no effect on the operation of crystal No.115. Also, by vibrating the mount of the 45°-cut crystal, the coupling decline observed could be stopped by not allowing the grating

48
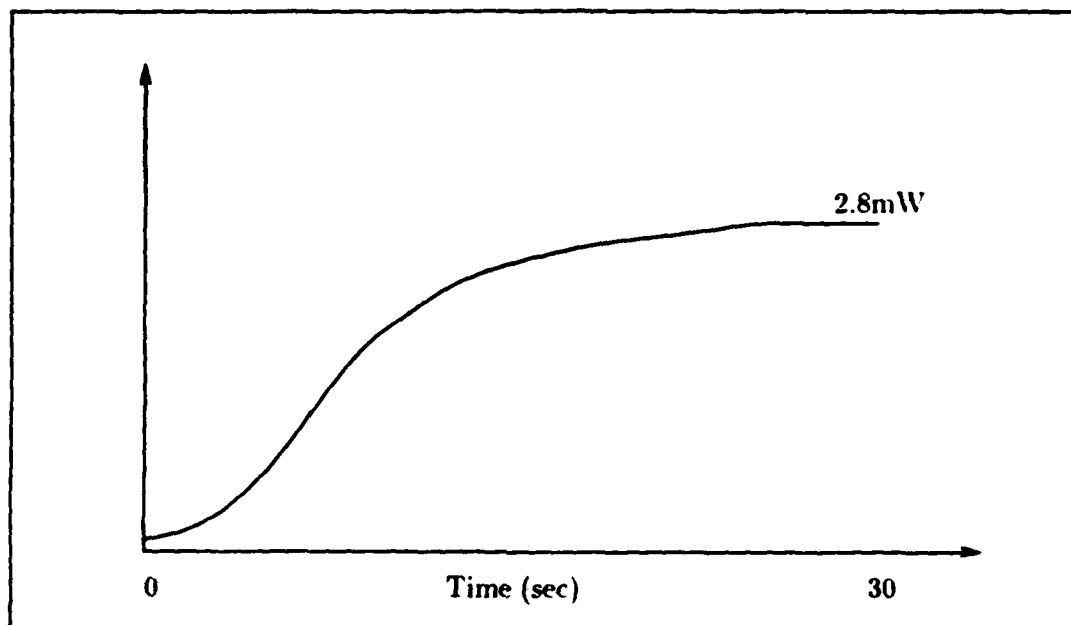
Figure 27. Self-Pumped Phase Conjugation with 45°-cut $BaTiO_3$.

in the crystal to stabilize. Therefore, it was concluded that vibrations were not the culprit for the coupling decline. The input beam paths used in two-wave coupling were checked for a self-pumped phase conjugate return along the input beam paths and none was noted. An experimental test setup was made with crystal No.115 as a self-pumped phase conjugate mirror to see if the phase conjugation return exhibited the same decline in percent reflectivity, R, that the two-wave coupling exhibits in coupling gain [14] (see Figure 27). A time plot of the self-pumped phase conjugation with crystal No.133 is contained in Figure 27 and shows that no decline was observed. A more complete discussion of self-pumped phase conjugation experiments with the 45°-cut crystal is contained in Appendix B. Before continued two-wave coupling experiments were made with crystal No.115, the crystal was sent to the manufacturer to flatten the faces of the crystal. The faces were curved, resulting in a focusing of the beams similar to a convex lens. The result of these experiments with crystal No.115 was a lack of confidence in the experimental method used in the two-wave

49

coupling experiments.

Crystal No.119, z-cut, then arrived from the manufacturer. Two-wave coupling experiments were performed with No.119, and the coupling gains were as expected from the published articles (see Chapter 2). This provided the confidence in our experimental methods to say that the behavior of crystal No.115, 45°-cut is unique. The first theory of the behavior was the particular boule the crystal was made from was exhibiting properties never seen before, a time-dependent reversal of the c-axis. This time-dependent behavior was thought to be due to competition between charge carriers within the crystal (electrons vs. holes). However, this theory was discounted, but not totally refuted, when a second 45°-cut crystal (No.133) from a different boule was received from the manufacturer. This 45°-cut (No.133) crystal exhibits the same time-dependent coupling characteristics as the other 45°-cut (No.115) crystal (see Figure 41). Therefore, it is theorized that the 45°-cut crystals are unique as a class from the z-cut crystals. More about the experimental results of the 45°-cut crystals will be discussed in the following sections.

Each of the crystals will now be discussed in detail within separate sections. Two general sets of experiments are performed: one with extraordinary polarized beams to determine the gain available from the crystal, and the other with ordinary polarized beams to determine the fractional poling and carrier concentrations as discussed in Section 4.3.1.

5.2.3 Z-cut Crystal, No.119

As noted above, the z-cut crystal experimental results were as expected. The first experiments with the z-cut crystal were performed with the Spectra-Physics laser at 488 nm and then experiments were made at AFWAL using the Coherent argon and dye lasers.

5.2.3.1 Gain of Z-cut Crystal

The experiments at 488nm were performed with extraordinary polarized beams. The intensity of the pump beam was 47.7 mW/cm^2, the intensity of the probe beam was 395 $\mu W/cm^2$, the angle θ was set
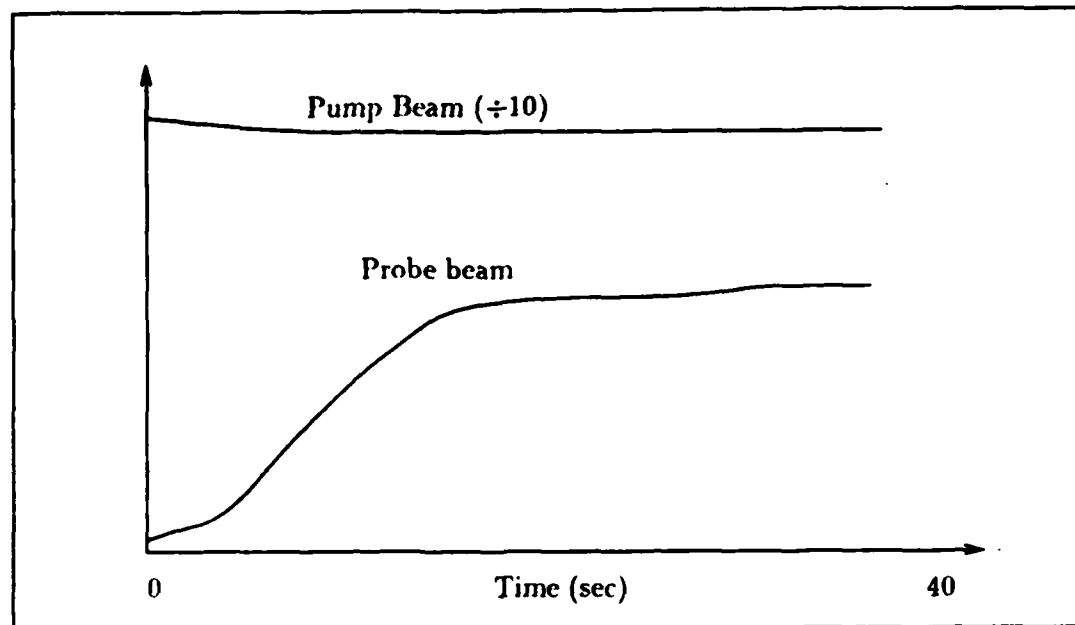
Figure 28. Two-Wave Coupling Time Response in Z-cut $BaTiO_3$.

at $1.66°$. and the angle β was varied. The time response of the two-wave coupling was exponential, and the gains recorded were steady state (see Figure 28). The two-wave coupling gain coefficient Γ versus β is plotted in Figure 29. This plot demonstrates that as β increases the coupling gain increases. Recalling Equation 28 and rewritten here, the reason for the increase in coupling at larger angles of β is due to the larger effective electro-optic coefficient.

$$r_{extraordinary} = \frac{1}{2}cos\beta \, [n_o^4 r_{13}(cos2\theta - cos2\beta)$$
$$+ 4n_e^2 n_0^2 r_{42}sin^2\beta$$
$$+ n_e^4 r_{33}(cos2\theta + cos2\beta)]$$

The reason the curve starts to decrease at larger angles can be attributed to a depletion of the pump beam. An assumption made in the mathematical derivation of coupling gains is that the pump beam remains undepleted. From the experiments conducted within this thesis, the requirement for a undepleted pump beam translates into—if the pump beam loses $\approx 15\%$ of its intensity it starts to become depleted and

51
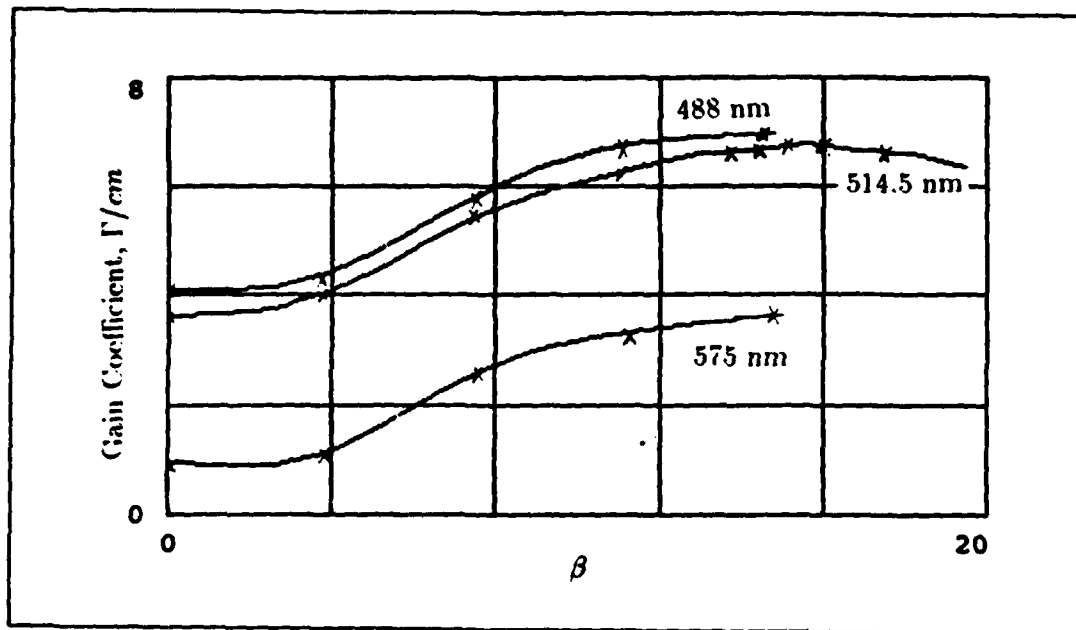
Figure 29.   Two-Wave Coupling at $\theta = 1.66°$ for Z-cut $BaTiO_3$.   Note that the gain starts to drop off after $\approx 16°$.

no longer follows the predicted values. There are two processes which can deplete the pump beam. The first is the amplification of the probe beam by two-wave mixing as explained in Chapter 4. The second is a process called beam-fanning. Since beam-fanning will be mentioned several times throughout this chapter, it is essential an understanding of beam-fanning is developed.

Beam-fanning is the result of an index gradient which is formed within a crystal with large electro-optic coefficients (i.e. $BaTiO_3$) when illuminated with light [15]. The mechanism responsible for beam-fanning is the photoelectric effect. The intense pump beam generates charge carriers within the crystal which migrate to regions that are not as intense. Thus, a space-charge electric field is developed which causes an index gradient in the crystal that deflects the pump beam in the direction of the +c-axis. Beam-fanning increases as the angle β is increased because of the larger electro-optic coefficient, r_{42}, present at larger angles of β. Beam-fanning spreads the

52
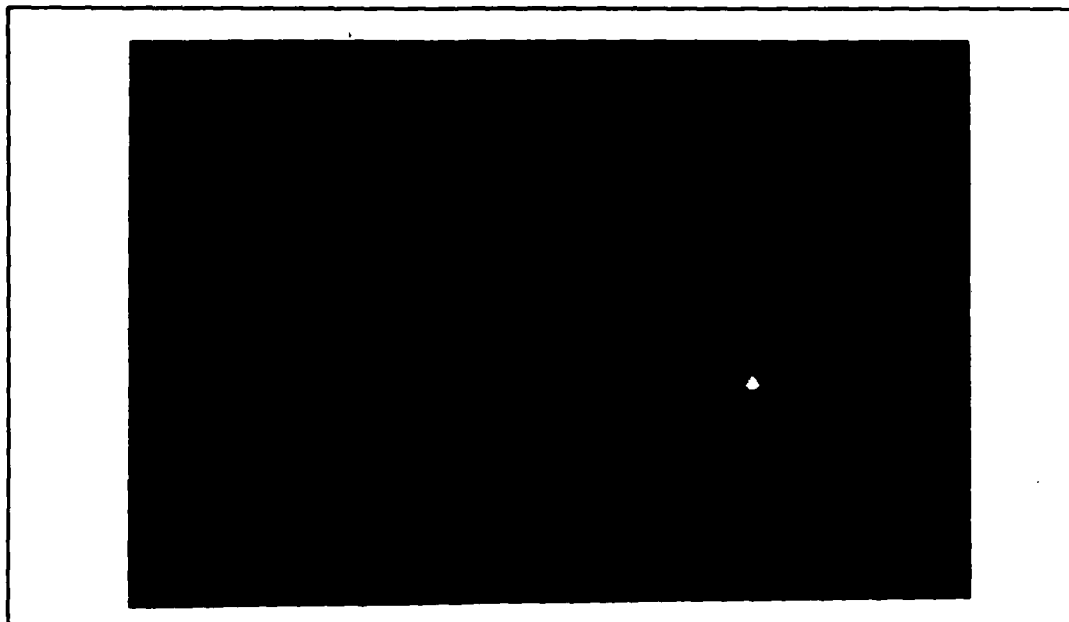
Figure 30. Beam-Fanning of Z-cut Crystal with Normal of the Input Beam 8.2° to the +C-axis. Only the pump beam is incident on the crystal in this photograph. Note that the intense spot is where all of the beam should be; However, energy is spread to the left by beam-fanning.

energy of the pump beam out, thereby, reducing the intensity of the pump beam (see Figure 30).

This experiment was then reaccomplished at 575 nm and at 514.5 nm with a noticeable change in the gain coefficients (see Figure 29). It was expected that the gain coefficients would vary between the wavelengths, because of the $1/\lambda$ factor in the Γ equation. However, an increase in gain at 514.5 nm above the gain at 488 nm was unexpected. However, after research it was found that this effect has been seen previously by Motes in his experiments on intensity-dependent absorption within $BaTiO_3$ [25]. Therefore, it has been shown that two-wave coupling gain does increase with increasing β, and that the gain coefficient at 488 nm is greater than the gain coefficients at 575 nm which demonstrates the inverse relationship of wavelength and gain shown in Equation 26. The gain at 514.5 nm was seen to be greater than

53
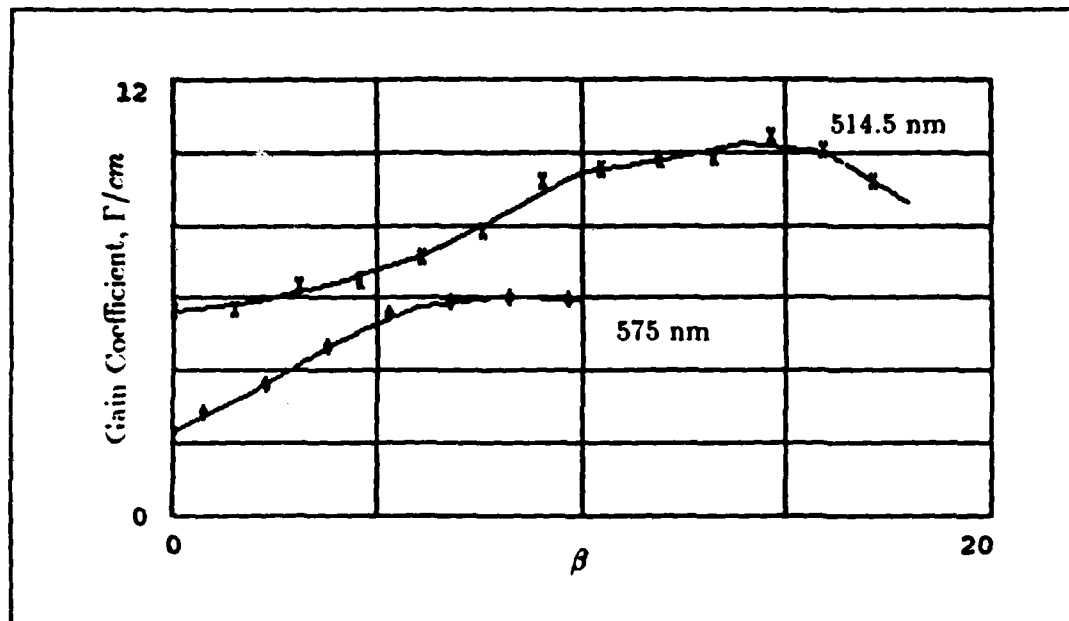
Figure 31.   Two-Wave Coupling at $\theta = 6.6°$ for Z-cut $BaTiO_3$.   Note the drop off in
gain at $\approx 9°$ for 575 nm and $\approx 15°$ for 514.5 nm. This is because the pump
power (thus beam-fanning) in the 575 nm experiment was greater than the
514.5 nm, but I_1/I_2 was kept constant. Therefore, the greater beam-fanning
causes the pump to be depleted earlier.

the gain at 488 nm and 575 nm. These experiments were also performed at $\theta = 6.6°$
($2\theta_{external} = 32°$) because this angle is to be used in the resonator. This angle is
the smallest angle which can be brought into the resonator for crystal C2. The gain
curves for this angle at 575 nm and at 514.5 nm are shown in Figure 31. As can be
seen in this figure, the gain at 514.5 nm remains greater than the gain at 575 nm. It
is also noted that the gain is greater at $\theta = 6.6°$ than 1.66° which was not predicted
by Lee for extraordinary waves [11]. Therefore, if follow-on research requires more
gain than that found here, then it is recommended that angles of θ greater than
6.6° be tried, even though the theory as presented by Lee recommends an angle
of approximately 2°. The gain received here of 125 ($\approx 1/125$ for attenuation) is
more than enough for the purpose of the nonlinear attenuation required within the

resonator. This attenuation determines the slope of the attenuation; whereas, in the resonator the only concern is that a nonlinear attenuation is provided and not the slope of the attenuation.

In the next section, the fractional poling factor and carrier concentrations of the z-cut crystal are calculated based upon measurements performed with ordinary polarization and the results are extrapolated to the extraordinary polarization case.

5.2.3.2 Fractional Poling Factor and Carrier Concentrations of Z-cut Crystal

The following experiment was to find the fractional poling factor and carrier concentrations for the z-cut crystal. In this experiment, ordinary polarized beams were used. The ordinary polarization was determined by the use of a sheet polarizer with its transmission axis parallel to the optics table (for extraordinary the polarizer is set perpendicular to the table). When the transmitted beam was minimized, the beam was considered to be ordinary.

The following experiment was accomplished at 575 nm with ordinary polarization. The pump intensity was 214 mW/cm^2, the probe intensity was 625 $\mu W/cm^2$, and the angle β was set at 0.5°. An angle β of 0° would have been preferable for this measurement to maximize the r_{eff} for ordinary polarizations and hence the gain changes as θ is varied.

$$r_{eff} = n_o^4 r_{13} cos(\beta) \tag{35}$$

However, at a β of 0°, reflections within the crystal superimpose a portion of the pump beam onto the probe beam output producing a measurement error. Thus, a compromise is reached of $\beta \approx 0.5°$ that allows a high r_{eff}, while the reflection from the pump beam misses the probe beam output. The experimental results are plotted with the gain coefficient Γ versus the grating period, Λ_g (see Figure 32a). This figure shows that the gain increases as θ increases due to the $(1/cos\theta)$ term in the Γ equation (see Equation 26). The second is the straight line plot of $1/\Gamma\Lambda_g$ versus $1/\Gamma_g^2$ to calculate the fractional poling factor by the intercept point of the

Gain Coefficient, Γ/cm

Λ_g

$1/\Gamma\Lambda_g$

$(1/\Lambda_g)^2$
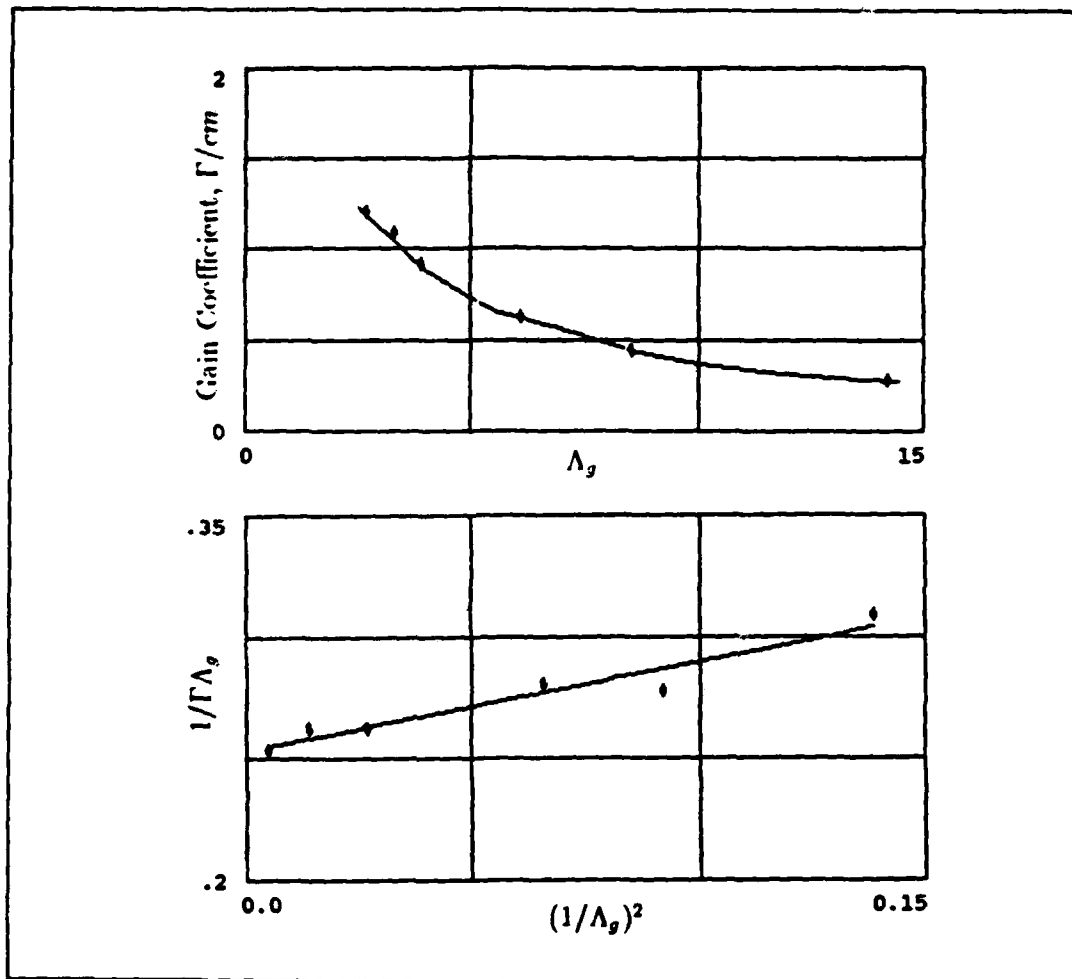
Figure 32. Gain Coefficient versus Grating Period and Straight line plot to determine the Fractional Poling Factor and Carrier Concentration.

line with the $1/\Gamma\Lambda_g$ axis and the carrier concentration with the slope of the line (see Figure 32b).

$$Intercept = \frac{\lambda\,n}{2\pi r_{eff}\sigma\,FE_d\Lambda_g}$$

$$.253 \times 10^4 = \frac{(575nm)(2.44)}{2\pi r_{eff}\sigma\,F(.16/\Lambda_g)\Lambda_g}$$

$$\sigma F = \frac{5.52 \times 10^{-10}}{r_{eff}} = .64$$

56

$$Slope = \frac{\Lambda_g \lambda \, n}{2\pi \, r_{eff} \sigma \, FE_q}$$

$$.363 \times 10^{-8} = \frac{(575nm)(2.44)\Lambda_g}{2\pi(5.52 \times 10^{-10})E_q\Lambda_g}$$

$$E_q = 1.12 \times 10^{11} = \frac{2\epsilon}{\epsilon_r \epsilon_o} N$$

$$N = 51.7 \times 10^{16}/cm^3$$

The results of this experiment were as expected and are similar to results previously published [21] [41] [34]. This experiment also reinforced Klein's argument that the unclamped electro-optic coefficients ($r_{13} = 24$, $r_{33} = 80$, and $r_{42} = 1640pm/V$) should be used for two-wave coupling with no external electric field applied [21]. If the clamped coefficients ($r_{13} = 8$, $r_{33} = 24$, and $r_{42} = 820pm/V$) are used a nonphysical result of $\sigma F > 1$ occurs.

This experiment was then reaccomplished using extraordinary beams to see if the amplification of the crystal could be predicted based upon the fractional poling factor found using ordinary polarization. During this experiment, the gain showed the same dependence on θ as seen with the ordinary polarization, but the gains achieved were consistently less than the gains predicted by the fractional poling factor. The reason the fractional poling factor is inaccurate in predicting extraordinary polarization gains is due to beam-fanning. The effects of beam-fanning in two-wave coupling is pictured in Figure 33 and with just the pump beam in Figure 30. As can be seen, the beam-fanning spreads the pump beam over a large angle (0 to $\approx 22°$ within the z-cut crystal). This results in a differential increment of the angle β as the beams propagate through the crystal and a decrease in the intensity of the beam. Therefore, what is required is a mathematical model which describes the combination of beam-fanning and two-wave coupling. An average β could be calculated by knowing the actual gain, the fractional poling factor, and the initial conditions of
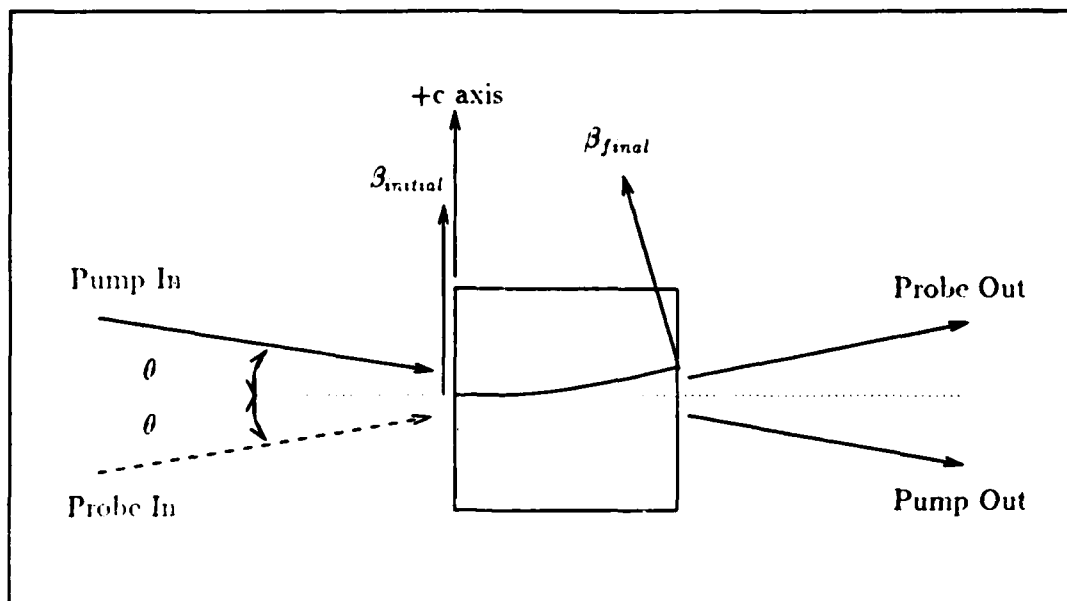
Figure 33. Two-Wave Coupling with Beam-Fanning. Note that the angle β under-
goes an incremental change throughout the volume of the crystal.

the input beams; however, this would not give an accurate picture of the volume
effects. This calculation would also only be good for the particular initial conditions
since both two-wave coupling and beam-fanning are functions of the input powers,
polarization of input beams, and the internal angles inside the crystal. Therefore,
to accurately predict the gain behavior, a combined model must be developed. This
modeling is beyond the immediate scope of this thesis, but is recommended as a
follow-on effort because work has not been performed in this area. Without this
modeling, the fractional poling factor is of limited use as a ballpark figure of what
gains should be expected with a given crystal.

   5.2.3.3 Nonlinear Attenuation with the Z-cut Crystal In the optical as-
sociative memory design, a nonlinear attenuation is required in the correlation do-
main to threshold the correlation peaks (Section 3.3). The test setup is shown in
Figure 34. Note that the +c-axis is reversed 180° from the direction used for amplifi-

Figure 34. Nonlinear Attenuation with Z-cut $BaTiO_3$.

Figure 35. Nonlinear Attenuation versus Pump-Probe Intensity Ratio.

cation. The intensity of the pump beam was 312 $\mu W/cm^2$, and the initial intensity of the probe beam was 25.7 mW/cm^2. The internal angles used were $\theta = 6.6°$ (external 16°) and $\beta = 8.2°$ (external 20°). The intensity of the probe beam was then reduced to generate the attenuation curve (see Figure 35). This curve is plotted against the theoretical attenuation curve for the initial conditions given. As can be seen, the theoretical curve matched very closely to the experimental curve.

5.2.3.4 Z-cut Crystal Operation in Image and Fourier Plane For the optical information processing algorithms, the crystals will be required to be used within both image and Fourier planes. The fi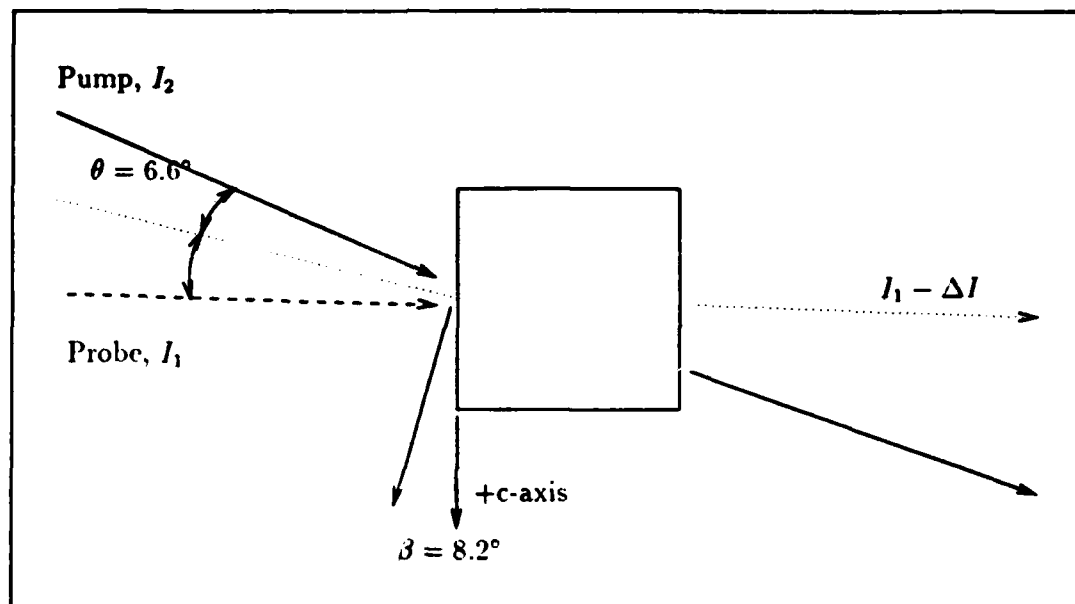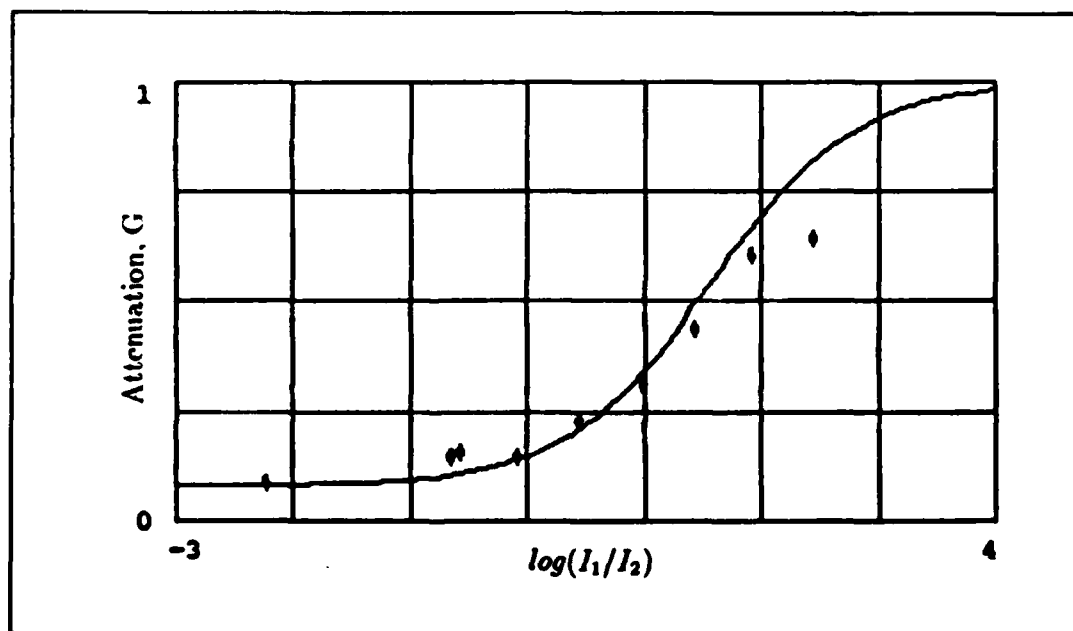rst test performed was for image amplification. The internal angles used were $\theta = 6.6°$, $\beta = 8.2°$, the intensity of the pump beam was 336 mW/cm^2, and the intensity of the probe beam was 190 $\mu W/cm^2$. The USAF resolution chart was used for determining the image quality after amplification. The resolution chart was minified by 2.16 with an 18 cm focal length lens to place groups +2 through +7 of the resolution chart into the crystal. The amplified output is then magnified to determine the maximum resolution of the crystal. Group +5 (1) could be recognized at the output which correlates to a resolution of 69.12 lines/mm.

In the second test, the crystal was placed in the Fourier plane of a 30 cm focal length lens. A 30 cm lens was used because it is close to the 35 cm focal length of the confocal resonator. The result was a real-time edge enhanced output with resolution to group 0 (6) on the Air Force resolution chart or 1.8 lines/mm resolution. The low resolution of the edge enhanced output is due to the spatial filtering performed by the crystal due to its limited size. The edge enhancement is due to the very intense DC spot in the Fourier plane. This intensity exceeds the intensity of the pump beam which results in an attenuation of the DC term. This was to be expected from the saturable gain curve presented in Figure 23 because once the intensity of the probe beam exceeds that of the pump beam a gain of less than unity is predicted. This suggests another method of achieving attenuation with $BaTiO_3$ were low intensity

60

peaks are passed, while high intensity peaks are attenuated. This edge enhancement can be eliminated by placing the crystal within the Fresnel diffraction region of the lens such that there was not an intense DC spot within the crystal or by reduction of the intensity of the probe beam. The resolution was not degraded by the slight displacement of the crystal from the Fourier plane. Therefore, with the crystals in the Fourier plane, a resolution limit is created which will limit the spatial frequency content of the objects stored within the resonator. This points to the ultimate need to improve the design of the optical associative memory. With crystal C1, which operates only on the correlation peaks, there is no problem with loss of high spatial frequencies. However, the image amplification in crystal C2 will be limited in resolution due to its placement in the Fresnel diffraction region of the mirror. As smaller resonators are built, they will have improved resolution due to less spatial separation of the Fourier terms.

5.2.3.5 Summary of Z-cut Crystal, No.119

Much has been learned about the operation of $BaTiO_3$ through the testing of the z-cut crystal. First, confidence about the experimental setup was built by comparison of experimental results with published articles. Second, it was learned that modeling the behavior of the crystal with ordinary beams to predict the behavior of extraordinary beams was of limited use unless a mathematical model is built that takes into account the effects of beam-fanning on two-wave coupling. The operation of the crystal was also investigated as a nonlinear attenuator, an image amplifier in an image plane, Fresnel plane, and Fourier plane. It was found that the crystal can indeed be used as a nonlinear attenuator, and that if the crystal is placed within the Fourier plane, the DC term can be attenuated for an edge enhanced image. The crystal was seen to be an effective image amplifier.

5.2.4 45°-cut Crystal, No.115

As mentioned in the beginning of this section, the 45°-cut crystal demonstrated effects never seen before. This effect is a time
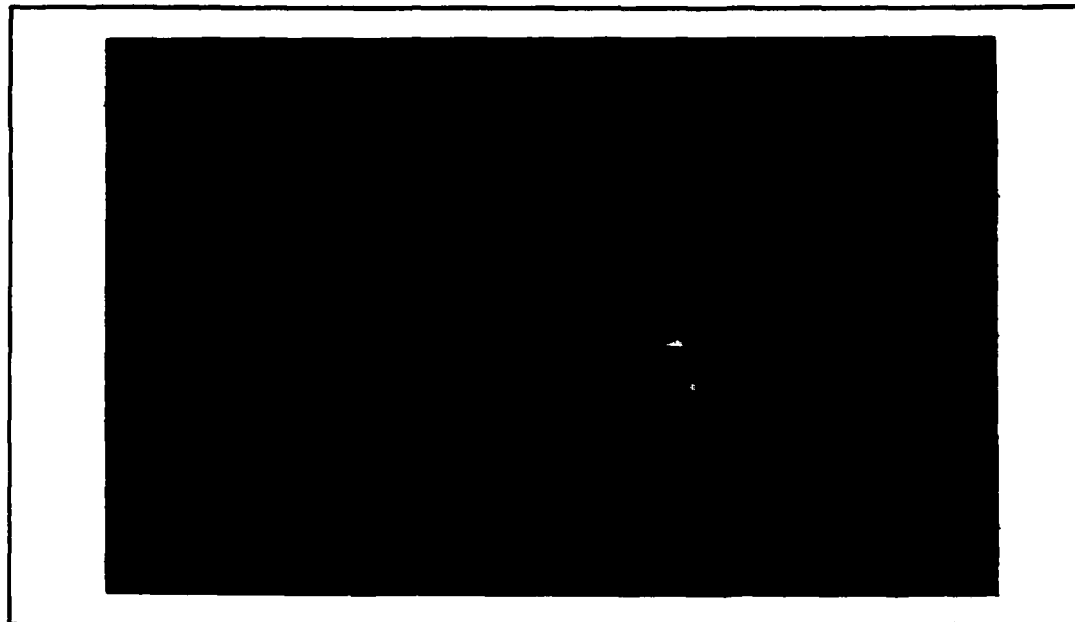
Figure 36. Beam-Fanning of 45°-cut Crystal with Input Beam Normal to the Crystal Face. Only the pump beam is incident on the crystal in this photograph. Note that the pump beam has almost completely vanished from its initial location and is spread to the left by beam-fanning.

dependent coupling gain as shown in Figure 26. By the photorefractive effect, an internal grating is formed in which energy is coupled into the probe beam. This is seen in the rising portion of the probe beam. The probe beam is then seen to reach a peak and then to decline to a minimum. While the probe is exhibiting this behavior, the pump beam is exhibiting an exponential decline in intensity. This has been attributed to beam-fanning as discussed in the previous section. Beam-fanning in the 45°-cut crystal is seen to spread the pump beam over larger angles ($\approx$ 0 to 27° inside of the crystal) than the z-cut because of the larger effective electro-optic coefficients (see Figure 36).

Because of the rise and fall of the probe intensity, the peak probe intensity will be used for gain measurements in the following section.
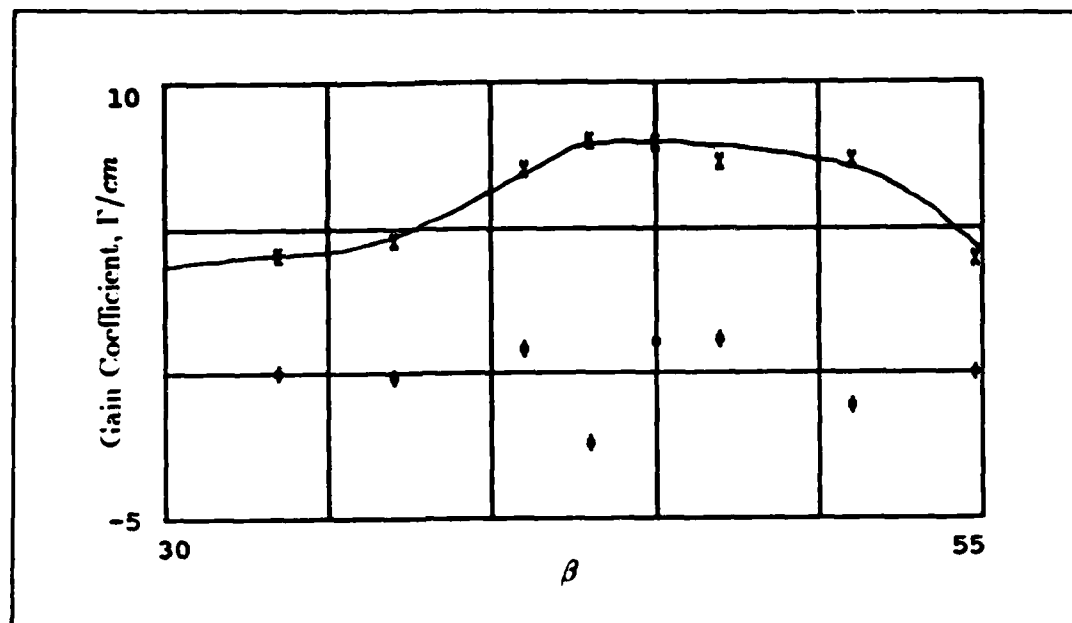
Figure 37. Two-Wave Coupling at $\theta = 1.66°$ for 45°-cut, No.115, $BaTiO_3$. The gain coefficient at the peak probe intensity is plotted with a solid line, while the steady state gain coefficient is plotted with unconnected diamonds.

5.2.4.1 Gain of 45°-cut Crystal, No.115 Not many quantitative measurements were made of the gain of the 45°-cut crystal, but much qualitative research was performed to understand the time-dependent behavior of the crystal. Two experiments performed were both taken at 488 nm with one using extraordinary polarization and the other using ordinary polarization. The extraordinary polarization tests will be discussed in this section, while the ordinary polarization test will be in the following section.

Detailed measurements were taken with the initial conditions of $\theta = 1.66°$, the pump intensity of 52 mW/cm^2, and the probe intensity of 490 $\mu W/cm^2$. The angle β was varied with the resulting gain coefficients plotted in Figure 37. A small steady state gain was noted at some angles and is plotted with a dotted line. As can be seen in this figure, for most angles the probe output with the pump beam applied was less than the original probe without the pump beam applied. It is theorized that the

63

reason there is a steady state gain at these angles is because the beam-fanned pump beam and probe beam have reached a β_{avg} which has a large effective electro-optic coefficient. θ was then varied from 1.66° to 5.6° to see if a steady state gain could be achieved with $\beta = 45°$; however, no steady state gain was noted.

5.2.4.2   Fractional Poling Factor and Carrier Concentrations of 45°-cut Crystal. No.115

Ordinary polarized beams are used to determine the fractional poling factor and carrier concentrations of the crystal as in section 5.2.3.2. The gains reported here are steady state. The reason the gains are steady state is because only the lower r_{13} electro-optic coefficient is activated; therefore, there is no appreciable amount of beam-fanning. The polarization was set with the sheet polarizer as discussed in Section 5.2.3.2. The angle β was maintained at $\approx 45.5°$ while the angle θ was varied from 1.7 to 8.8°. The intercept of the straight line plot (.101 $cm/\mu m$) was used to calculate the fractional poling factor as shown in Section 5.2.3.2 with the result being a fractional poling factor greater than 1. It is impossible to get a fractional poling factor greater than one, so a problem existed with the experimental setup.

The mathematics of the electro-optic coefficients were analyzed to determine if the polarization method chosen was bad. This is in fact the case as is shown below.

$$
\begin{aligned}
r_{ordinary} &= n_o^4 r_{13}cos\beta \\
&= (2.48^4)(24pm/V)cos(45) \\
&= 642pm/V \\
r_{extraordinary} &= \frac{1}{2}cos\beta\, [n_o^4 r_{13}(cos2\theta - cos2\beta) \\
&\quad + 4n_e^2 n_0^2 r_{42}sin^2\beta \\
&\quad + n_e^4 r_{33}(cos2\theta + cos2\beta)] \\
&= \frac{1}{2}cos(45)\,[(2.512)^4(24pm/V)(1 - cos(2\cdot45)) \\
&\quad + 4(2.48)^2(2.512)^2(1640pm/V)sin^2(45)
\end{aligned}
$$
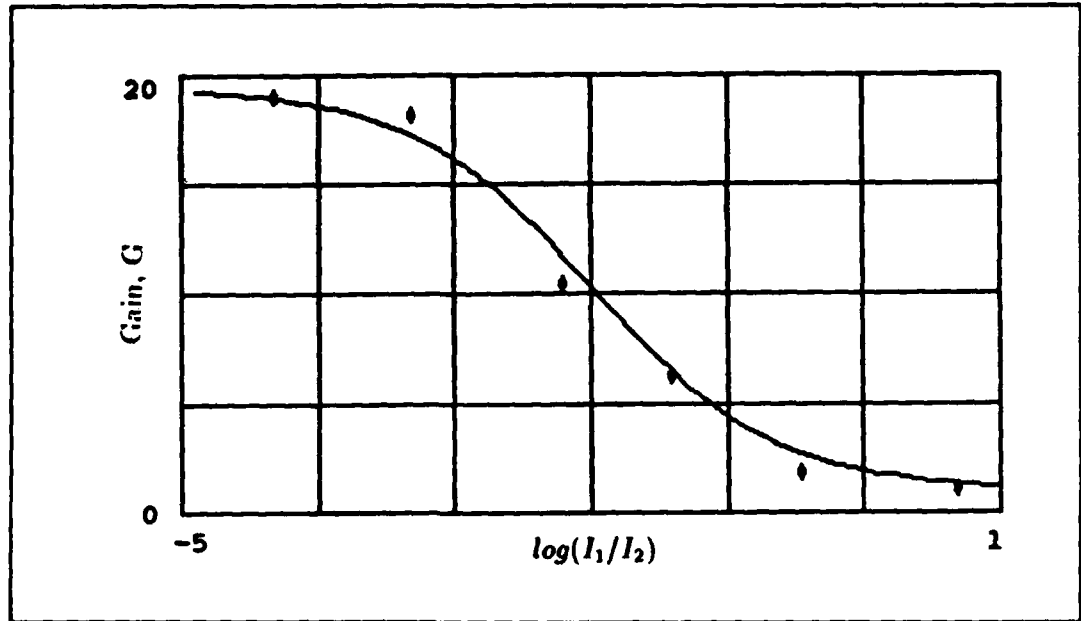
Figure 38. Saturable Gain Curve with 45°-cut Crystal.

$$+ (2.48)^4(80pm/V)(1 + cos(2 \cdot 45))]$$

$$= 12657pm/V$$

Therefore, it takes less than a degree off of ordinary polarization to influence the measurements taken in this section. Before these measurements could be reaccomplished with another method of determining the orientation of the polarization, the crystal had to be returned to the manufacturer for repair as previously discussed.

   5.2.4.3 Saturable Gain Curve Within this section, the saturable gain curve shown by Lee [11] and used by Northrop within their associative memory [27] is experimentally developed. These gains were peak gains and not steady state. The test scenario used to generate the saturable gain curve was $\theta = 2°$, $\beta = 45°$, pump intensity of 26 mW/cm^2, and an initial probe intensity of 1.2 $\mu W/cm^2$ at a wavelength of 575 nm. The probe intensity was then increased over six decades to achieve the saturable gain curve in Figure 38. Thus, $BaTiO_3$ can be used as a

nonlinear gain media, or if the probe beam intensities are limited to a region where the pump is approximately 10^5 times greater than the probe, $BaTiO_3$ can be used as a linear amplifier as discussed in Section 4.3.3.

5.2.4.4   Summary of 45°-cut Crystal, No.115   Within this section, it has been shown that the gain of the 45°-cut crystal is not appreciably larger than that of the z-cut crystal due to the large beam-fanning witnessed with the 45°-cut crystal which depleted the pump beam. It is noted that the fractional poling factor is difficult to solve for due to the large extraordinary coefficients available with just a slight misalignment of the angle of polarization. An important capability within processing systems is the ability to perform both linear and nonlinear processing. It has been experimentally shown that two-wave coupling in $BaTiO_3$ can be used to perform linear and nonlinear amplification.

5.2.5   45°-cut Crystal, No.133   Two-wave coupling experiments performed on crystal No.133 were to determine the maximum gain point to operate the crystal in the resonator, to improve the methodology of experimentally determining the fractional poling factor, and to investigate the effects of intensity of the pump beam on two-wave coupling and beam-fanning.

5.2.5.1   Gain of 45°-cut Crystal, No.133   The following measurements were all taken at 575 nm. From these experiments, an operating point for the crystal C2 within the optical associative memory will be found. First, the experiments were conducted with $\theta = 2°$ and then at $\theta = 3.5°$. For $\theta = 2°$, the experimental conditions were a pump intensity of 48 mW/cm^2 and a probe intensity of 11 $\mu W/cm^2$. For $\theta = 3.5°$, the experimental conditions were a pump intensity of 71 mW/cm^2 and a probe intensity of 263 $\mu W/cm^2$. The gain coefficients were graphed on the same figure for comparison (see Figure 39). As can be seen, the gain for $\theta = 3.5°$ was greater than at 1.66°. This was not expected from Lee's theoretical work [11]. However, it
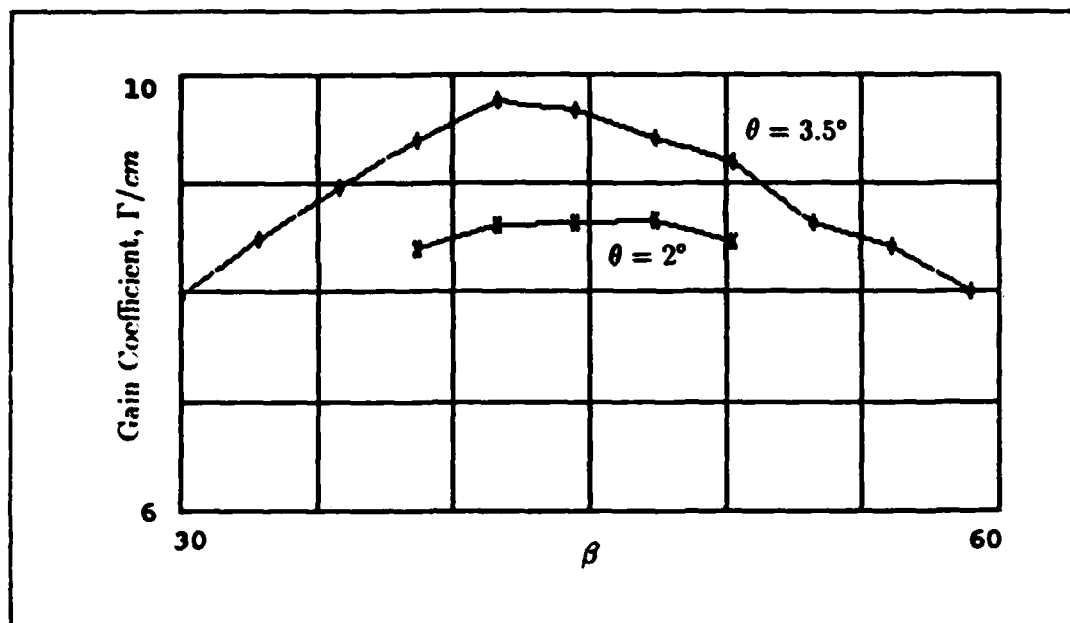
Figure 39. Two-Wave Coupling for 45°-cut, No.133, $BaTiO_3$.

does look good for the confocal resonator, since the smallest angle that can be used in the resonator for a crystal C2 pump beam is 3.5°. The maximum gain point was at $\beta = 40.6°$ which is similar to that predicted by Lee. Since the gain was continuing to increase at larger angles of θ, additional experiments above 3.5° should be conducted.

5.2.5.2 Fractional Poling Factor and Carrier Concentrations of 45°-cut Crystal, No.133 Greater success was had at determining the fractional poling factor and carrier concentrations within crystal No.133 by improving the method of setting the polarization inclination. The method used entailed minimizing the beam-fanning of the crystal by rotating the polarization. First, the polarization was set at extraordinary polarization and the beam-fanning allowed to build. A power meter was then placed within the "beam-fanned" beam, and the polarization was quickly rotated to the point that the beam was minimized. This procedure had to be performed quick (less than 5 seconds), so the minimum was found before the beam washed out the index gradient formed with the extraordinary beam. It was noted that the direction

67

the polarization rotator was turned (clockwise or counter-clockwise) had an effect on the spread of angles determined to be "ordinarily" polarized. The reason is the lost of the beam-fanning gradient as the polarization is rotated from the illumination with the laser light (diffusion of charge carriers). Therefore, the angles (five clock-wise and five counter-clockwise) were averaged together to calculate the ordinary polarization angle.

The experiment was performed with a probe beam intensity of 265 $\mu W/cm^2$, a pump beam intensity of 123 mw/cm^2, and $\beta \approx 45.5$. The fractional poling factor is calculated from the intercept point of the straight line plot (0.253 $\mu m/cm$) to be .89, and the carrier concentration is calculated from the slope (0.315 μm^{-2}) to be 4.9×10^{16} cm^{-3}.

5.2.5.3 Time Response of 45°-cut Crystal

The time response of the two-wave coupling and beam-fanning has been shown by researchers to depend on the intensity of the pump and probe beams [12] [13]. The reason for the time dependence is due to the time rate of freeing charge carriers which is proportional to the beam intensity. This is why for a more intense beam, two-wave coupling and beam-fanning occur faster (see Figure 40). In these plots, all conditions were the same between the two except that the beam intensities for the second plot were a third less than the intensities of the first plot. The result is a faster time constant for the more intense beams in the first plot.

5.2.5.4 Summary of 45°-cut Crystal, No.133

The time-dependent characteristics of No.133 and No.115 crystals were the same which gives more weight to the argument that the time-dependent behavior witnessed is due to the cut of the crystal and not a function of the boule the material came from. Proceeding from this premise, it is believed that the time-dependent behavior of the two-wave coupling is due to depletion of the pump beam from beam-fanning. An averaging method of determining ordinary polarization for the fractional poling factor test with a 45°-

36.7 $m\mathit{W}/cm_2$ Pump Beam ($\div 10$)

$\theta_{ext} = 3.5°$

$\beta_{ext} = 42°$

486 $\mu\mathit{W}/cm_2$ Probe beam

$I_1 = 260\mu\mathit{W}/cm_2$

$I_2 = 123mw/cm_2$

Time (sec)

(a)

$I_1 = 162\mu\mathit{W}/cm_2$

$I_2 = 81m\mathit{W}/cm_2$

25 $m\mathit{W}/cm_2$

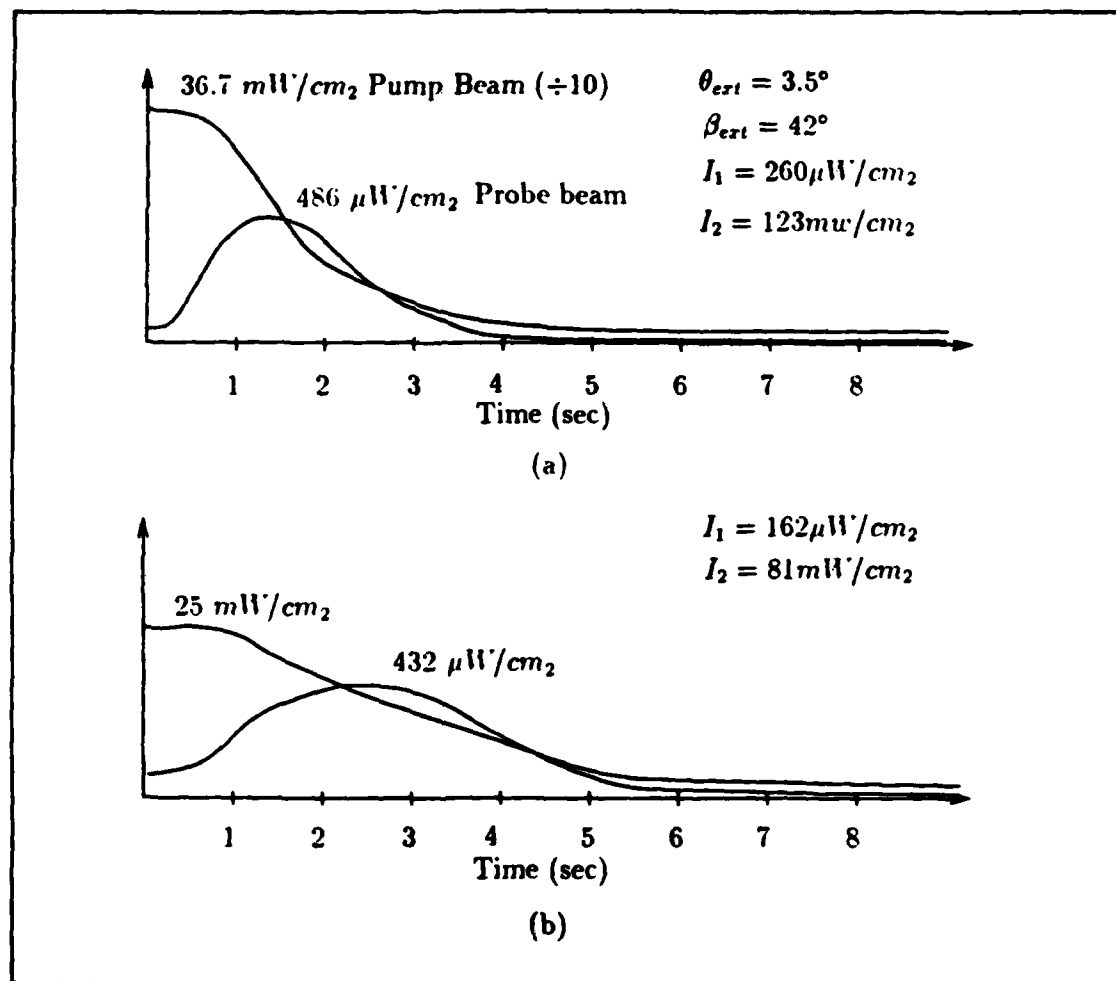432 $\mu\mathit{W}/cm_2$

Time (sec)

(b)

Figure 40.   Time Plots of Two-Wave Coupling with 45°-cut Crystal, No.133.   Note that the time constant has changed between the two plots. In plot (b), the beam intensities are a third less than those of plot (a).

cut crystal was experimentally shown to yield better performance than the polarizer method first used. It was verified that the time constants of the crystal depended upon the intensities of the input beams.

5.3 $BaTiO_3$ Ring Laser

Within this section, the operation of $BaTiO_3$ ring laser is investigated qualitatively. The crystals were placed within the resonator with a pump beam incident and no probe beam. Two crystals were used: a 45°-cut and a z-cut. Two resonators were used: the confocal resonator and a resonator formed with three plane mirrors. The output of the resonator is monitored when the pump beam is directed onto the crystal.

With the z-cut crystal in the confocal resonator, there was very little energy in the resonator beam because the crystal was just overcoming the losses in the resonator. When a neutral density filter of 0.3 (50 % transmission) was placed in the cavity the z-cut crystal no longer lased. With the 45°-cut crystal in the confocal resonator, there was considerably more energy in the resonator beam. The 45°-cut crystal easily lased with four times the losses in the resonator than the z-cut did. In both cases, the resonator beams were steady state. It is hypothesized that the reason the gains with the 45°-cut crystal are steady state is because of the beam-fanning process starts the lasing. The 45°-cut crystal initially fans a large amount of energy as seen in the two-wave coupling, but this energy is fed back into the crystal by the resonator mirrors. Thus, the resonator beam (probe) increases in intensity from the beam-fanning and is increased further by two-wave coupling. Now the difference between in the resonator and outside of the resonator becomes dramatic. In the resonator, the strong and increasing probe beam reinforces the grating that initially developed from beam-fanning and modified by the resonator beam. This is different than the two-wave coupling as presented in the previous sections, in that the probe beam was a constant beam that did not have the benefit of using the beam-fanned

70

energy of the pump.

These experiments were reaccomplished within the plane mirror resonator. In both cases (z-cut and 45°-cut), the plane mirror resonator gave greater resonator fields than the confocal resonator because there was less cavity losses. An aperture could be placed in all of these resonators to control which regions of the crystal which lased.

The results of these qualitative experiments show that the 45°-cut crystal still has promise for optical processing systems. In fact, within the ring laser the 45°-cut crystal works better than the z-cut crystal. Therefore, the first work in future research should be the characterization of the crystals within an optical resonator. Since the gain the crystal provides is just enough to overcome the resonator losses, the method of characterizing the gain of the crystal should be to add attenuation into the cavity until the crystal barely lases. This point would be the maximum gain the crystal has available for gain with the geometric configuration and pump beam intensity.

5.4 Summary

Much has been learned about the optical properties of $BaTiO_3$ in two-wave coupling. It has been verified that amplification can be achieved with these crystals, and that the amplification can be linear or nonlinear. Gains on the order of thousands have not been achieved as predicted by Lee [11], but gains on the order of a few hundreds have been achieved. An improved methodology is presented for determining the fractional poling of 45°-cut crystals. It is recommended that a mathematical model be built which combines the effects of beam-fanning and two-wave coupling. It has also been shown that steady state coupling can be achieved within an optical resonator with the 45°-cut crystal. This coupling was substantial, but it has only been looked at qualitatively. The area of coupling gain within the resonator promises to bear the most fruit as it applies to optical information processing. It

has been seen that the gain at 514.5 nm is greater than both 488 nm and 575 nm; therefore, for applications where a maximum gain is required, 514.5 nm should be used. In the next two chapters, the confocal resonator and low-angle holograms are investigated.

VI. CONFOCAL RESONATOR

6.1 Introduction

The confocal resonator consists of the Mangin mirrors developed by Lee at the University of California as discussed in the Summary of Current Knowledge. As mentioned earlier, the Mangin mirrors are unique in that the reflective surface is on the backside of the mirror and not the front side. Also, the radius of curvature of the two faces are different from each other. These two design parameters give the Mangin mirror confocal resonator improved performance over simple spherical confocal resonators [10]. The improved performance is due to the reduction of the spherical aberrations present in spherical lenses and mirrors. The specifications for the Mangin mirror set used in this thesis are in Appendix B. Before considering how the resonator is tested for performance, it is important to understand how the resonator is aligned. The alignment procedures developed are believed to be the easiest to implement; however, they are not the only possible means of achieving an aligned resonator.

6.1.1 Confocal Resonator Alignment
The confocal resonator is not difficult to align once it is known how to align and stabilize it. Before the alignment procedure is discussed; however, mention should be made of the problems encountered during the alignment of the resonator. These are related to mechanical vibrations and air currents. These are two very important factors in resonator stability. This lesson required a long time to learn in this thesis, and it is hoped this discussion will keep the reader out of similar problems. First, mechanical vibrations of the resonator and input beam must be minimized. When this thesis first began, free standing mirror mounts were used to hold the Mangin mirrors. This configuration was useless because the longitudinal spacing of the resonator could not be stabilized. The interference fringes fluctuated wildly. Next, rigidly interconnected mirror mounts were used

73
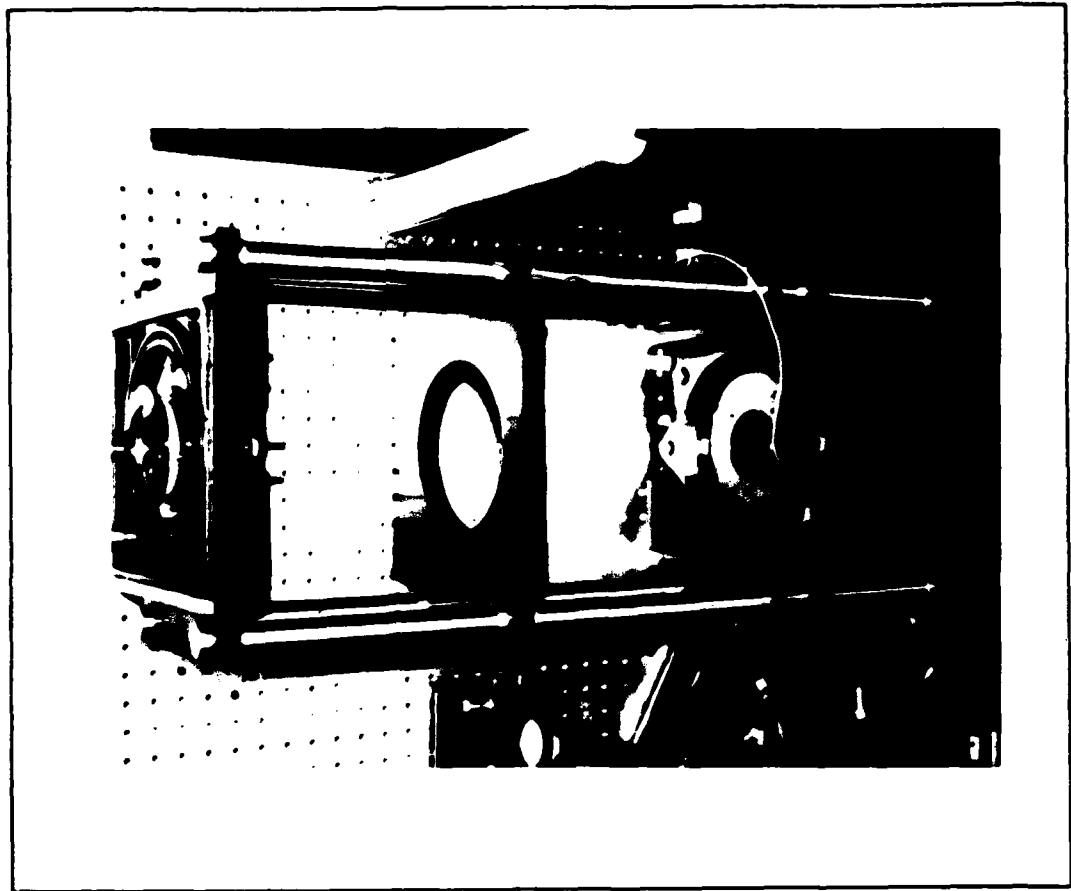
Figure 42. Rigidly Mounted Mirrors Using Burleigh 6 inch Resonator Kit.

which were specifically made for resonator use (see Figure 42). This substantially reduced the random variation of the fringes, but fluctuations still remained that the stabilization circuitry could not respond to. It was finally noted that the remaining problem was air currents. As soon as sides and a top were added to the resonator to block air currents, the fringes remained constant enough for the stabilization circuitry to handle the remaining small variations in the cavity length. Therefore, in order to perform any tasks within the resonator, the resonator must be rigidly mounted and isolated from air currents. A problem noted with the mirror set at AFWAL is that the anti-reflective coating on the front surface of the mirrors is for

Input   Output

(a) Longitudinal Misalignment

Input   Output

(b) Angular Misalignment
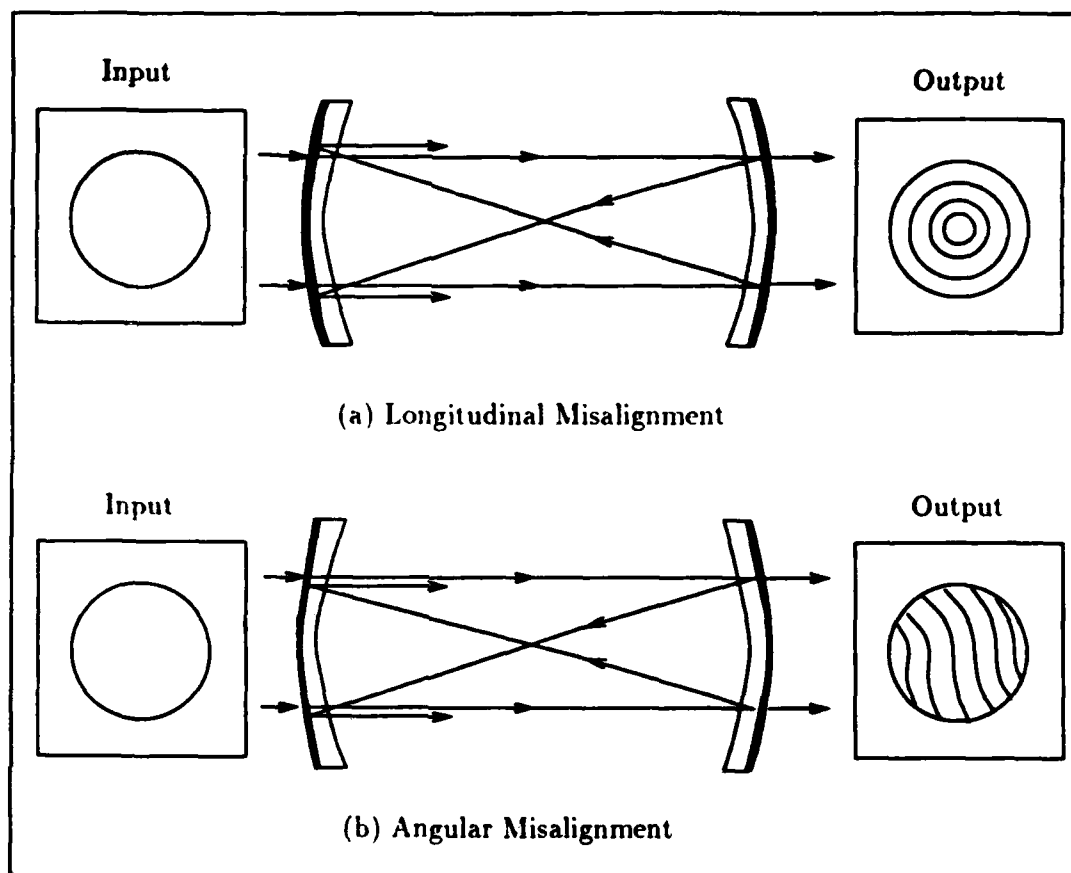
Figure 43. MisAlignment of the Confocal Resonator.

514.5 nm and not the 575 nm wavelength the reflective coatings are specified for. This caused difficulty in originally understanding the fringe pattern of the resonator because the face reflections add a low intensity fringe pattern on top of the two fringe patterns that will be discussed in the following paragraphs (longitudinal alignment and angular alignment fringes).

With the major lessons learned, the alignment of the cavity can now be performed. Two fringe patterns resulting from misalignment of the confocal resonator are shown in Figure 43. In general, the fringe pattern is due to the combined effects of longitudinal and angular misalignment. The fringes are used to determine if the resonator is alignment. The fringe pattern desired is the largest bull's-eye pattern

with the largest angular alignment fringe.

The first step in the alignment procedure is to set up a collimated beam in the resonator. Because of the fact that the resonator mirrors are Mangin mirrors with a slight negative lens embodied in them, the beam coming into the resonator must be slightly converging to compensate for the negative lens–this makes the beam collimated in the resonator. The procedure for creating this beam is to first collimate a laser beam with a collimator and spatial filter combination. It is very important to direct this collimated beam directly into the resonator parallel to the resonator's axis. This is performed first by ensuring the collimated beam is traveling straight down the optic table and that the resonator structure is aligned with the table and the collimated laser beam. At this time, the resonator mirrors should be visually separated by approximately 70 cm. The front mirror of the resonator can now be coursely aligned by ensuring that the back reflection off the front mirror outer surface is centered on the collimating lens (see Figure 44a). Then a lens L1 of focal length greater than 40 cm is used to focus the laser beam in the midplane of the resonator (see Figure 44b). After L1 is in place, a second lens L2 is used to collimate the beam within the resonator (see Figure 44c). The mirror within the resonator is to check for collimation over a longer distance than afforded inside the resonator. Note that the beam leaving the output mirror will be diverging due to the back Mangin mirror.

A bull's-eye pattern should now be seen at the output although the bull's-eye circles may not be connected. This is not important at this time. What is important is maximizing the size of the central portion of the bull's-eye (see Figures 43a and 45). This is accomplished by varying the cavity length under micrometer control. This resonator did not originally have micrometer control of the cavity length, but it was added due to the difficulty of precisely setting the cavity length by hand. The angular alignment of the cavity is now adjusted using the horizontal and vertical adjustments on the back and front mirrors to maximize a second set of fringes due

76

(a) Alignment of Front Mirror

(b) Alignment of Lens, L1

(c) Alignment of Lens, L2
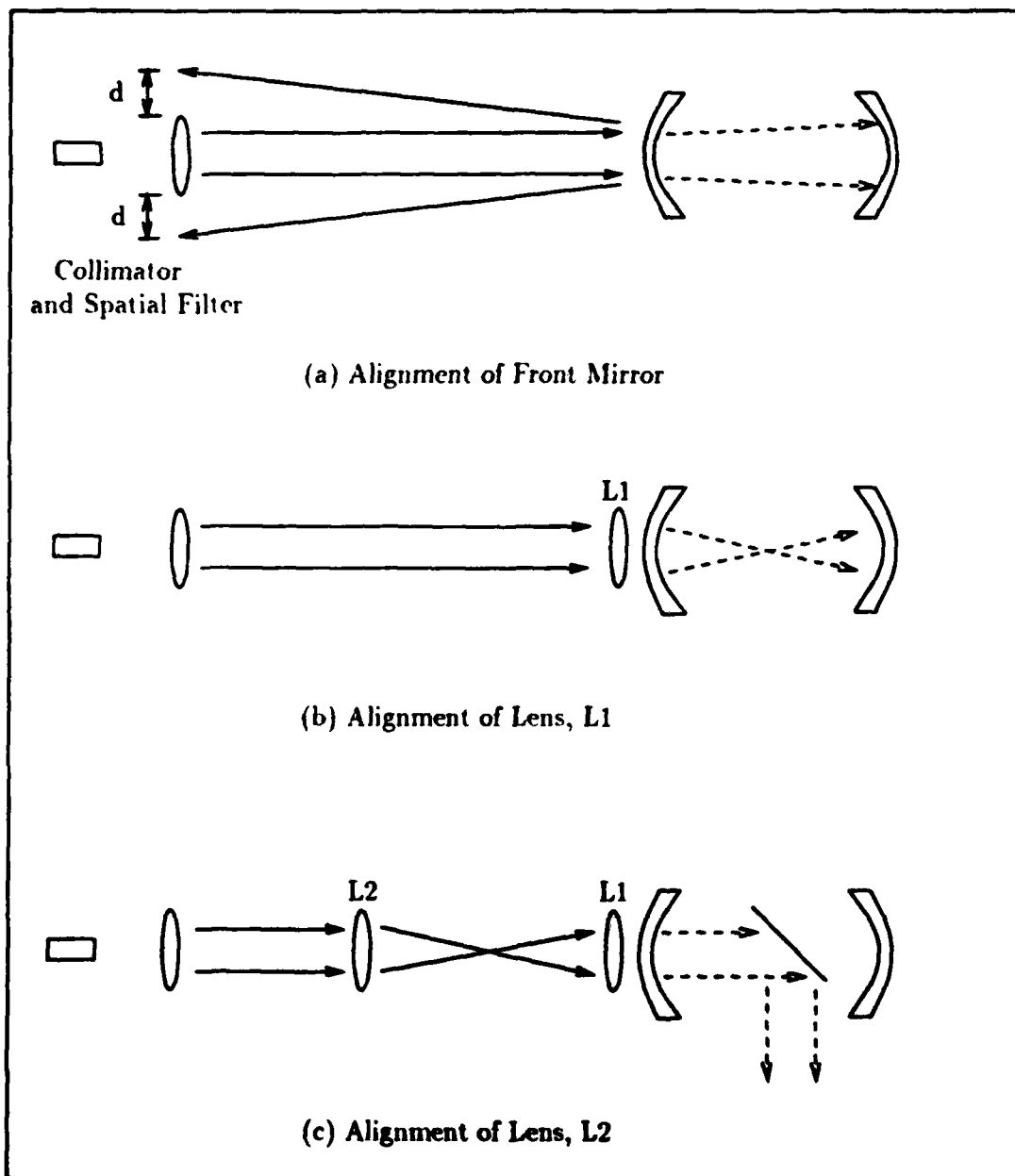
Figure 44. Set up of Collimated Beam for Resonator Alignment.

77
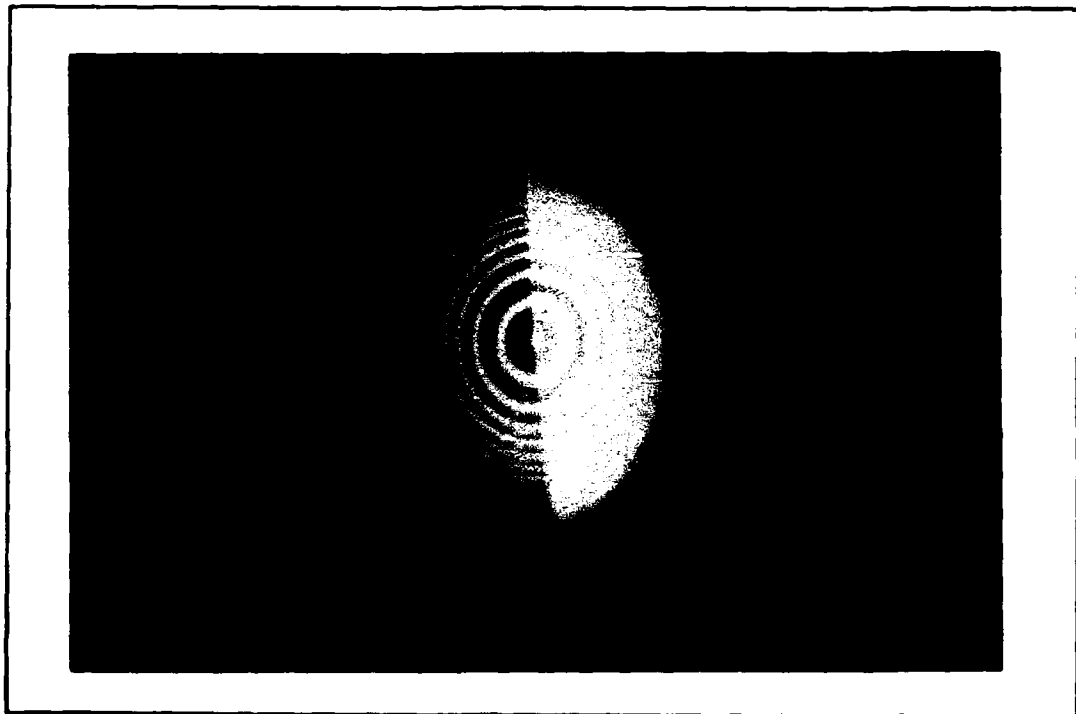
Figure 45.   Bull's-eye Pattern from Longitudinal Misalignment.   Angular misalignment can also be noted in this fringe pattern.
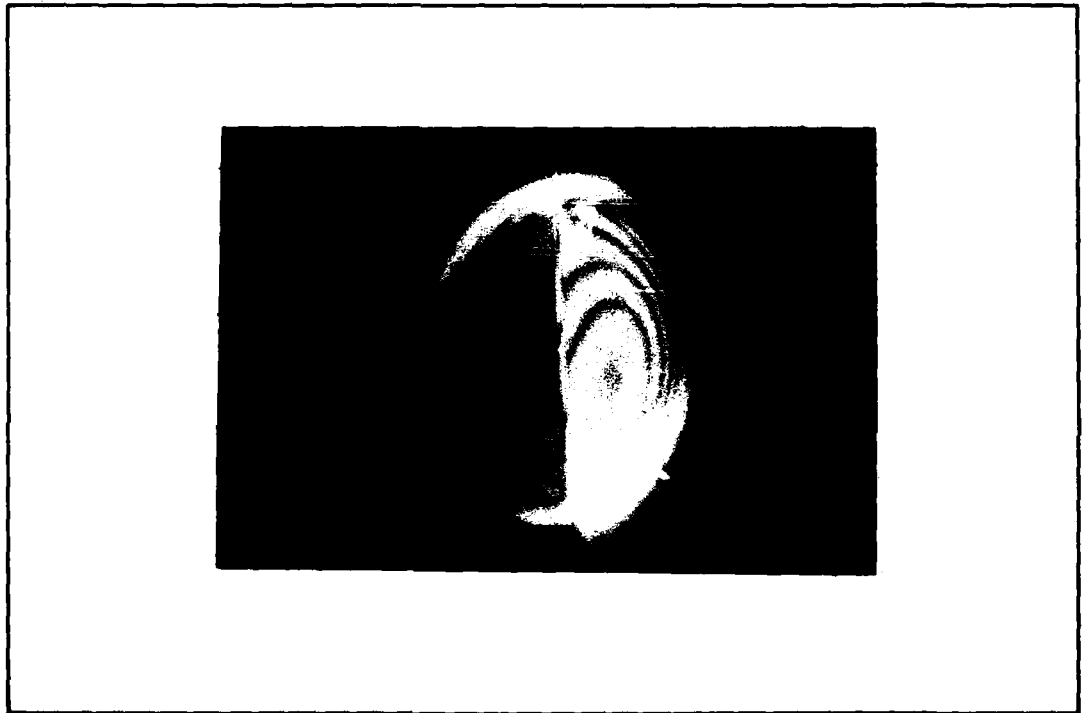
Figure 46. Fringe Pattern from Angular Misalignment.
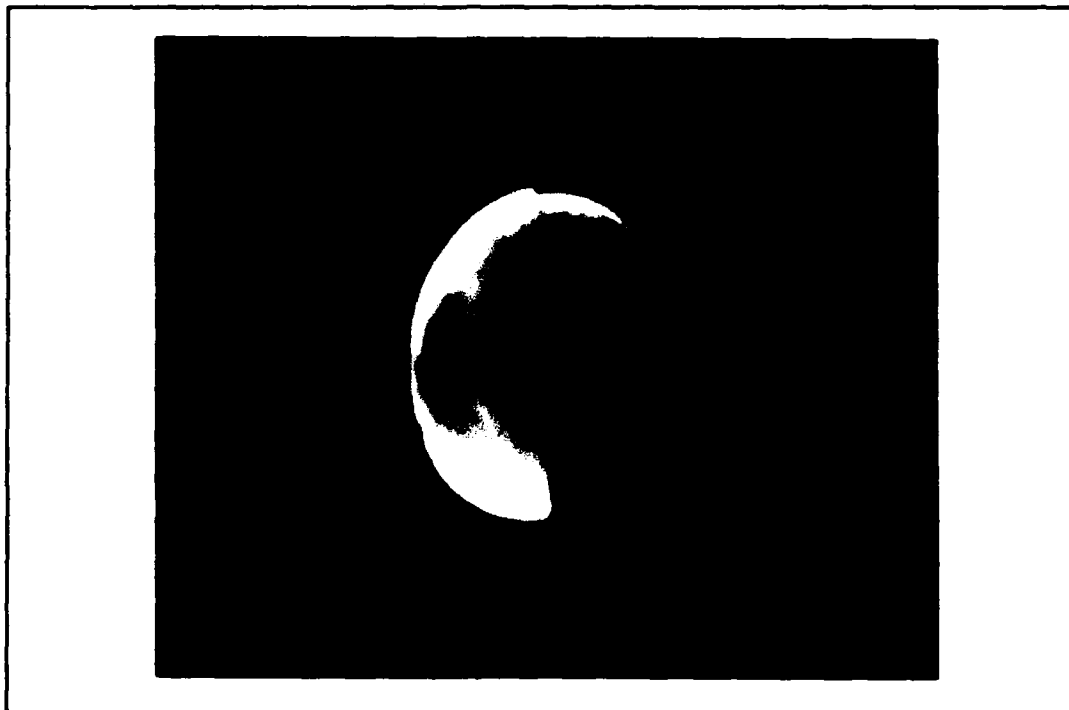
Figure 47.   Fringe Pattern With Optimum Alignment of Confocal Resonator.   Al-
though the resonator is aligned, it can be seen form the small focus spots
resulting from face reflections, that the input beam is not vertically aligned
with the resonator.

to the interference of the inverted beam in the resonator (see Figures 43b, 46, and 47) that will not be present during normal operation of the resonator (see Figure 48). Note that the front mirror should be moved last, because it should be close to optimum alignment due to the alignment step in Figure 44b. An alignment aid with the Mangin mirrors used in this thesis is the fact that the right and left sides of the mirrors have different reflectances with a boundary line between them. This line can be used to achieve horizontal alignment by ensuring the lines from the multiple passes through the resonator overlap as shown in Figure 47. The resonator is now aligned and ready to be used for optical processing.

6.1.2 Testing of the Confocal Resonator Experimental confirmation has been made of the reduction of spherical aberrations by the Mangin mirrors compared to simple spherical mirrors by Lee [10]. The mirror designs used in this thesis are identical to the mirrors used by Lee except the wavelength characteristics of the reflective coatings. Since the only resonator available to AFIT is the Mangin mirror resonator, comparison of the resonator to simple spherical mirror resonators was not directly possible. However, comparisons can be made between the results published by Lee and experimental observations made here.

The experimental setup used to verify the performance of the Mangin mirrors is as shown in Figure 48. In this setup, the imaging characteristics of the resonator are tested by using a USAF resolution target. The resolution target is illuminated with a collimated and spatial filtered beam at plane P1 and is imaged to the midplane of the resonator with lens L1 (unity magnification). The output of the resonator is then imaged onto a CCD camera to determine the resolving ability of the resonator. This is an excellent test because this is exactly the environment that will be used at AFIT in performance of not only this thesis, but follow-on research work. Another test is to bring the plane wave (no input object) into the resonator and illuminate an aperture in the midplane image plane. The size of the aperture can then be varied to determine the area of the beam with constant phase. In this test, the aperture size is
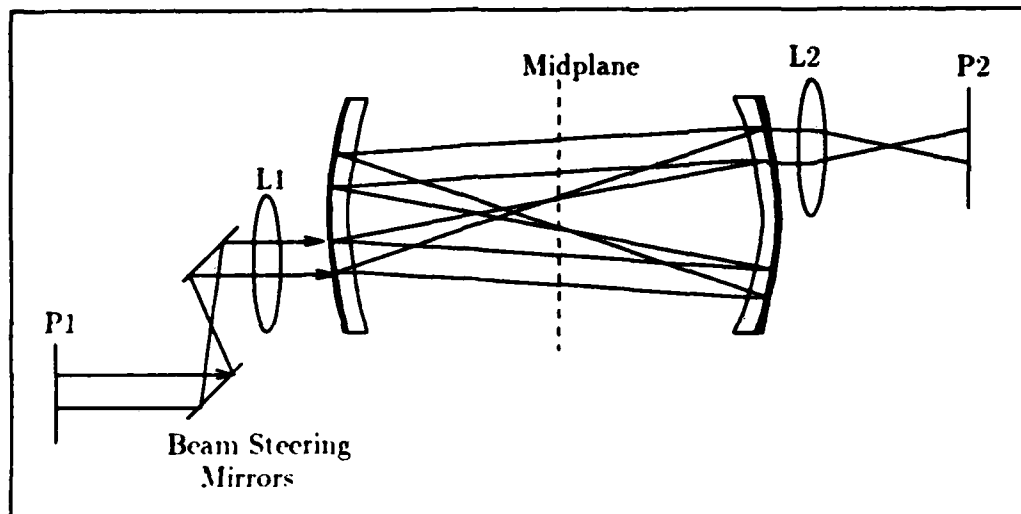
81

Figure 48.   Resolution Testing of the Mangin Mirror Confocal Resonator.   Lens L1 is used to image the resolution chart into the resonator with unity magnification.

increased until a fringe is seen in the output. The area which does not have a fringe in it is a measure of the space-bandwidth product. Once the area of constant phase is known, all processing will be accomplished within this region. The importance of the resolution and the space-bandwidth product is the greater they are, the greater the amount of parallel information processing that can be accomplished accurately in the confocal resonator.

The results of the resolution test were very good considering that two-inch optics were used to bring the image into the resonator and out onto a vidicon camera. In the experiment, the angle of inclination was 12 mrad (same as Lee) to simulate the diffraction of the image off of the hologram at an angle in the hologram. The vertical and horizontal line pairs of the resolution chart could be distinguished down to 57 lines/mm in this test which translates to resolution of lines down to 17.5 μm apart. Lee reported the Mangin mirrors have an experimental resolution limit of 128 lines/mm. To explain why the resolution reported by Lee is not achieved here, a look at diffraction limited optics is required. One figure of merit for image resolution in

a diffraction limited system is the Rayleigh resolution criteria. Using the Rayleigh resolution criteria [$1.22\lambda(distance\ from\ optic)/(diameter\ of\ optic)$], the resolution of the input optic for two point sources is 7.5 μm ($d_o = 60cm$), and the calculated resolution of a Mangin mirror is 6.27 μm or 159 lines/mm (72 mm aperture and distance of 70 cm). The coherent transfer function of the input optic convolved with the Mangin mirrors and the output optics explain why a resolution of 57 lines/mm was obtained. An analysis of this data would give a ballpark figure for the resolution of the resonator. but it would not improve the system resolution any. In fact, the component with the worst resolution of the system is crystal C2 in the Fresnel plane (see Section 5.2.3.4). If artificial phase diffusers are developed at AFIT, a hologram can be placed in the Fourier transform plane and the crystal in the image plane. Thus the crystal would no longer be the limiting system component. At this point, higher $f/\#$ optics would be required to increase the system resolution.

The test for a constant phase used by Lee was modified by using an aperture outside of the mirrors to limit the size of the beam in the resonator rather than using the aperture in the image plane (see Figure 48). The reason this was done was to make the adjustment of the aperture easier and avoid blocking the Fourier transform plane with the apertures outside diameter. The area of constant phase was found to be 36 mm in diameter which is slightly larger than the 33.6 mm. The difference is believed to be because Lee used an input beam at an inclination of 12 mrad, but an inclination of 0 mrad was used here. The inclination of 0 mrad was used because in the optical associative memory, the diffraction off of the holograms will allow the separations of the Fourier transform planes in the midplane of the resonator.

6.2 Summary

Many important lessons have been learned about the alignment and stabilization of the confocal resonator. Now that these lessons have been learned, the resonator can be used to characterize the gain of the nonlinear crystals. The con-

focal resonator itself has been characterized at 575 nm. A wavelength of 514.5 nm can be used within the resonator, but very little feedback would be provided ($\approx$ 10 %). Since AFIT is considering the purchase of another Mangin mirror set, it is recommended that the mirrors are purchased for operation at 514.5 nm since this is a wavelength easily provided by an argon laser, and the $BaTiO_3$ crystals provide more gain at 514.5 nm. In the next chapter, the holographic plates are characterized at low-angles between the reference and object beams to determine the maximum diffraction efficiency that can be expected within the resonator.

VII. Low-Angle Phase Holography

7.1 Introduction

The experiments performed in this section are based upon the work of Fielding [16]. The photographic plates used to perform the low-angle experiments were Kodak 1-A High Resolution plates recorded at 488 nm. These plates and the high resolution plates (Agfa 8E75-HD) for use at 575 nm are well-characterized at large angles (10-30°). However, for use within the confocal resonator, small angles are required (1-3°). Thus, the holographic plates need to be characterized to determine what diffraction efficiency can be expected at the low angles.

7.2 Low-Angle Requirement

The low-angle requirement is driven by two factors. One is the physical size of the Mangin mirrors, and the other is the size of the crystal in the Fourier plane. The Mangin mirrors have a outer diameter of 72 mm but from the last chapter, only have a phase error free diameter of 36 mm which only allows a maximum of 18 mm of deflection by the holograms over 35 cm (3°). The crystal C1 in the Fourier plane limits the angle by the spatial separation of the correlation peaks. Since the crystal is 5 mm wide, a maximum separation that can be used is $\approx$ 4 mm. The angle calculated from the inverse tangent of 4 mm/35 cm is 0.65°. Therefore, the angles must be in a band of 0.65°. The minimum angle which can be used is 1° to allow for separation of crystals C1 and C2. Due to these design constrains, the band of angles to be used will be from 2.2 to 2.8°.

7.3 Recording and Development of Holograms

The process used by Fielding was to record the hologram with ten times the intensity in the reference beam than in the object beam. The reason for ten times the intensity in the reference beam is to provide for a linear recording of the object
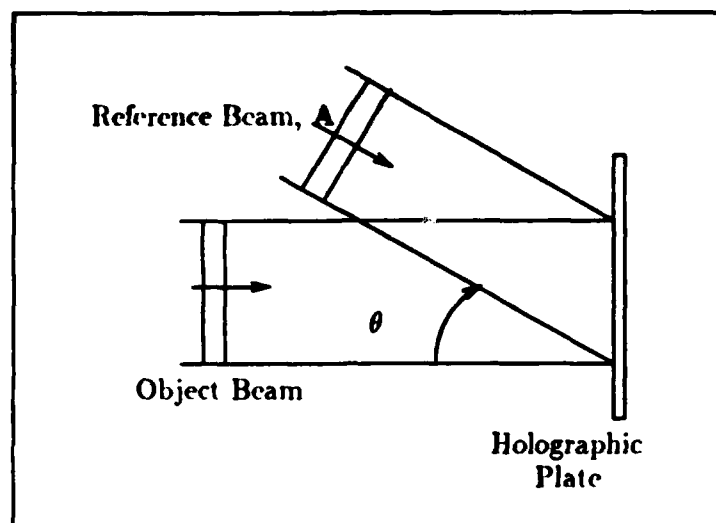
85

Figure 49. Test Configuration Used for Testing of Low-Angle Holograms.

beam on the hologram. Two plane waves were used as the object and reference beams (see Figure 49). The beam intensities selected were 50 $\mu W/cm^2$ in the object beam, and 500 $\mu W/cm^2$ in the reference beam. To find the optimum exposure time for the maximum diffraction efficiency of the phase holograms, a two-step process is used. First, a calculation is performed based on the energy density for 50 % transmission. Fielding had found this energy density to be between 10-15 $\mu J/cm^2$ [16]. From (energy/area) = (power/area) x time, the beginning exposure time is calculated. Using this starting exposure time , the exposure times are increased to find the optimum exposure time for maximum diffraction efficiency.

Fielding has found that the development process has enormous impact on the diffraction efficiency of the holograms. The development process used for making the phase holograms was the one found by Fielding to be the best. This development process consists of five steps:

1. 2 minutes in Kodak D-19 Developer (develops exposed portions of plates)

2. 1 minute rinse

86

3. 1 minute in Kodak Rapid Fixer (removes undeveloped emulsion)

4. 1 minute rinse

5. 8 minute in a bleach solution consisting of: (bleaches remaining silver halide)

   (a) .8 g Potassium Dichromate

   (b) 4.0 g Potassium Bromide

   (c) 1 ml Sulfuric Acid

   (d) Deionized water to 1 litre

7.4 Diffraction Efficiency

The angle, θ, selected for this test was 2.5° because it is in the center of the band. The beam intensities chosen for the diffraction efficiency test were 50 $\mu W/cm^2$ in the object beam, and 500 $\mu W/cm^2$ in the reference beam. The starting exposure time is calculated as 30 ms.

$$15 \; \mu J/cm^2 = 550 \mu W/cm^2 \times time \tag{36}$$

The exposure times are then increased to find the optimum exposure time for maximum diffraction efficiency. The diffraction efficiency received for each exposure time is plotted in Figure 50. As seen from this plot, the maximum diffraction efficiency is at an exposure time of 150 ms for a resulting 12 % diffraction efficiency. A picture of the diffraction pattern of the 150 ms exposure hologram is shown in Figure 51. With this hologram, six diffracted orders were seen on each side of the zeroth order. They are not pictured due to the thresholding of the photographic film.

7.5 Summary

The remaining question pertaining to the question of phase holography is whether or not 10 % (Used as a conservative measure) is enough for the associative memory to resonate to a solution. The answer to this question is yes if one
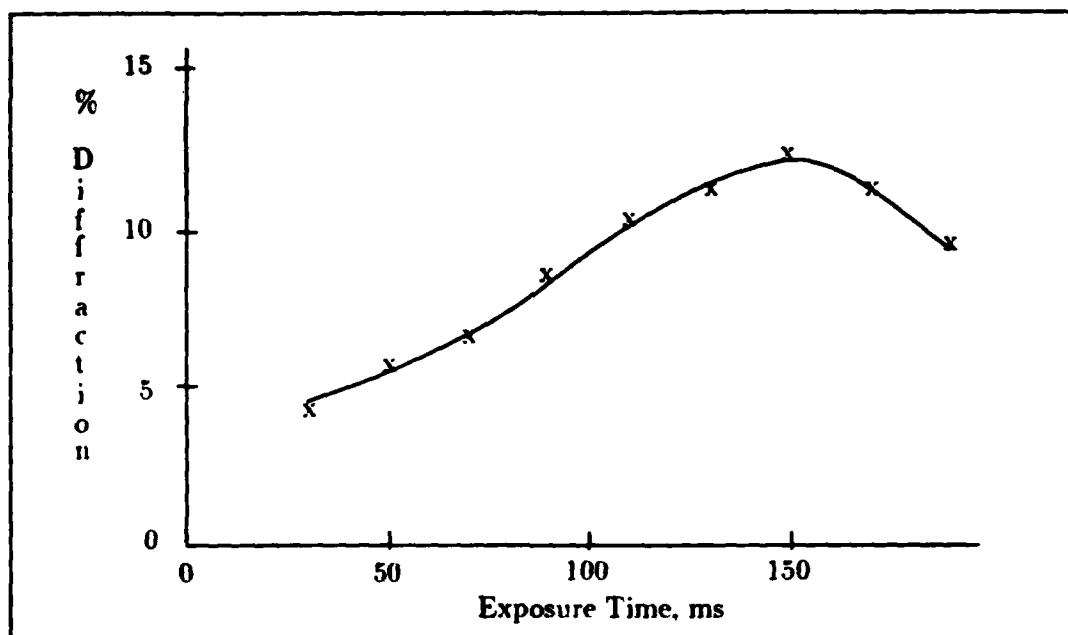
Figure 50. Diffraction Efficiency versus Exposure Time.

object is stored (Gain of 300); however, if two objects are stored the answer is no (Gain of 600). The gain required contained in parenthesis are arrived at by taking into consideration the losses of the mirrors, diffraction efficiency of two holographic plates, and losses going into the $BaTiO_3$ crystals. The nonlinear attenuation crystal, C1, could be turned around for additional gain which would result in a configuration similar to Northrop's design [27]. Before this is attempted, however, more experiments to maximize the gain of the 45°-cut crystal within the resonator should be conducted.

Figure 51.   Diffraction Pattern of a Thin Hologram.   The zeroth order is the largest spot in the center, and the diffracted orders are symmetric about the zeroth order.

VIII. CONCLUSIONS AND RECOMMENDATIONS

8.1 Conclusions

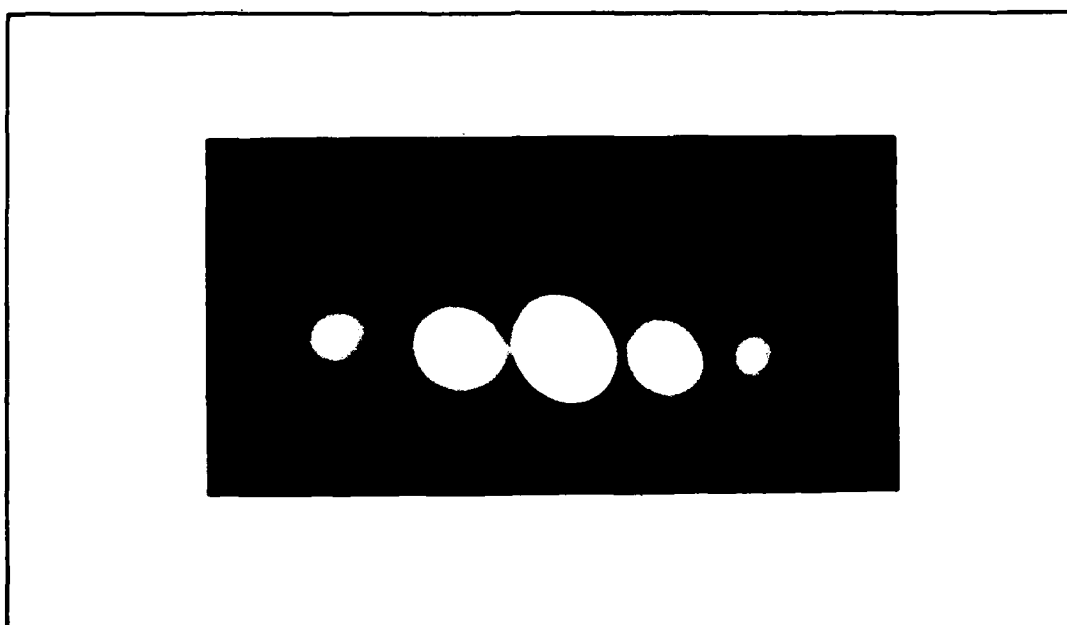Four major contributions of this thesis are in resonator architecture design, characterization of the $BaTiO_3$ crystals, resonator alignment and stabilization, and characterization of holographic plates for low-angle holography. All of these areas were directed to building of the capability to perform optical regenerative algorithms at AFIT. This thesis was very successful in laying the foundation for development of optical regenerative algorithms within the confocal resonator and their implementation. Each of the contributions of the thesis will now be discussed, followed by recommendations for continued research.

The confocal resonator offers a unique processing environment with two image and two Fourier transform planes, but with that environment comes unique challenges to the optical associative memory design. This challenge comes from the the need for holographic memory elements in a resonator which wants the beams to follow a single on-axis path through the resonator in order for the beams to recombine. The optical associative memory design developed in Chapter 3 is able to account for this on-axis design condition and uses it to the advantage of the design. Another important characteristic of this design is the use of a nonlinear attenuator in the feedback path. This attenuator allows for a gain-loss competition within the resonator for convergence to the problem solution. While this architecture was not implemented in this thesis, it will be implemented in follow-on research at AFIT which will use the design architecture in Chapter 3.

Optical processing functions necessary for implementation of optical regenerative algorithms have been demonstrated with $BaTiO_3$. The most basic requirement for these regenerative algorithms is a gain mechanism to recover losses within the feedback path. With both the z-cut and 45°-cut crystals, the necessary gain for

processing applications has been demonstrated. The gain with the z-cut crystal was steady-state both inside and outside the resonator. However, with the 45°-cut crystal, a time-dependent gain was noted outside of a resonator and a steady-state gain was noted inside the resonator. The time-dependent gain is caused by the large amount of beam-fanning within the 45°-cut crystal. Within the resonator, however, the beam-fanning aids the development of the resonator beam by providing a large initial energy to initiate the lasing and large electro-optic coefficients to maintain the lasing process. Within the resonator the 45°-cut crystal has shown a greater ability to compensate for cavity losses, suggesting improved gain performance of the 45°-cut crystal over the z-cut crystal. Other important processing abilities demonstrated with $BaTiO_3$ include image amplification, edge enhancement, nonlinear attenuation, and nonlinear amplification.

Many lessons were learned about the alignment and stabilization of a large optical resonator. The primary lessons learned were the sensitivity of the resonator to vibrations and air currents. The resonator had to have rigidly interconnected supports and the cavity isolated from air currents before stabilization was achieved. A complicating factor in the stabilization was the improperly anti-reflection coated inner surfaces of the resonator, which were coated for 514.5 nm rather than matching the 575 nm of the outer reflective surfaces. The reflections off of the front surfaces added an extra set of fringes at the resonator output. The resonator was still able to be stabilized with these face reflections.

The holographic plates were characterized for maximum diffraction efficiency with low-angles between the reference and object beams (1-3°). The maximum diffraction efficiency for the holographic plate at an angle of 2° was 12 %. For the gains demonstrated thus far, this diffraction efficiency is enough for the storage of one object within the holographic memory. However, with improvements in the gain by characterization of the $BaTiO_3$ crystal within the resonator, object storage greater than 3 should be theoretically possible from the work by Lee [11].

8.2 Recommendations

The following are recommendations for continued research on optical regenerate algorithms within the confocal resonator:

1. Characterization of both the z-cut crystal and the 45°-cut crystal within the confocal resonator;

2. Mathematical modeling of the combination of beam-fanning and two-wave coupling within $BaTiO_3$;

3. Implementation of the processing architectures contained in Chapter 3 and Appendix C;

4. Procurement on a confocal resonator with reflective and anti-reflective coatings at 514.5 nm, since this is the optimum frequency for gain in $BaTiO_3$;

5. Research on Lithium Niobate crystals for improved diffraction efficiency at low angles and volume storage of holograms; and,

6. Research on artificial phase diffusers for the storage of Fourier transform holograms within the confocal resonator.

Appendix A. *TWO-WAVE COUPLING TEST PLAN*

The experimental measurements made of the two-wave coupling in $BaTiO_3$ will be taken in accordance with the following test plan (see Figure 52). This test plan includes procedures that would not normally be included in a two-wave coupling experiment in order to investigate an abnormal effect that we have noted within our particular $BaTiO_3$ crystal which is cut along the (100), (011) and (01$\bar{1}$) crystallographic planes. The abnormal effect is an amplification of the probe beam when both beams are incident on the crystal followed by a deamplification of the probe beam below its original value. The energy lost in the probe beam appears to be going in the direction of the output pump beam. The two-wave coupling test plan is:

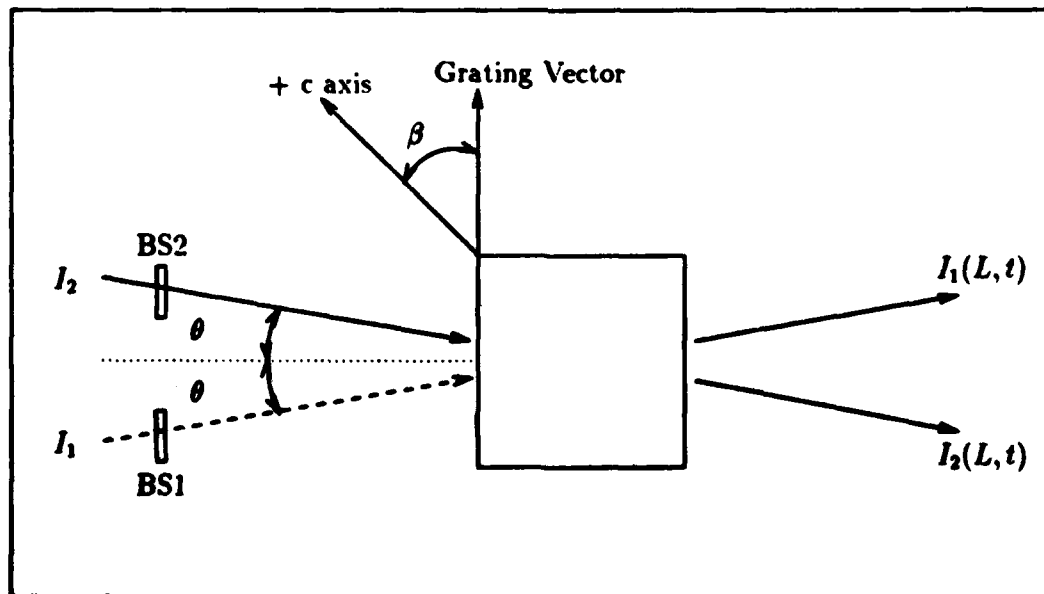1. Measure the intensities of the pump, I_2, and the probe, I_1, beams.

Figure 52. Two-Wave Coupling Test Configuration

93

2. Measure the degree of polarization and the polarization orientations of the input beams. The polarization desired is extraordinary.

3. Measure the angle, 2θ, between I_2 and I_1 and measure the angle, β, of the grating vector with respect to the +c-axis of the crystal.

4. Erase all gratings formed.

5. Input both the probe and pump beams and measure the time response of the output beams $I_1(L,t)$ and $I_2(L,t)$.

6. Measure the outputs of beam splitters, BS1 and BS2, to determine if there is any phase conjugation of the probe and pump beams.

7. Repeat the above procedure for different input beam intensities.

8. Repeat the above procedure for different angles, β, between the grating vector and the +c-axis.

9. Repeat the above procedure for different angles, 2θ, between the pump and probe beams.

Appendix B. *SELF-PUMPED PHASE CONJUGATION: 45°-CUT CRYSTAL*

Due to the excellent references available for self-pumped phase conjugation. only the experimental results will be published here. A good reference for the theory behind self-pumped phase conjugation is reference [14] [16]. The experimental setup for self-pumped phase conjugation is shown in Figure 53. The angle of interest here is the external angle, α, between the normal to the crystal face and the input beam.

Two experiments were performed with the 45°-cut crystal. The first was to find the maximum reflectivity and the second was to find the image resolution. In
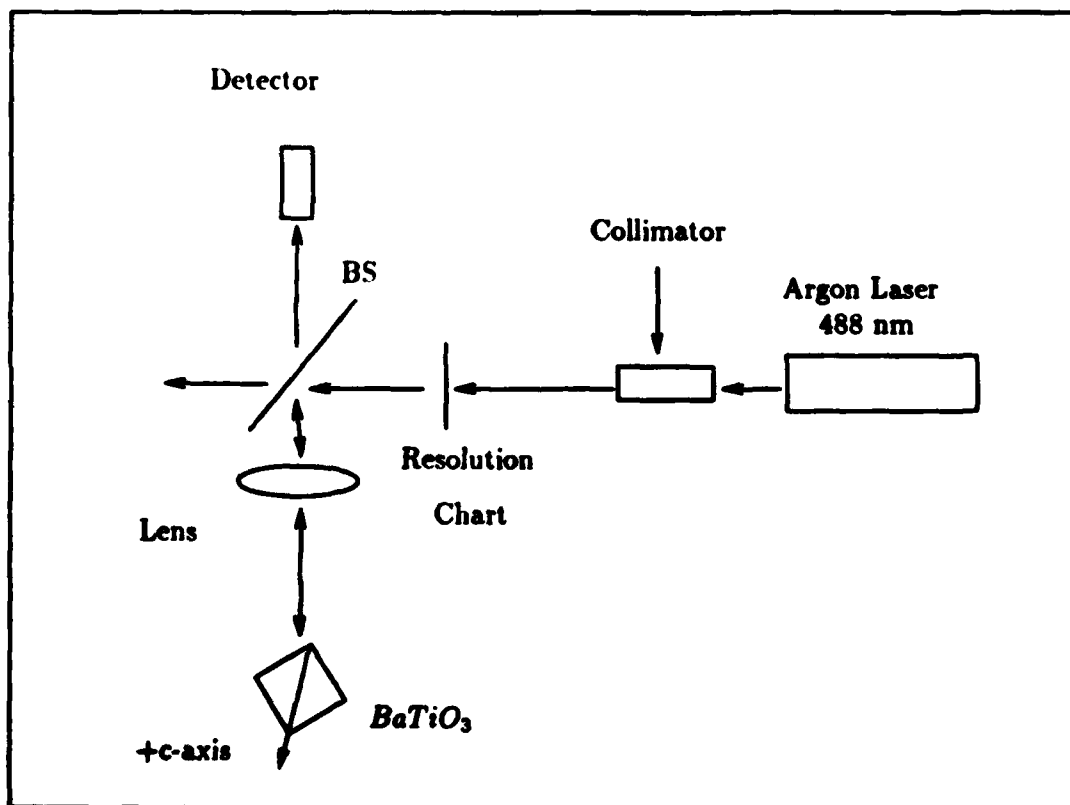

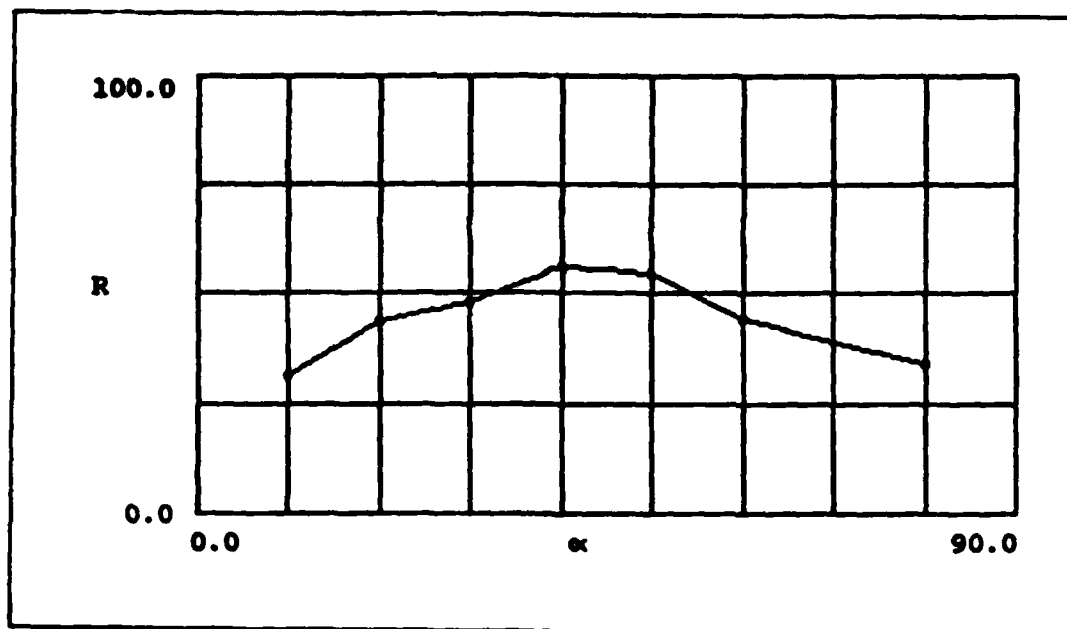**Figure 53. Experimental Setup for Phase Conjugate Reflectivity**

Figure 54. Phase Conjugate Reflectivity versus External Input Angle

these experiments, there was 5 mW total power in a 1 mm diameter beam incident on the crystal.

For the maximum reflectivity test, the USAF resolution chart was not present. The angle, α, was varied from 10 to 80°. The maximum reflectivity was found at $\alpha = 40°$ and was 56 %. This compares with 38.5 % found by Fielding for the z-cut crystal [16]. For the image resolution test, a USAF resolution chart was placed a focal length away from the lens and the crystal was set at $\alpha = 40°$. In this experiment, resolution down to 16 lines/mm (group 4 (1)) for the vertical bars and 11 lines/mm (group 3 (4)) (see Figure 55). The resolution difference was also noted by Fielding, and the cause is not known. This test was redone for the resolution chart tilted at 45° with resolution down to 16 lines/mm for both line pairs (see Figure 56). Calculations were performed to see if the limit related to the crystal or the setup and it was determined that the setup was the cutoff due to the spatial filtering of the crystal's dimensions.

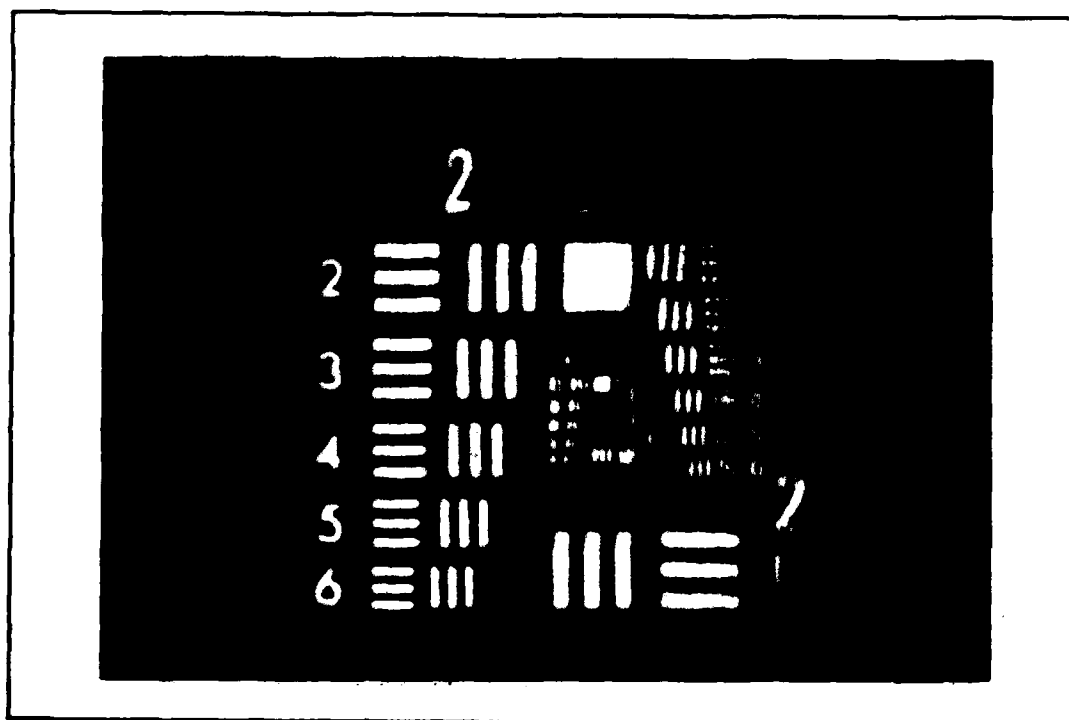Figure 55. Image Resolution of Phase Conjugation with USAF Resolution Chart. Note that the vertical and horizontal bars have different resolution.
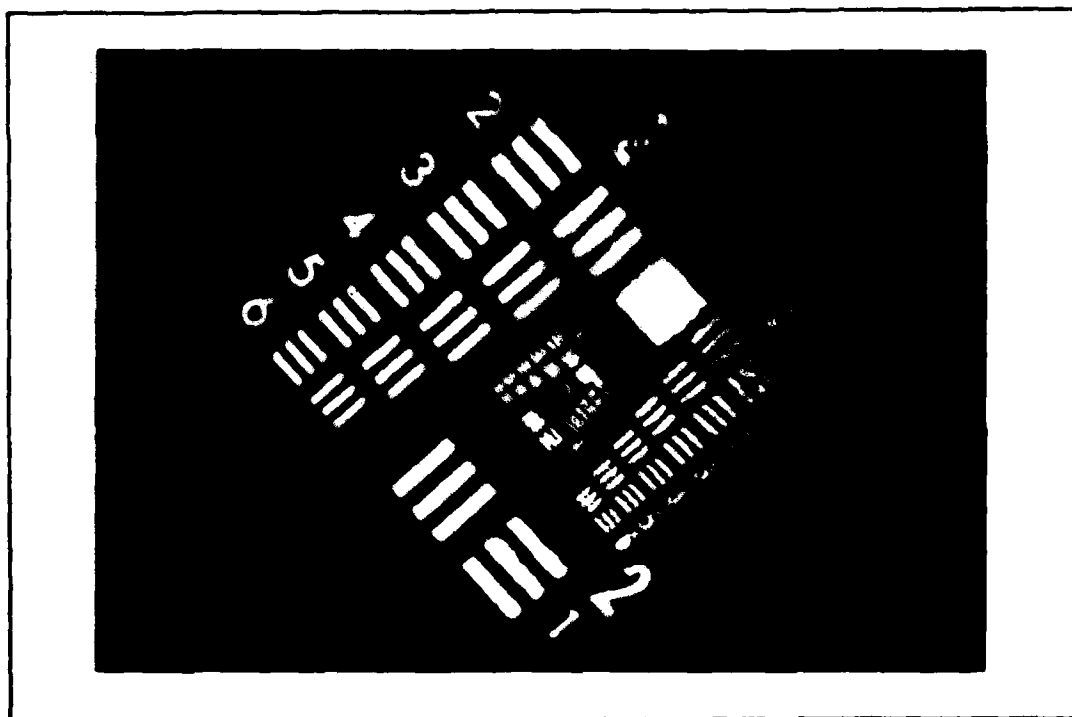
Figure 56. Image Resolution with the Chart Tilted at 45°. Note that the horizontal and vertical bars have the same resolution.

Therefore, the 45°-cut crystal yields improved percent reflectivity and has been shown to have resolution at least as good as 16 lines/mm.

Appendix C. *AMPLITUDE STRIPPING OF AN AMPLITUDE AND PHASE VARYING SIGNAL*

Many algorithms require that only the amplitude or phase of a signal be passed on within the algorithm. Two such algorithms are the Fienup phase retrieval algorithm and the Kobel-Martin pattern recognition algorithm which requires the amplitude only and the phase only portions of the signal.

Passing only the amplitude variations without the phase information has been demonstrated by Peri [30]. Peri used the process of two-wave coupling in $BaTiO_3$ to pass the amplitude variations of the pump beam onto the probe beam without passing the phase of the pump beam (see Figure 57). However, a system for passing
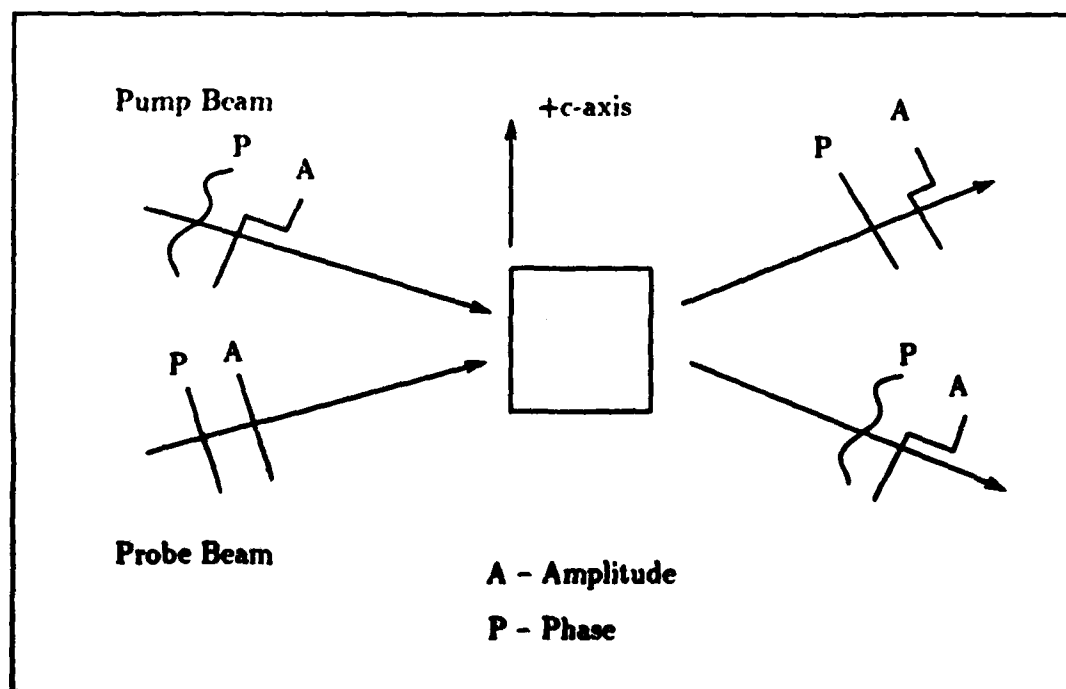

Figure 57. Coherent Energy Transfer in Two-Wave Coupling. The amplitude variations of the pump beam is transferred to the probe beam [30].
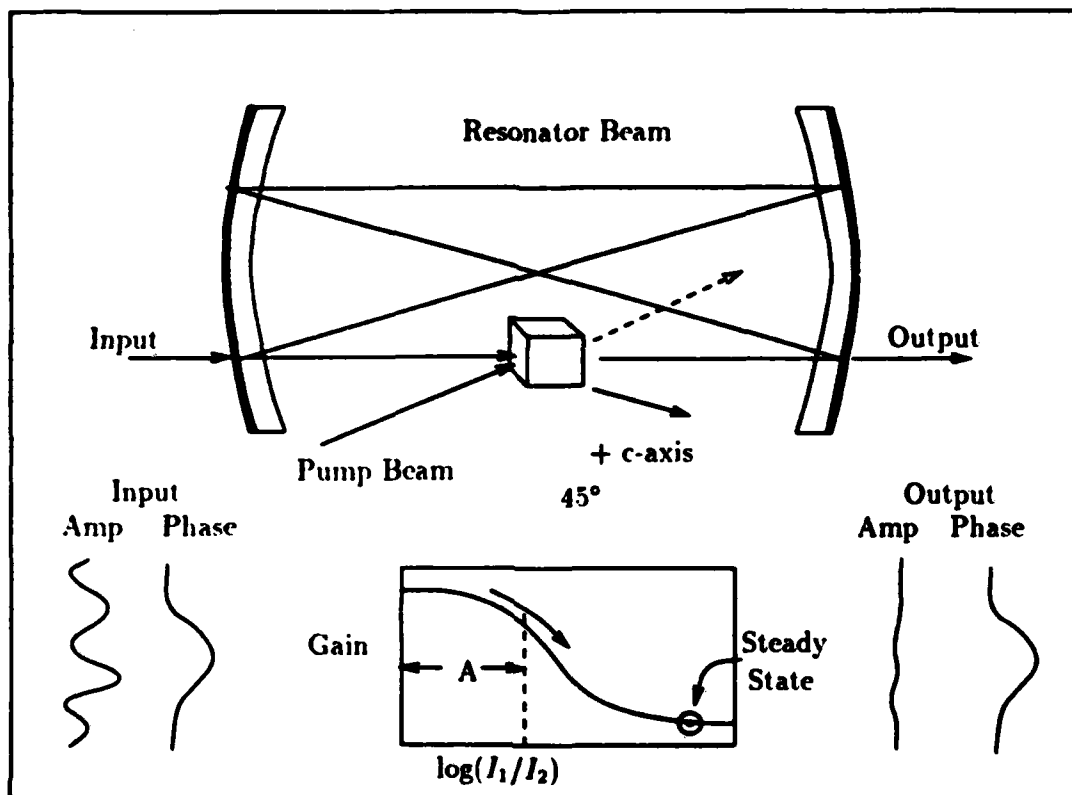
Figure 58. Amplitude Stripping of an Amplitude and Phase Varying Signal. The $BaTiO_3$ crystal operates as a saturable gain media to lessen amplitude variations.

the phase only has not been proposed. A method of passing only the phase information is to use the saturable gain characteristics of the $BaTiO_3$ crystals (Sections 4.3.3 and 5.2.4.3) and optical feedback. Using the saturable gain curve shown in this thesis and reproduced here (see Figure 37), the input may be limited to region A of the $log(I_1/I_2)$ axis. As the resonator and crystal lase on the input beam, the operating region of the crystal walks down the gain curve until it reaches the point where the gains equal loses with the result being a more uniform amplitude output with the original phase information. Thus, the amplitude variations have been stripped, while the phase information is passed on.
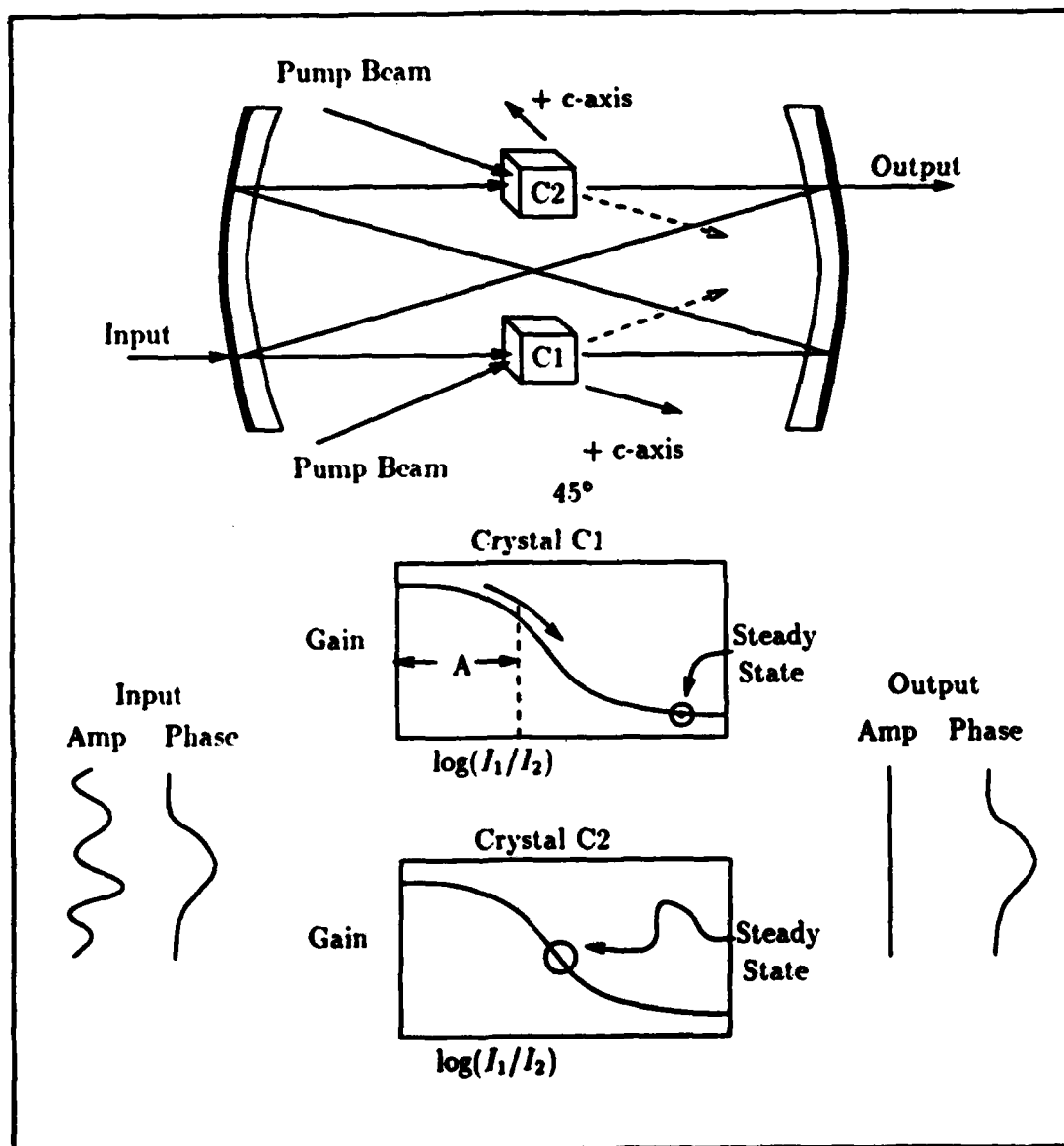
Figure 59. Improved Amplitude Stripping Schematic. Crystal C1 operates as a saturable gain media as in the previous schematic, and crystal C2 also operates as a saturable gain media to clean up the final amplitude variations. Note that crystal C1 has bottomed out on its curve, while C2 is still in the middle of its nonlinearity in the steady-state condition.

If the uniformity of the output beam is not enough for the algorithm, then another crystal could be placed in the feedback loop also operating as a saturable gain media to level out the amplitude of the output beam (see Figures 35 and 59). In order to perform this function, the biasing of the two crystals should be such that crystal C2 is still in the middle of its nonlinearity while crystal C1 has bottomed out on the curve as shown in Figure 59. Thus, the crystals operate in a cooperative mode for a steady-state solution of a uniform amplitude output with the input phase variations.

Bibliography

1. Akins, Robert and Sing Lee. "Coherent Optical Image Amplification by an Injection-Locked Dye Amplifier at 632.8 nm," *Applied Physics Letters, 35:* 660-662 (1 November 1979).

2. Akins, R. and S. Lee. "Transient Response and Time Evolution of 2-D Solutions in a Coherent Optical Processor with Feedback," *Applied Optics, 21:* 4515-4520 (15 December 1982).

3. Akins, Robert P. and Sing H. Lee. "Two-Stage Injection-Locked Ring Dye Laser/Amplifier for Coherent Image Amplification." *Journal of the Optical Society of America A, 1:* 533-536 (May 1984).

4. Anderson, Dana Z. "Coherent Optical Eigenstate Memory," *Optics Letters, 11:* 56-58 (January 1986).

5. Anderson, Dana Z. and R. Saxena. "Theory of Multimode Operation of a Unidirectional Ring Oscillator having Photorefractive Gain: Weak Field Limit," *Journal of the Optical Society of America B, 4:* 164-176 (February 1987).

6. Bledowski, Alekander and Wieslaw Krolikowski. "Exact Solution of Degenerate Four-Wave Mixing in Photorefractive Media," *Optics Letters, 13:* 146-148 (February 1988).

7. Cedarquist, Jack and Sing Lee. "Coherent Optical Feedback for the Analog Solution of Partial Differential Equations." *Journal of the Optical Society of America, 70:* 944-953 (August 1980).

8. Cedarquist, Jack and Sing Lee. "Confocal Feedback Systems with Space Variance, Time Sampling, and Secondary Feedback Loops," *Journal of Optical Society of America, 71:* 643-650 (June 1981).

9. Cronin-Golomb, Mark. *et al.* "Photorefractive Time Differentiation of Coherent Optical Images," *Optics Letters, 12:* 1029-1031 (December 1987).

10. Fainman, Y. and S. Lee. "Experimental Evaluation of Mangin Mirror Performance for Optical Processing with Feedback," *Optical Engineering, 24:* 535-540 (May/June 1985).

11. Fainman, Y. *et al.* "Optimal Coherent Image Amplification by Two-Wave Coupling in Photorefractive Barium Titanate," *Optical Engineering, 25:* 228-234 (February 1986).

12. Feinberg, Jack. *et al.* "Photorefractive Effects and Light-Induced Charge Migration in Barium Titanate," *Journal of Applied Physics, 51:* 1297-1305 (3 March 1980).

13. Feinberg, Jack. *et al.* "Erratum: Photorefractive Effects and Light-Induced Charge Migration in Barium Titanate," *Journal of Applied Physics, 52:* 537 (January 1981).

14. Feinberg, Jack. *et al.* "Self-Pumped, Continuous-Wave Phase Conjugator Using Internal Reflection," *Optics Letters*, 7: 486-488 (October 1982).

15. Feinburg, Jack. "Asymmetric Self-Defocusing of an Optical Beam from the Photorefractive Effect," *Journal of the Optical Society of America*, 72: 46-50 (January 1982).

16. Fielding, Kenneth H. *A Position, Scale, and Rotation Invariant Holographic Associative Memory*. MS Thesis, AFIT/GEO/ENG/88D-2. School of Engineering, Air Force Institute of Technology (AU), Wright-Patterson AFB, OH, December 1988. (DTIC number not available at this time).

17. Fienup, J. R. "Phase Retrieval Algorithms: A Comparison," *Applied Optics*, 21: 2758-2769 (1 August 1982).

18. Goodman, Joseph W. *Introduction to Fourier Optics*. San Francisco: McGraw-Hill Book Co., 1968.

19. Gunter, P. "Holography, Coherent Light Amplification and Optical Phase Conjugation with Photorefractive Materials," *Physics Reports (Review Section of Physics Letters)*, 93, No. 4: 199-299 (1982).

20. Johnston, Steve and Sing Lee. "Confocal Optical Feedback Processing System: an Improved Design," *Applied Optics*, 22: 1431-1438 (15 May 1983).

21. Klein, M. B. and George C. Valley. "Beam Coupling in Barium Titanate at 442nm," *Journal of Applied Physics*, 57: 4901-4905 (15 June 1985).

22. Klein, M. B. *et al. Degenerate Four-Wave Mixing Smart Detector: Final Report.* September 1986. Contract MDA 904-83-C-0463. Fort George Meade MD: Maryland Procurement Office, February 1983.

23. Klein, M.B. *et al.* "Imaging Threshold Detector Using a Phase-Conjugate Resonator in Barium Titanate," *Optics Letters*, 11: 575-577 (September 1986).

24. Lee, Sing H. "Optical Information Processing," *Topics in Applied Science*, Volume 48, edited by Sing H. Lee. Berlin: Springer-Verlag, 1981.

25. Motes, Andy and Jin Joong Kim. "Beam Coupling in Photorefractive Barium Titanate Crystals," *Optics Letters*, 12: 199-201 (March 1987).

26. Motes, Andy. *et al.* "Temporal Behavior of the Intensity-Dependent Absorption in Photorefractive Barium Titanate," *Optics Letters*, 13: 509-511 (June 1988).

27. Stoll, H. M. and L-S. Lee. "A Continuous-Time Optical Neural Network," *Proceedings of the IEEE International Conference on Neural Networks, 2:* 373-384 (July 1988).

28. *Optical Implementation of Phase Retrieval.* Contract Proposal PLX87-019 to the Air Force Weapons Laboratory. Sparta, Inc., Laguna Hills CA, 14 May 1987.

29. Pepper. David M. "Hybrid Phase Conjugator/Modulators using Self-Pumped O°-Cut and 45°-Cut Barium Titanate Crystals," *Applied Physics Letters, 49*: 1001-1003 (20 October 1986).

30. Peri, David. "Optical Implementation of a Phase Retrieval Algorithm," *Applied Optics, 26*: 1782-1785 (1 May 1987).

31. Rajbenbach. Henri. *et al.* "Optical Implementation of an Iterative Algorithm for Matrix Inversion," *Applied Optics, 26*: 1024-1031 (15 March 1987).

32. Sanders Associates, Inc. *Barium Titanate Crystals.* Nashua NH, undated.

33. Saxena. R. and D. Z. Anderson. "Effects of an Applied Field on the Steady State Characteristics of a Unidirectional Photorefractive Ring Oscillator," *Optics Communications, 66*: 172-178 (15 April 1988).

34. Schunemann. P. G. *et al. The Effects of Feed Material and Annealing Atmosphere on the Properties of Photorefractive Barium Titanate Crystals.* Sanders Associates. Merrimack NH, undated.

35. Smiri. Authur L. *et al.* "Picosecond Photorefractive Effect in Barium Titanate," *Optics Letters, 12*: 501-503 (July 1987).

36. Sternklar. Shimon W. and Baruch Fischer. "Controlling the Self-Frequency Shift and Intensity of Oscillations with Photorefractive Crystals," *Applied Optics, 24*: 3121-3122 (1 October 1985).

37. Strohkendl, F. P. *et al.* "Hole-Electron Competition in Photorefractive Gratings." *Optics Letters. 11*: 312-314 (May 1986).

38. Valley. George C. and Marvin B. Klein. "Optimal Properties of Photorefractive Materials for Optical Data Processing," *Optical Engineering, 22*: 704-711 (November 1983).

39. Valley, George C. and Gilmore J. Dunning. "Observation of Optical Chaos in a Phase-Conjugate Resonator," *Optics Letters, 9*: 513-515 (November 1984).

40. Valley, George C, "Simultaneous Electron/Hole Transport in Photorefractive Materials," *Journal of Applied Physics, 59*: 3363-3366 (15 May 1986).

41. Valley, George C. "Competition between Forward- and Backward-Stimulated Photorefractrive Scattering in Barium Titanate," *Journal of the Optical Society of America B, 4*: 14-19 (January 1987).

42. Yariv, Ammon and Pochi Yeh. *Optical Waves in Crystals.* New York: John Wiley and Sons, 1984.

Vita

Captain Jeffery A. Wilson ███████████████████████████████████ ██████████████████████████████ **in 1960** ████ **attended** the United States Air Force Academy, from which he received the degree of Bachelor of Science in Electrical Engineering in May 1984. Upon graduation, he received a commission in the USAF and was assigned to the Air Force Logistics Command at Kelly AFB, TX. At Kelly AFB, Capt. Wilson served as a System Engineer for Air Force Automatic Test Systems. He entered the Electro-Optics Masters Program in the School of Engineering, Air Force Institute of Technology, in June 1987.

REPORT DOCUMENTATION PAGE

Form Approved
OMB No. 0704-0188

1a. REPORT SECURITY CLASSIFICATION	1b. RESTRICTIVE MARKINGS
UNCLASSIFIED	

2a. SECURITY CLASSIFICATION AUTHORITY	3. DISTRIBUTION/AVAILABILITY OF REPORT
	Approved for public release;
2b. DECLASSIFICATION/DOWNGRADING SCHEDULE	distribution unlimited

4. PERFORMING ORGANIZATION REPORT NUMBER(S)	5. MONITORING ORGANIZATION REPORT NUMBER(S)
AFIT/GEO/ENG/88D-5	

6a. NAME OF PERFORMING ORGANIZATION	6b. OFFICE SYMBOL (If applicable)	7a. NAME OF MONITORING ORGANIZATION
School of Engineering	AFIT/ENG	

6c. ADDRESS (City, State, and ZIP Code)	7b. ADDRESS (City, State, and ZIP Code)
Air Force Institute of Technology Wright-Patterson AFB OH 45433-6583	

8a. NAME OF FUNDING/SPONSORING ORGANIZATION	8b. OFFICE SYMBOL (If applicable)	9. PROCUREMENT INSTRUMENT IDENTIFICATION NUMBER
Rome Air Development Center	RADC/COTC	

8c. ADDRESS (City, State, and ZIP Code)	10. SOURCE OF FUNDING NUMBERS			
Griffiss AFB, NY 13411	PROGRAM ELEMENT NO.	PROJECT NO.	TASK NO.	WORK UNIT ACCESSION NO.

11. TITLE (Include Security Classification)

Optical Information Processing in a Confocal Fabry-Perot Resonator

12. PERSONAL AUTHOR(S)
Jeffery A. Wilson, B.S.E.E., Capt, USAF

13a. TYPE OF REPORT	13b. TIME COVERED	14. DATE OF REPORT (Year, Month, Day)	15. PAGE COUNT
MS thesis	FROM _____ TO _____	1988 December	119

16. SUPPLEMENTARY NOTATION

17. COSATI CODES			18. SUBJECT TERMS (Continue on reverse if necessary and identify by block number)
FIELD	GROUP	SUB-GROUP	Optical Processing Barium Titanate
20	06		Optical Interferometers
01	02		

19. ABSTRACT (Continue on reverse if necessary and identify by block number)

Thesis Advisor: Steven K. Rogers, Capt, USAF
Associate Professor of Electricial Engineering

Approved for release in Accordance with AFR 190-1

12 Jan 1989

20. DISTRIBUTION/AVAILABILITY OF ABSTRACT	21. ABSTRACT SECURITY CLASSIFICATION
☐ UNCLASSIFIED/UNLIMITED ☒ SAME AS RPT. ☐ DTIC USERS	UNCLASSIFIED

22a. NAME OF RESPONSIBLE INDIVIDUAL	22b. TELEPHONE (Include Area Code)	22c. OFFICE SYMBOL
Steven K. Rogers, Capt, USAF	(513) 255-6027	AFIT/ENG

DD Form 1473, JUN 86   *Previous editions are obsolete.*   SECURITY CLASSIFICATION OF THIS PAGE

Abstract

Many optical information processing algorithms require feedback to perform iterative processing. An algorithm which exemplifies the requirement for feedback is the optical associative memory. This thesis explores the theoretical design of an optical associative memory in a confocal Fabry-Perot resonator.

The components of the optical associative memory — $BaTiO_3$ crystals, confocal resonator, and holographic plates — are characterized individually to determine the feasibility of implementing the associative memory. The $BaTiO_3$ crystals are characterized for processing functions such as image amplification, edge enhancement, linear and nonlinear gain, and linear and nonlinear attenuation. Unique 45°-cut $BaTiO_3$ crystals are investigated in two-wave coupling experiments. The 45°-cut crystals did not perform as expected, and their performance points to a need to improve the mathematical model of two-wave coupling to include the effects of beam-fanning. The sensitivity of the confocal resonator to mechanical vibrations and air currents were learned along with methods to overcome these problems and align/stabilize the resonator. The $BaTiO_3$ crystals were placed within the resonator to perform qualitative analysis on the crystals. Within the resonator, it was verified that the 45° crystal does have more gain potential than the z-cut crystal. Experiments with the holographic plates at the 1-3° angles necessary for the confocal resonator show a diffraction efficiency of 12 %.

The result of these experiments is a qualified yes to the feasibility of the optical associative memory in the confocal resonator. The qualification comes from the need for a better model of two-wave coupling and beam-fanning and follow-on quantitative analysis of the 45°-cut crystal within the confocal resonator.